

UC Santa Cruz

UC Santa Cruz Electronic Theses and Dissertations

Title

Electrocatalysts for Water Splitting and Carbon Dioxide Reduction Reaction

Permalink

<https://escholarship.org/uc/item/6cp2t5nv>

Author

Wang, Shanwen

Publication Date

2022

Peer reviewed|Thesis/dissertation

UNIVERSITY OF CALIFORNIA
SANTA CRUZ

**ELECTROCATALYSTS FOR WATER SPLITTING AND CARBON
DIOXIDE REDUCTION REACTION**

A dissertation submitted in partial satisfaction
of the requirements for the degree of

DOCTOR OF PHILOSOPHY

in

CHEMISTRY

by

Shanwen Wang

June 2022

The Dissertation of Shanwen Wang is approved:

Professor Yat Li, chair

Professor Jin Zhong Zhang

Professor Scott R. J. Oliver

Peter Biehl
Vice Provost and Dean of Graduate Studies

Copyright © by
Shanwen Wang
2022

Table of Contents

List of Figures	v
List of Tables	xiv
Abstract	xv
Dedication	xviii
Acknowledgements	xix
Chapter 1 - Introduction of Electrochemical Water Splitting	1
Abstract	1
1.1 Background	1
1.2 Basic Mechanisms	2
1.2.1 Hydrogen Evolution Reaction	3
1.2.2 Oxygen Evolution Reaction	6
References	8
Chapter 2 - Periodic Porous 3D Electrodes Mitigate Gas Bubble Traffic during Alkaline Water Electrolysis at High Current Densities	10
Abstract	10
2.1 Introduction	10
2.2 Experimental Section	14
2.3 Results and Discussion	20
2.4 Conclusion	43
References	44
Chapter 3 - Introduction of Electrochemical CO ₂ Reduction	49
Abstract	49
3.1 Background	49

3.2 Basic Mechanisms	49
References.....	52
Chapter 4 - Cu ₂ O/CuS Nanocomposites Show Excellent Selectivity and Stability for Formate Generation via Electrochemical Reduction of Carbon Dioxide	54
Abstract	54
4.1 Introduction.....	54
4.2 Experimental Section	60
4.3 Results and Discussion	63
4.4 Conclusion	79
References.....	80
Chapter 5 - Amorphous CeO ₂ -Cu Heterojunction for CO ₂ Reduction into Multi-carbon Alcohols	87
Abstract.....	87
5.1 Introduction.....	87
5.2 Experimental Section	90
5.3 Results and Discussion	94
5.4 Conclusion	107
References.....	107
Chapter 6 - Outlook	111
References.....	114

List of Figures

Chapter 1

Figure 1.1 A typical Volcano shape plot. $\log i_0$ values of HER as a function of M-H bond energy.

Chapter 2

Figure 2.1 3D printing of 3DPNi and the deposition of C-Ni_{1-x}O. a) Schematic illustration of the ink formulation. b) G (elastic modulus) versus shear stress (top) and shear stress versus shear rate (bottom) for Ni-based inks with solid loadings of 40 vol% (blue) and 50 vol% (red). c–e) Schematic diagrams showing the preparation of 3DPNi and the surface functionalization of 3DPNi with C-Ni_{1-x}O catalyst. Inset in (d) is a digital photographic image of a 3DPNi lattice structure. Scale bar is 0.5 mm. SEM images collected from f) a C-Ni_{1-x}O/3DPNi lattice structure and g) high magnification view of the surface of an individual filament of the lattice structure. Scale bars are 500 and 4 μm , respectively.

Figure 2.2 EDS spectra of a) 3DPNi and b) NF.

Figure 2.3 a, b) SEM images of NiC₂O₄·2H₂O/3DPNi collected at low and high magnifications, respectively. c) XRD pattern of the NiC₂O₄·2H₂O/3DPNi.

Figure 2.4 XRD pattern of NiC₂O₄·2H₂O powders collected after annealing in Argon.

Figure 2.5 SEM images of the C-Ni_{1-x}O grown on a) 3DPNi and b) NF, respectively. Scale bars are 4 μm .

Figure 2.6 High-speed camera images of bubble release from C-Ni_{1-x}O/NF and C-Ni_{1-x}O/3DPNi. Side view high-speed camera images showing bubble release from a) C-Ni_{1-x}O/NF and b) C-Ni_{1-x}O/3DPNi structures at different periods of time. Scale bars are 2 mm. Red and blue dashed circles highlight the initial bubble in the first and second batch of bubble release, respectively.

Figure 2.7 High-speed camera images of bubble transport through C-Ni_{1-x}O/NF and C-Ni_{1-x}O/3DPNi. Top view high-speed camera images of a-c) C-Ni_{1-x}O/NF and g-i) C-Ni_{1-x}O/3DPNi collected at different periods of time. d,e,j,k) The corresponding images with dashed lines highlighting the shape of bubbles during transport in the two structures. f,l) The images with dashed lines highlighting the bubble shape exiting the two structures. Scale bars are 500 μ m.

Figure 2.8 Structure model of a) 3DPNi and b) NF. c) Relative bubble migration time through 3DPNi and NF as a function of bubble diameter, determined by time to cross the central plane of the structure (units are dimensionless). The two square data points represent the bubbles (diameter $d = 5$ and 7) entering the NF at different locations. d,e) Simulation frames showing bubble shape ($d = 20$) during transport in (d) 3DPNi and (e) NF. Arrow in the inset of (e) highlights an interaction with the NF surface, which is manifested through bubble deformation.

Figure 2.9 Gas bubble coalescence and release for C-Ni_{1-x}O/NF and C-Ni_{1-x}O/3DPNi electrodes during water electrolysis. High-speed camera images collected from the a) C-Ni_{1-x}O/NF and b) C-Ni_{1-x}O/3DPNi electrodes during water electrolysis. Scale bars are 2 mm.

Figure 2.10 Schematic illustrations of bubble coalescence and migration. a) C-Ni_{1-x}O/NF and b)

C-Ni_{1-x}O/3DPNi, respectively. Dashed box highlighting the coalescence of adjacent gas bubbles.

Figure 2.11 Electrochemical performance of C-Ni_{1-x}O/NF and C-Ni_{1-x}O/3DPNi during water electrolysis. Polarization curves of C-Ni_{1-x}O/NF and C-Ni_{1-x}O/3DPNi collected in 1.00 M KOH at a scan rate of 0.1 mV s⁻¹ for a) HER and d) OER. b,e) Plots to compare HER and OER overpotentials (η) of C-Ni_{1-x}O/3DPNi (0.1 mV s⁻¹) obtained at $j_{\text{geo}} = 50, 100, 500, \text{ and } 1000 \text{ mA cm}^{-2}$, with (b) HER catalysts, including Ni/NiO-NF (2 mV s⁻¹), NiOx@bamboo-like carbon nanotubes-NF (5 mV s⁻¹), NiCo₂S₄/NF (2 mV s⁻¹), MoO_x/Ni₃S₂-NF (0.1 mV s⁻¹), FeO_x/Fe foam (0.1 mV s⁻¹), and (e) OER catalysts, including NiO/carbon nitride (10 mV s⁻¹), FeO_x/Fe foam (0.1 mV s⁻¹), NiFeP (20 mV s⁻¹), MoO_x/Ni₃S₂-NF (0.1 mV s⁻¹), and Ni-Fe-OH@Ni₃S₂/NF (0.5 mV s⁻¹) in 1.00 M KOH electrolyte. c,f) Polarization curves shown in (a) and (d) with current normalized to the electrode's ECSA. The j_{ECSA} ratios (refers to the ratio of j_{ECSA} of C-Ni_{1-x}O/3DPNi to j_{ECSA} of C-Ni_{1-x}O/NF) are plotted as a function of overpotential for HER (inset of (c)) and OER (inset of (f)). g) Chronoamperometry curve collected from a water electrolysis device, using C-Ni_{1-x}O/3DPNi as OER and HER electrodes, at 2.2 V in 1.00 M KOH electrolyte at 80 °C.

Figure 2.12 EIS spectra of the C-Ni_{1-x}O/3DPNi and C-Ni_{1-x}O/NF. a) HER and b) OER, with dot representing experimental data and curve representing simulated results, insets are the tables showing the solution resistance (R_s) and charge transfer resistance (R_{ct}).

Figure 2.13 SEM images of the C-Ni_{1-x}O/3DPNi samples with printed pore sizes of a) 150 μm, and b) 750 μm. Scale bars are 500 μm.

Figure 2.14 Polarization curves of the C-Ni_{1-x}O/NF and C-Ni_{1-x}O/3DPNi with different pore size (150, 450 and 750 μm) collected in 1.00 M KOH for a) HER and b) OER at the scan rate of 0.1 mV s⁻¹. c) and d) are the polarization curves in a) and b) with current normalized to electrochemical surface area.

Figure 2.15 Chronoamperometry curve of the full water splitting with C-Ni_{1-x}O/3DPNi as HER and OER electrodes at the voltage of 2.56 V and room temperature.

Chapter 3

Figure 3.1 proposed reaction mechanism on different metal catalysts. Reproduced with permission from the study by Zhang et al.

Chapter 4

Figure 4.1 A schematic of the band alignment of Cu₂O /CuS heterojunctions based on previous reports, assuming a band gap within the reported range of 1.5-2.0 eV.

Figure 4.2 (a) A schematic illustration of the synthesis of Cu₂O/CuS nanocomposites. (b) and (c) SEM images of Cu₂O/CuS nanocomposites grown on a copper gauze collected at different magnifications. (d) HR-TEM image collected from a representative Cu₂O/CuS particle. (e) Corresponding FFT image of (d). Blue and yellow dashed lines highlight the diffraction rings of polycrystalline Cu₂O and CuS

particles, respectively. (f-i) HAADF-TEM image of Cu₂O/CuS nanocomposites and the corresponding mapping images of element O, Cu, and S.

Figure 4.3 (a) Cu 2p XPS spectrum. (b) Cu Auger LMM spectrum. (c) O 1s and (d) S 2p XPS spectra. All spectra were collected from Cu₂O/CuS particles without Cu gauze substrate. The black curves represent experimental data and red curves represent the fitting curve. The dashed lines represent deconvoluted peaks.

Figure 4.4 (a) Faradaic efficiency and (b) partial current for formate generation obtained from Cu₂O/CuS and Cu gauze at different applied potentials. The inset figure in (b) shows a magnified view of partial currents obtained at -0.4 V and -0.5 V vs. RHE.

Figure 4.5 (a) Faradaic efficiency and partial current density (towards formate) comparison of the Cu gauze, CuS, Cu₂O and Cu₂O/CuS (CuS and Cu₂O data was extracted from previous reports. (b) Faradic efficiency obtained from Cu₂O/CuS and Cu gauze at -0.9 V vs. RHE. The inset figures in (b) shows the contact angle of the 0.100 M KHCO₃ droplet on the Cu gauze (top left) and Cu₂O/CuS catalyst (bottom right). (c) A plot of FE for formate collected from the Cu₂O/CuS catalyst at -0.9 V vs. RHE for 30 hours.

Figure 4.6 Comparison of calculated CO₂RR pathways to produce formic acid from (a) OCHO* and (b) COOH* intermediates on CuS (110) without surface O_S or vacancy species. Analogous pathways with surface sulfur vacancies V_S species are shown in (c) and (d). Vacancies at S0 sites (V_{S0}) leave undercoordinated Cu that strengthen OCHO binding (c), while vacancies at S dimers (V_{S1}) leave undercoordinated S that more strongly bind COOH* (d). The black curves are pathways at 0 V vs. RHE and the red

curves are at the predicted limiting potential (the applied overpotential) that makes the entire pathway downhill in free energy, as computed within the CHE model.

Figure 4.7 Calculated binding free energies of CO* relative to gas-phase CO(g). The CO molecular reference adopts an electronic energy correction of +0.07 eV and a chemical potential contribution at 298 K and 5562 Pa. The plots show binding on (a) pure CuS (110), (b) surfaces with substitutional O_S on the non-S dimer sites (O_{S0}), (c) surfaces with O_S on S dimer sites (O_{S1}), (d) surfaces with vacancies at the S0 site, and (e) surfaces with vacancies at the S1 site. CO* adsorbs to Cu sites and exhibits weak and unfavorable binding free energies, where it is expected to dissociate.

Figure 4.8 Comparison of calculated CO₂RR pathways to produce formic acid from (a,c) OCHO* and (b,d) COOH* intermediates on CuS (110) with substitutional O at a surface dimer site (O_{S1}). The top and bottom panels differ in the proximity of the O_{S1} to the bound intermediate, e.g. acting as a participant in the binding or as a neighboring atom. The black curves are pathways calculated at 0 V vs RHE and the red curves are at the potential that makes the entire included pathway downhill in free energy, as computed within the CHE model. O_{S1} are found to slightly stabilize the OCHO*-mediated formic acid pathway (a,c), but make it much easier to bind COOH* intermediates at both the S1 (b) and O_{S1} sites (d) relative to pure CuS(110).

Figure 4.9 Comparison of calculated CO₂RR pathways to produce formic acid from (a) OCHO* and (b) COOH* intermediates on CuS (110) with substitutional O at a the S0 non-dimer surface S site (O_{S0}). The black curves are pathways calculated at 0 V vs RHE and the red curves are at the potential that makes the entire included pathway

downhill in free energy, as computed within the CHE model. O_{S0} are found to stabilize the $OCHO^*$ -mediated formic acid pathway (a), but make it much easier to bind $COOH^*$ intermediates at the $S0$ site.

Figure 4.10 Comparison of calculated hydrogen evolution reaction (HER) pathways to adsorb H and produce H_2 on (a) a Cu site, (b) a non-dimer S site ($S0$), and (c) a S dimer site ($S1$) on CuS (110) surfaces. The black curves are pathways calculated at 0 V vs RHE and the red curves are at the potential that makes the entire included pathway downhill in free energy, as computed within the CHE model. In (b) and (c) we also show competitive hydrogen sulfide evolution from surface S sites, showing that HER is preferred over surface degradation on CuS(110). H^* preferentially binds to anion sites, which may compete with $COOH^*$ intermediates but not $OCHO^*$, which most favorably binds through metal sites.

Figure 4.11 Comparison of calculated hydrogen evolution reaction (HER) pathways to adsorb H and produce H_2 on substitutional O_S occupying (a) a non-dimer $S0$ site and (b) a $S1$ dimer site on CuS (110) surfaces. We also show the competitive process for dissociation of the surface O_S as H_2O rather than facilitating HER, which we find is favorable for both the $S0$ and $S1$ sites at 0 V vs RHE. Thus, surface O_S sites are not expected to be long-lived under reducing conditions.

Figure 4.12 Comparison of calculated CO_2RR pathways to produce formic acid from (a) $OCHO^*$ and (b) $COOH^*$ intermediates on CuS (110) with a surface S vacancy (V_{S0}) at the $S0$ S site. The black curves are pathways calculated at 0 V vs RHE and the red curves are at the potential that makes the entire included pathway downhill in free

energy, as computed within the computational hydrogen electrode (CHE) model. V_{S0} are found to significantly enhance the OCHO*-mediated formic acid pathway, as the undercoordinated Cu can more strongly bind OCHO* relative to pure CuS(110).

Figure 4.13 Comparison of calculated CO₂RR pathways to produce formic acid from (a) OCHO* and (b) COOH* intermediates on CuS (110) with a surface S vacancy (V_{S1}) at a the S1 dimer S site. The black curves are pathways calculated at 0 V vs RHE and the red curves are at the potential that makes the entire included pathway downhill in free energy, as computed within the CHE model. V_{S1} are found to slightly destabilize the OCHO*-mediated formic acid pathway (a), but make it much easier to bind COOH* intermediates at the undercoordinated surface S1 sites relative to pure CuS(110).

Chapter 5

Figure 5.1 Schematic illustration of the synthesis and test of as-dealloyed catalysts.

Figure 5.2 X-ray diffraction patterns of a) Al₉₀Cu_{7.5}Ce_{2.5} alloy precursor and b) as-dealloyed sample.

Figure 5.3 a) and b) are the transmission electron images of the spent np CeO₂-Cu catalysts at low and higher magnifications, c) SAED image, d) HR-TEM image of the np CeO₂-Cu particles, e) Cu 2p and Ce 3d core-level XPS spectra of the spent np CeO₂-Cu catalyst.

Figure 5.4 a)-c) *CO adsorption configurations on np CeO₂-Cu catalyst. d)-f) *CH₂CHO adsorption configurations 6'-8' on np CeO₂-Cu catalyst. Green, red, blue

and brown spheres represent Ce, O, Cu, and C atoms, respectively. The top view and side view are highlighted by black and cyan boxes, respectively.

Figure 5.5 The protonation paths of *CH_2CHO and corresponding energy barriers over Cu-Ce and Cu-Ce site of np CeO₂-Cu.

Figure 5.6 F.E. comparisons of all products of a) np CeO₂-Cu and b) np Cu at different potentials. The dashed box highlights the F.E. of C₂₊ alcohols.

Figure 5.7 The comparisons of a) F.E. of alcohols, b) the ratio of F.E. of ethylene/alcohol, c) partial current density of alcohol, d) C_{dl} , of np CeO₂-Cu and np Cu, e) the ratio of j_{ecsa} of np CeO₂-Cu to np Cu at different potentials, f) literature data tested under similar conditions.

List of Tables

Chapter 2

Table 2.1 Input parameters used for the Shan-Chen LBM model

Chapter 3

Table 3.1 Major products of CO₂ reduction with different reaction pathways and standard reaction potentials.

Chapter 4

Table 4.1 Comparison of the catalytic performance of CuS/Cu₂O for formate formation with other state-of-the-art Cu-based catalysts.

Chapter 5

Table 5.1 *CO adsorption configurations and associated adsorption energy.

Table 5.2 *CH₂CHO adsorption configurations and associated adsorption energy.

Abstract

Electrocatalysts for Water Splitting and Carbon Dioxide Reduction Reaction

By

Shanwen Wang

With the growth of global population and the advancement of civilization, the energy demand is increasing rapidly. It's reported that the global annual energy demand is around 12 billion tons of oil equivalent and lead to 39.5 Giga tons of CO₂ gas. In 2013, carbon dioxide (CO₂) concentration in the atmosphere reached 400 parts per million for the first time in human history. The rise of CO₂ level is believed to be one of the major reasons for the anthropogenic climate change, and it's urgent to find a promising method to reduce the atmospheric CO₂ level.

Reducing CO₂ emission by using alternative clean fuels, *e.g.*, hydrogen fuel, is one of the promising methods. Electrolysis of water is one of most efficient and environmentally friendly methods to generate hydrogen gas and attracted a lot of attention recently. High-efficient, low-cost, and stable catalysts are required for both cathode and anode to reduce the activation energy barriers for hydrogen and oxygen evolution reactions. Significant advances have been made lately in developing water splitting catalysts, but there is still a lot of room for improvement.

Directly reduction of CO₂ into useful products is another promising method to reduce atmospheric CO₂ level. We can achieve a dual benefit by converting atmospheric CO₂ into value-added chemicals. Importantly, with the increasing prevalence of wind and solar power, the cost of electricity continues to decrease.

Abundant and low-cost renewable electrical energy sources make electrochemical reduction of CO₂ an attractive and promising solution for CO₂ mitigation. As a result, enormous effort has recently been devoted to exploring novel catalysts for electrochemical CO₂ reduction reactions (CO₂RR), with a goal of achieving improved selectivity, activity, and stability.

This dissertation covers my five years' study on designing and preparing catalysts for water splitting and electrochemical CO₂ reduction. For water splitting, we used a 3D printing technique to develop a new porous electrode with periodic pore structures. These pores aligned in the same direction and act as built-in gas bubble flow channels that effectively suppressed bubble coalescence, jamming, and trapping and, hence, result in rapid bubble release. The 3D printed electrodes decorated with catalysts achieved a high current density of 1000 mA cm⁻² at fairly low hydrogen evolution reaction and oxygen evolution reaction overpotentials. For electrochemical CO₂ reduction, we developed a new Cu₂O/CuS composite catalyst that simultaneously achieves an excellent faradaic efficiency of 67.6% and a large partial current density for generating formate. More importantly, it maintains the catalytic performance for at least 30 hours. The findings provided critical insights in the role of CuS in stabilizing the catalyst under CO₂ reduction conditions. My second CO₂ reduction project aims to enhance the selectivity and activity for carbon dioxide reduction towards C₂₊ alcohols (ethanol and propanol). We developed Cu-Ce catalysts for CO₂ reduction towards C₂₊ alcohols. Interfacing Cu and Ce and tuning the Cu/Ce ratio can modify the catalyst's electronic properties for improving CO adsorption. The Cu-Ce catalyst showed ~35%

Faradaic efficiency towards C_{2+} alcohols, which is almost twice as that of the Cu control sample.

Dedication

DEDICATED

TO

MY PARENTS, QUANSHENG WANG & YAN XIA

Acknowledgements

Five years passed so fast, I can't believe I almost finished my Ph.D. journey! I would like to express my deep sense of thanks to all those people who helped me during my Ph.D. studies.

Firstly, I would sincerely thank my advisor, Prof. Yat Li. Without his offer, I could not make it to be here. He is a very nice and understanding person, which makes me enjoy each project worked with him. His excellent scientific training reshaped my way to do research. His motivation-driven style towards every research topic, supportive attitude, timely and scholarly advice have helped me to a very great extent to accomplishing my research.

Secondly, I would like to thank my dissertation reading committee members, Professor Jin Zhong Zhang and Professor Scott R. J. Oliver. Their constructive suggestions, thoughtful feedback and encouraging words helped me a lot. I would also like to thank Professor David P. Belanger, who served as my committee member during my oral qualifying exam and gave me helpful suggestions in my research.

Thirdly, I need to thank Dr. Tianyi Kou. He is a talented and mature scientist. He provides me strong and continues support for my study and life. I would also like to thank my current and former lab mates: Professor Gongming Wang, Professor Xihong Lu, Dr. Hanyu Wang, Professor Teng Zhai, Dr. Tianyu Liu, Dr. Yi Yang, Dr. Bin Yao, Dr. Jing Zhang, Mingpeng Chen, Megan Freyman, Dun Lin, Anica Pinongcos, Riley Ball, Qiu Ren, Xinzhe Xue, Ella Davidi, Sam Eisenberg. I also thank these visiting scholars in our lab: Professor Changjin Tang, Dr. Huarong Peng, Dr.

Cheng Cheng, Dr. Xiaoli Fan. In addition, I would like to thank our collaborators: Dr. Eric Duoss, Dr. Fang Qian, Dr. Cheng Zhu, Dr. Joel Varley at Lawrence Livermore National Lab; Professor Jennifer Lu, Samuel Chiovoloni and Han-Lin Kuo at University of California, Merced.

Finally, I would like to thank my parents for their understanding and financial support. Due to the Covid-19 pandemic, I haven't been able to visit them for 3 years, I love my parents and I miss them so much!

The text of this dissertation includes reprints of the following previously published or subsequently published materials:

1. T. Kou, **S. Wang**, R. Shi, T. Zhang, S. Chiovoloni, J. Q. Lu, W. Chen, M. A. Worsley, B. C. Wood, S. E. Baker, E. B. Duoss, R. Wu, C. Zhu, Y. Li, *Adv. Energy Mater.* **2020**, *10*, 2002955.
2. **S. Wang**, T. Kou, J. B. Varley, S. A. Akhade, S. E. Weitzner, S. E. Baker, E. B. Duoss, Y. Li, *ACS Materials Lett.* **2021**, *3*, 100-109.
3. T.Kou, **S. Wang**, S. Yang, D. Rao, S. Chiovoloni, J. Lu, E. Duoss, Y. Li, in progress. (co-first author)

Chapter 1

Introduction of Electrochemical Water Splitting

Abstract

Over the past century, the global temperature increases steadily due to anthropogenic activities. In 2018, 315 cases of disasters are related to climate change, which include drought, extreme temperature, flooding, storms, wildfire and landslides, 131.7 billion dollars were lost. The rise of CO₂ level is believed to be one of the major reasons for the anthropogenic climate change, and it's urgent to find a promising method to reduce the atmospheric CO₂ level. Reducing CO₂ emission by using alternative clean fuels, e.g., hydrogen fuel, is one of the promising methods. Electrolysis of water is one of most efficient and environmentally friendly methods to generate hydrogen gas and attracted a lot of attention recently. High-efficiency, low-cost, and stable catalysts are required for both cathode and anode to reduce the activation energy barriers for hydrogen and oxygen evolution reactions. Significant advances have been made lately in developing water splitting catalysts, but there is still a lot of room for improvement. In this chapter, the water splitting mechanisms, evaluation methods and different kinds of catalysts will be discussed.

1.1 Background

With the growth of global population and the advancement of civilization, the energy demand is increasing rapidly. It's reported that, in 2010, 12717 million tons of oil equivalent (MTOE) was consumed worldwide, 80% of the energy was generated from fossil fuels.¹ Fossil fuels are not sustainable, and the combustion of fossil fuels

will lead to the rise of CO₂ level.² In 2013, carbon dioxide (CO₂) concentration in the atmosphere reached 400 parts per million for the first time in human history³. The rise of CO₂ level is believed to be one of the major reasons for the anthropogenic climate change. In 2018, it's reported that 315 cases of disasters are related to climate change, including drought, flooding, landslides, storms, etc. 68.5 million people were affected and 131.7 billion dollars were lost.⁴ A clean and renewable energy carrier is desperately in need.

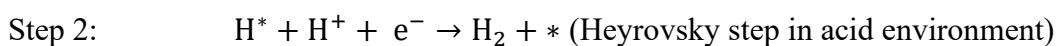
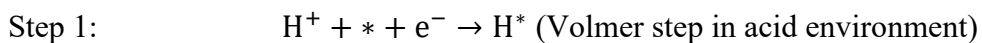
Hydrogen gas, with high combustion energy and zero carbon emission features, has attracted a lot of attention recently. Nowadays, the most common methods to produce hydrogen gas are steam reforming (from natural gas) and electrolysis from water (water splitting). Compare with steam reforming method, electrolysis method is more environmentally friendly. The electricity required for water splitting can be derived from renewable energy, such as wind energy and solar energy, the total process could achieve carbon emission free. Thus, electrochemical water splitting is considered as a promising method to generate hydrogen gas and is gaining increased attentions recently.

1.2 Basic Mechanisms

Electrochemical water splitting can be divided into two half reactions, one is hydrogen evolution reaction (HER), another is oxygen evolution reaction (OER). Developing catalysts with high activity and long stability are critical for both half reactions to reduce the total energy input.

1.2.1 Hydrogen Evolution Reaction

Hydrogen evolution reaction (HER) is a classic two electron transfer reaction. The chemical reaction equations in different medias can be different. The cathodic HER reaction can be described as :



where * is the active center of the catalysts. As described above, the first step is called Volmer step, where the H^+ (or H_2O) adsorb on the catalyst surface to form adsorbed H^* . Then followed by Heyrovsky step (one adsorbed H^* combine with one proton) or Tafel step (two adsorbed H^* combine with each other) to form H_2 . All the three steps are crucial for HER. To figure out the rate determining step and get more insights of the reaction mechanism, Tafel slope is widely used in HER study. In the next part, Tafel slope in HER study will be summarized and discussed.

In 1905, Tafel equation was summarized by a Swiss chemist, Julius Tafel, from the study of the electroreduction of organics on metal electrodes (eq.1.1)⁵:

$$\eta = a + b \log i \quad (\eta = U - U_0) \quad (1.1)$$

where η represents the overpotential, U is the applied potential, U_0 is the thermodynamically determined potential, i is current density, b is known as Tafel

slope, α is the charge transfer coefficient, R is the gas constant, T is temperature, F is Faradic constant.

In 1930s, Bultter, Volmer and co-workers established the relation between the Arrhenius equation and Tafel equation (eq.1.2)⁶:

$$i = i_{\text{forward}} - i_{\text{backward}} = i_0 \exp\left(\frac{\alpha\eta F}{RT}\right) - i_0 \exp\left(\frac{-(1-\alpha)\eta F}{RT}\right) \quad (1.2)$$

where i_{forward} is the forward current density, i_{backward} is the backward current density, i_0 is the exchange current density. When the η is relatively large, the equation can be simplified as (eq.1.3):

$$\eta = -\left(\frac{2.303RT}{\alpha F}\right) \log i_0 + \left(\frac{2.303RT}{\alpha F}\right) \log i \quad (1.3)$$

Compare eq.1.3 with eq.1.1, a (eq.1.4) and b (eq.1.5) are derived as:

$$a = -\left(\frac{2.303RT}{\alpha F}\right) \log i_0 \quad (1.4)$$

$$b = \left(\frac{2.303RT}{\alpha F}\right) \quad (1.5)$$

As shown above, a and b are related to α . It's worth to note here that the number of electrons before the rate determining step also need to be considered. Thus, if the rate determining step is a one electron transfer step, the value of charge transfer coefficient is 0.5, and the overall α should be $n+0.5$, so the Tafel slop will be $2.303RT/(n+0.5)F$, n is the number of electrons that transferred before the rate determining step. At 298 K, if $n=0$, the value of Tafel slope is around 120 mV dec^{-1} , if $n=1$, the value will be around 40 mV dec^{-1} . While if the rate determining step is a zero electron transfer step, the value of α is 0, and the Tafel slop equation will be $2.303RT/nF$, so if $n=1$, the value of Tafel slope is around 60 mV dec^{-1} , if $n=2$, the value will be around 30 mV dec^{-1} .⁶ It's widely

accepted that the Tafel slope of 120, 40, 30 mV dec⁻¹ indicates the rate determining step is Volmer, Heyrovsky and Tafel step, respectively.⁷ Generally, a lower Tafel slope value is desired for HER as a lower Tafel slope value suggests the rate determining step is near the end of the HER process. Although Tafel plot simply describes the increase of overpotential vs. the increase of current density, it is very useful for kinetic study.

From the HER reaction steps, it's not difficult to get the conclusion that the binding energy between the catalyst and the reactants should be neither too large nor too small, and this is the basic idea of Sabatier principle. Sabatier principle states that there will be an optimal binding energy between the catalyst and the reactant. Therefore, if we plot the activity (*e.g.*, current density) vs. the binding energy (*e.g.*, hydrogen adsorption energy), a volcano shape curve will be obtained (Figure 1.1).⁸ It's clearly shown in the figure that some noble metals such as Pt, Re, Ir and Rh have the highest activity for hydrogen evolution reaction. However, due to the high cost of noble metals, the large-scale application of noble metals on HER is limited. Instead, some non-noble metal-based catalysts, such as metal (Ni, Co, Fe, etc.) sulfides, hydroxides, nitrides, phosphides, and oxides attract a lot of attention recently. For example, the overpotential of carbon doped NiO is 27 mV at 10 mA cm⁻²,⁹ which is even comparable with some noble-metal based catalysts, such as Pt/C (20 mV), Ru nanoparticles on C₂N layer (17 mV),¹⁰ at same test conditions. However, for large scale applications, low overpotential at high current density (~1000 mA cm⁻¹) is crucial¹¹ and there is still much room for improvement.

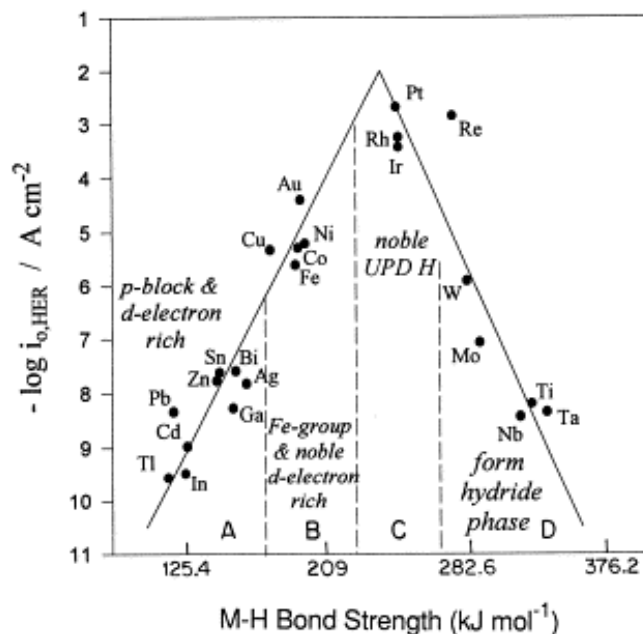
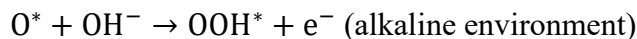
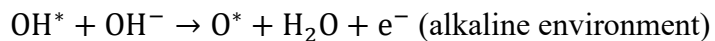
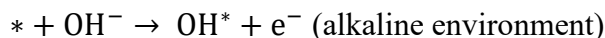


Figure 1.1 A typical Volcano shape plot. $\log i_0$ values of HER as a function of M-H bond energy.¹²

1.2.2 Oxygen Evolution Reaction

Compare with the HER, oxygen evolution reaction (OER) is four electrons involved reaction, in which the multistep elementary reactions create significant energy barriers. And the reaction mechanism is more complicated. The anodic OER reaction can be described as¹³:



Fourth step: $\text{OOH}^* \rightarrow * + \text{O}_2 + \text{H}^+ + \text{e}^-$ (acid environment)

$\text{OOH}^* + \text{OH}^- \rightarrow * + \text{O}_2 + \text{H}_2\text{O} + \text{e}^-$ (alkaline environment)

where * represents the active site of the catalysts. Similar to HER, Tafel slope is widely used in OER study. The difference is that the charge transfer coefficient α is determined by another equation (eq.1.6)¹⁴:

$$\alpha = \frac{n_b}{v} + n_r \beta \quad (1.6)$$

where n_b is the electron numbers that transferred back to the electrode before the rate determining step, v is the number of rate determining steps, n_r is the electron numbers that involved in the rate determining step, and β is the symmetry factor (for single electron transfer reaction, $\beta = 0.5$). Thus, if the rate determining step is the first step, $n_b = 0$, $v = 0$, $n_r=1$ and $\beta = 0.5$, so the calculated Tafel slope=120 mV dec⁻¹. If the rate determining step is the reaction that after one electron transfer reaction, $n_b = 1$, $v = 1$ and $n_r=0$, the calculated Tafel slope=60 mV dec⁻¹. If the rate determining step is the second electron transfer step, $n_b = 1$, $v = 1$, $n_r=1$ and $\beta = 0.5$, the calculated Tafel slope=40 mV dec⁻¹. If the rate determining step is the third electron transfer step, then $n_b = 2$, $v = 1$ and $n_r=0$, the corresponding Tafel slope=30 mV dec⁻¹. Based on the discussion above, the value of Tafel slope could indicate the rate determining step, and very useful for OER mechanism study. Like HER, a lower Tafel slope value is preferred for OER study, as a smaller Tafel slope value indicates the rate determining step is near the end part of the four electrons involved OER process.

As shown before, there are three OER intermediates: O^* , HO^* , and HOO^* . Based on previous studies,¹⁵ there is scaling relationship between them, which means

the binding energies of these intermediates are dependent with each other, and the OER activity can be plotted versus only one parameter (e.g., binding energy of O^{*}). Therefore, a volcano shape plot can be created with overpotential vs. O^{*} binding energy. It's clearly shown in the figure that some noble based catalysts such as IrO_x and RuO₂ have impressive activity for OER and are considered as benchmark OER catalysts. However, the stability of these noble metal oxides is not good. During the OER test, these noble metal oxides tend to be oxidized and dissolved in the solution. In addition, due to the high cost of noble metals, the large-scale application of noble metals on OER is limited. Instead, some non-noble catalysts, such as NiO_x, Ni(OH)₂, NiFeOOH, etc., showed promising activity for OER and attracted a lot of attention recently.

References

1. C. Acar, I. Dincer, *Int. J. Hydrog. Energy* **2014**, *39*, 1-12.
2. N. Abas, A. Kalair, N. Khan, *Futures* **2015**, *69*, 31-49.
3. K. Willett, M., A. J. Dolman, D. F. Hurst, J. Rennie, and P. W. Thorne, Eds., in *Bulletin of the American Meteorological Society*, Vol. 95, American Meteorological Society, **2014**, 5.
4. S. Fawzy, A. I. Osman, J. Doran, D. W. Rooney, *Environ. Chem. Lett.* **2020**, *18*, 2069-2094.
5. G. T. Burstein, *Corros. Sci.* **2005**, *47*, 2858-2870.
6. Y.-H. Fang, Z.-P. Liu, *ACS Catal.* **2014**, *4*, 4364-4376.

7. T. Shinagawa, A. T. Garcia-Esparza, K. Takanabe, *Sci. Rep.* **2015**, *5*, 13801.
8. A. B. Laursen, A. S. Varela, F. Dionigi, H. Fanchiu, C. Miller, O. L. Trinhammer, J. Rossmeisl, S. Dahl, *J. Chem. Educ.* **2012**, *89*, 1595-1599.
9. T. Kou, M. Chen, F. Wu, T. J. Smart, S. Wang, Y. Wu, Y. Zhang, S. Li, S. Lall, Z. Zhang, Y.-S. Liu, J. Guo, G. Wang, Y. Ping, Y. Li, *Nat. Commun.* **2020**, *11*, 590.
10. J. Mahmood, F. Li, S.-M. Jung, M. S. Okyay, I. Ahmad, S.-J. Kim, N. Park, H. Y. Jeong, J.-B. Baek, *Nat. Nanotechnol.* **2017**, *12*, 441-446.
11. Y. Luo, L. Tang, U. Khan, Q. Yu, H.-M. Cheng, X. Zou, B. Liu, *Nat. Commun.* **2019**, *10*, 269.
12. A. G. Olabi, M. A. Abdelkareem, *Renew. Sust. Energ. Rev.* **2022**, *158*, 112111.
13. Z. Yan, H. Liu, Z. Hao, M. Yu, X. Chen, J. Chen, *Chem. Sci.* **2020**, *11*, 10614-10625.
14. N.-T. Suen, S.-F. Hung, Q. Quan, N. Zhang, Y.-J. Xu, H. M. Chen, *Chem. Soc. Rev.* **2017**, *46*, 337-365.
15. J. Rossmeisl, A. Logadottir, J. K. Nørskov, *Chemical Physics* **2005**, *319*, 178;
J. Rossmeisl, Z. W. Qu, H. Zhu, G. J. Kroes, J. K. Nørskov, *J. Electroanal. Chem.* **2007**, *607*, 83-89.

Chapter 2

Periodic Porous 3D Electrodes Mitigate Gas Bubble Traffic during Alkaline Water Electrolysis at High Current Densities

Abstract

Alkaline water electrolysis at high current densities is plagued by gas bubble generation and trapping in stochastic porous electrodes (e.g., Ni foams), which causes a significant reduction in the number of electrolyte accessible catalyst active sites. Here, 3D printed Ni (3DPNi) electrodes with highly controlled, periodic structures are reported that suppress gas bubble coalescence, jamming, and trapping and, hence, result in rapid bubble release. The 3DPNi electrodes decorated with carbon-doped NiO achieve a high current density of 1000 mA cm^{-2} in 1.00 M KOH electrolyte at hydrogen evolution reaction and oxygen evolution reaction overpotentials of 245 and 425 mV, respectively. This work demonstrates a new approach to the deterministic design of 3D electrodes to facilitate rapid bubble transport and release to enhance the total electrode catalytic activity at commercially relevant current densities.

2.1 Introduction

Much attention has recently focused on water electrolysis as a path to establish a hydrogen economy by converting intermittent renewable energies into clean hydrogen-based chemical energy. Presently, water electrolysis is performed in alkaline or acidic media. Alkaline water splitting (AWS) electrolyzers offer several advantages over proton exchange membrane (PEM) water electrolyzers performed in acidic media, such as lower cost cell components, which has led to their commercialization at the

megawatt level.¹ In addition, performing electrolysis under alkaline conditions can improve the purity of the generated hydrogen gas,² and, importantly, the less corrosive environment allows the use of most nonplatinum group metal catalysts for the hydrogen evolution reaction (HER) and the oxygen evolution reaction (OER).³ However, commercial AWS electrolyzers operate at relatively low current densities ($<400 \text{ mA cm}^{-2}$) and voltage efficiencies ($<80\%$),⁴ compared to PEM electrolyzers. Therefore, increasing the operational current density and voltage efficiency of AWS electrolyzers will enable more competitive industrial production of hydrogen gas with these systems.

The overall efficiency of AWS electrolyzers is determined by intrinsic and extrinsic factors.⁵ Tremendous efforts have been made to improve the intrinsic activity of electrocatalysts to minimize the cumulative energy barriers of proton-coupled electron transfer steps and accelerate the sluggish reaction kinetics of water-alkali HER and OER to reduce their overpotentials.⁶ We recently demonstrated that carbon doping is an effective method to introduce thermal neutral hydrogen adsorption sites in NiO and provide hot spots for water dissociation.⁷ The carbon-doped NiO catalyst achieved a HER current density of 10 mA cm^{-2} at an ultralow overpotential of 27 mV. Doping has also been used to improve the performance of OER catalysts. It has been reported that doping oxophilic Ce into NiO can increase the adsorption capability of NiO toward the oxygen intermediate species and, thus, increase its OER activity (10 mA cm^{-2} at 279 mV).⁸

In addition to enhancing the intrinsic activity of electrocatalysts, it is equally important to increase the electrodes' extrinsic activity, meaning electrolyzers should

ideally be operated at high current densities to generate hydrogen gas at commercially competitive rates. Yet, increasing the operational current density will result in significant gas bubble generation,⁹ which is a problem that may not be observed for operation at low current densities. Gas bubbles are problematic because they block a large portion of the catalytically active surface area, and therefore limit the hydrogen production rate. The presence of gas bubbles also generates significant Ohmic resistance that restricts the voltage efficiency at large current densities. To increase the operational current density, widely available 3D porous electrodes have been employed to enhance the catalytically active surface area and mass diffusion of electrolyte. Commercial nickel foam (NF) is one of the most commonly used 3D porous electrodes for AWS.¹⁰ The high electrical conductivity of nickel also makes NF an ideal substrate to support HER/OER catalysts. While the porous structure of NF can facilitate the mass transfer of electrolyte, the disordered pore/NF skeleton arrangement is not favorable for fast release of gas bubbles generated during water electrolysis.¹¹ Once gas bubbles form and detach from the electrode surface, they migrate upward due to buoyancy. As they transport through the disordered 3D structure, the bubbles can easily become blocked and trapped. As a result, these trapped bubbles create a physical barrier between active sites and electrolyte that causes significant Ohmic loss and decreases the number of available active catalytic sites,^{9, 11} especially at high current densities. It is highly desirable to have a 3D Ni architecture with ordered channels that allows rapid release of gas bubbles, yet it is challenging to construct such a complex electrode using conventional manufacturing methods.

Recently, 3D printing has been employed as a rapid approach to construct complex architectures with unique chemical, mechanical, and structural properties,¹² including structures favorable for mass transport¹³ and for heterogeneous catalysis such as water electrolysis.¹⁴ Extrusion-based 3D printing techniques, such as direct ink writing (DIW), have been utilized to create highly ordered multiscale cellular materials made from ceramics,¹⁵ polymers,¹⁶ metals,¹⁷ and carbons.¹⁸ Herein, we use this filament-based printing technique to fabricate a 3D printed Ni (3DPNi) lattice with periodic bubble flow channels. The 3DPNi surface was functionalized with carbon-doped nickel oxide (C-Ni_{1-x}O) nanorods as a HER/OER bifunctional catalyst. Visualization experiments were performed to observe gas bubble transport behavior and show that the 3D printed structure is effective in suppressing the drainage process and bubble coalescence, compared to the disordered structure of NF. C-Ni_{1-x}O-decorated 3DPNi (denoted as C-Ni_{1-x}O/3DPNi) electrodes achieve a high current density of 1000 mA cm⁻² at low overpotentials of 245 mV for HER and 425 mV for OER, respectively. Substantially lower current densities were obtained from NF decorated with the same catalyst (denoted as C-Ni_{1-x}O/NF) at the same overpotentials. C-Ni_{1-x}O/3DPNi also has a higher electrochemical surface area (ECSA) current (j_{ECSA}) than C-Ni_{1-x}O/NF at the same potential, suggesting that the rapid release of bubbles is critical to retaining the high specific reaction rate of the electrode especially at high potentials. Taken together, the results unambiguously show that the 3D printed lattice structures with ordered channels facilitate gas bubble transport and release, leading to enhanced performance for water electrolysis.

Gas evolution occurs on both electrodes during water electrolysis and it includes several steps. First, gas bubbles nucleate on the catalyst surface and grow due to the inward flux of adjacent dissolved gas and large Laplace pressure.¹⁹ When the dimension of the gas bubble achieves a critical value, the adhesion between the gas bubble and the catalyst surface will be overcome by buoyancy, and the bubble will detach.²⁰ How bubbles transport out of a porous electrode is determined by a number of factors such as electrode thickness, porosity, size, tortuosity, and spatial distribution of pores. For water electrolysis, avoiding bubble trapping is critical for the electrode's catalytic performance at high current densities. Esposito and co-workers utilized the buoyancy effect to drive the separation of hydrogen and oxygen gas bubbles in their 3D printed water electrolyzer.¹⁴ Herein, we hypothesized that the upward movement of gas bubbles driven by buoyancy can also be facilitated when channels with orientation align with the direction of buoyancy are built to guide bubble flow. The rapid release of gas bubbles via the bubble flow channels guarantees a large reactant accessible surface area even at high reaction rates (current density or potential). Moreover, uniform bubble flow also accelerates the mass transfer of the surrounding electrolyte to the catalyst surface through convection.

2.2 Experimental Section

Ni Ink Preparation: Nickel powder (mean particle size 3–7 μm , Alfa Aesar), PLGA copolymer (85:15 lactide:glycolide by molar ratio, Sigma-Aldrich), DCM (b.p. 40 $^{\circ}\text{C}$, Sigma-Aldrich), and EGBE (boiling point 171 $^{\circ}\text{C}$, Sigma-Aldrich) were used as received. Typically, 2 g PLGA pellets were fully dissolved into 2 g DCM to generate a

polymeric solution. Then, 26.7 g Ni powders were mixed with this solution to form a colloidal suspension for 30 s at 2000 rpm using a planetary mixer (ARE-250, Thinky). High-speed mixing concentrated the suspension due to the evaporation of DCM. Finally, 1 g EGBE and an appropriate amount of DCM were added to yield a composite ink composed of a total solid loading of 40 and 50 vol% (Ni + PLGA) and balanced DCM:EGBE ratio of 2:1.

Ink Rheology: The rheological properties of the Ni ink were characterized using a stress-controlled Rheometer (AR 2000ex, TA) with a 40 mm flat plate geometry and a gap of 500 μm in the presence of solvent trap to avoid solvent evaporation. A stress sweep from 10^{-2} to 10^3 Pa at a constant frequency of 1 Hz was conducted to record the shear modulus variations as a function of sweep stress. The yield stress (τ_y) was defined as the stress where storage modulus fell to 90% of the plateau value. A strain sweep from 10^{-1} to 10^2 s^{-1} was performed to record the apparent viscosities at varying shear rates.

Printing of Ni Lattices: The as-prepared Ni inks were loaded into a 10 mL syringe barrel (Nordson EFD) attached by a Luer-Lok to a smooth-flow tapered nozzle [inner diameter (d), 200 μm]. An air-powered fluid dispenser (Ultimus V, Nordson EFD) provided the appropriate pressure to extrude the ink through the nozzle. The target patterns were printed using a three-axis positioning stage (ABL9000, Aerotech). The 3D Ni green parts were printed onto a silicon wafer with an initial nozzle height of 0.7d to ensure adhesion to the substrate. The required pressure depended on the ink rheology, nozzle size, and printing speed, and typical values ranged from 60 to 90 psi

at 5–15 mm s⁻¹. The printed parts were dried in the air and then thermally treated at 300 °C for 1 h and 600 °C for 1 h in H₂. Finally, the samples were heat treated at 900 °C for 3 h in Ar. The typical printed sample xyz dimensions were 10 mm × 10 mm × 3 mm, and the linear shrinkage was below 10%.

Synthesis of C–Ni_{1-x}O Nanorods on 3D Printed Ni and NF: Nickel oxalate was grown on 3D printed Ni lattices by a hydrothermal method reported earlier.²³ Specifically, a two-electrode system was used in this step with the 3D printed Ni lattice as the working electrode and Ni foil as counter electrode. 0.3 M oxalic acid was used as the electrolyte. A voltage of 50 V was applied for 10 min to grow nickel oxalate on the surface of Ni lattice. Subsequently, nickel oxalate/3D printed Ni was heat treated in Ar atmosphere at 400 °C for 40 min to convert nickel oxalate to C–Ni_{1-x}O. The same synthetic method was used to grow C–Ni_{1-x}O on NF.

Structural Characterization: The morphologies of C–Ni_{1-x}O/3DPNi and C–Ni_{1-x}O/NF were characterized by scanning electron microscopy (SEM, Hitachi S-4800 II). The phase composition of the materials was investigated by X-ray diffraction (Rigaku SmartLab).

Gas Injection and High-Speed Camera Experiments: C–Ni_{1-x}O/3DPNi and C–Ni_{1-x}O/NF electrodes were horizontally mounted on a sample holder shelf and immersed in deionized water. A small syringe needle was inserted from the bottom into the samples at a 1 mm depth. The needle was connected to a syringe pump with plastic tubing. Air was pumped into the sample at a flow rate of 1 mL s⁻¹ to generate bubbles. To record gas bubble transport and release, two high-speed cameras (Photron Fastcam

mini-UX50) were mounted at the top and side of the sample to capture videos and images during water electrolysis measurements conducted at 4.8 V.

Shan-and-Chen-Type Multicomponent Multiphase Lattice Boltzmann Method: A multicomponent, multiphase lattice Boltzmann method,³⁴ as proposed by Shan and Chen, was employed to investigate bubble migration as a function of bubble size and porous structure (both random and periodic). This method overcomes numerical challenges with the Navier–Stokes equation and is appropriate for flow through complex geometries. The open source code Palabos³⁵ was used to carry out the simulations. A single-component density distribution function $f^\sigma(\mathbf{x},t)$ was introduced for each of the two fluid components, $f^\sigma(\mathbf{x},t)$ with $\sigma = 1$ for the gas bubble (fluid 1) and $\sigma = 2$ for the liquid electrolyte (fluid 2). Here \mathbf{x} denotes the spatial coordinate in 3D. The forces acting on each component, \mathbf{F}_σ , include fluid–fluid interfacial interactions, $\mathbf{F}_{c,\sigma}$, the fluid-solid adhesion, $\mathbf{F}_{ads,\sigma}$, and the gravitational force, \mathbf{F}_g . The key model parameters that describe both $\mathbf{F}_{c,\sigma}$ and $\mathbf{F}_{ads,\sigma}$ are G_c and $G_{ads,\sigma}$. The former is a parameter that controls the strength of the cohesion force, and the latter adjusts the interaction strength between each fluid and a solid porous structure.

The static contact angle between a bubble (of fluid 1) and a solid surface is then defined as³⁶

$$\cos\theta_1 = \frac{G_{ads,2} - G_{ads,1}}{G_c \frac{\rho_1 - \rho_{d,2}}{2}} \quad (2.1)$$

where $\rho_{d,2}$ is the dissolved density of fluid 2 in fluid 1. Note that $G_{ads,2} = -G_{ads,1}$ in the simulations. The selection of model parameters (Table 2.1) led to a contact angle

θ_1 of 156.4° and 154.0° computed from the static contact angle equation and simulation,³⁶ respectively.

Table 2.1 Input parameters used for the Shan-Chen LBM model

Variable	Descriptions	Values
ρ_1 and ρ_2	Equilibrium Fluid densities	2.00
τ	Relaxation-time	1.00
$\rho_{d,1}$ and $\rho_{d,2}$	Dissolved density	0.06
G_c	Cohesion force strength	0.90
F_g	Applied gravitational force	$1e^{-4}$
ϵ	Convergence threshold	$5e^{-6}$
$G_{ads,1}$	Adhesion parameters	0.4
$G_{ads,2}$	Adhesion parameters	-0.4

Using the model, a series of 3D simulations was carried out where a pure gas bubble of fluid 1 (ρ_1) was placed inside a $140 \times 120 \times 120$ cuboidal volume of fluid 2 (ρ_2) with periodic boundaries. A porous medium of size $120 \times 120 \times 120$ was also immersed in fluid 2, with a reference frame displaced by 20 units along the + x-direction. Migration of gas bubbles of different sizes was considered through both the random NF and periodic 3DPNi pore structures. For the former, the size and spatial distributions of the pores were relatively random, while the latter had a monodispersed pore size and well-defined spatial distribution. The pore structure for the periodic structures was chosen to match the 3D printed lattice model. The random structure was generated from an open-cell foam model reconstructed from a series of Micro computed tomography images. The model formulation is described in detail

elsewhere.^{36,37} The input parameters used for the Shan–Chen model are documented in Table 2.1. The parameters were selected according to recommendations published elsewhere.³⁶

Electrochemical Measurements: Electrochemical measurements were performed using a three-electrode system in 1.00 M KOH electrolyte. C–Ni_{1-x}O/3DPNi or C–Ni_{1-x}O/NF was used as working electrodes, Hg/HgO served as the reference electrode, and nickel foam was the counter electrode. The reference electrode was corrected using a calibration method reported elsewhere.³⁸ For HER, the electrolyte was purged by nitrogen gas prior to and throughout the measurements. Cyclic voltammetry (CV) was first performed in a potential window of –0.6 to –1.35 V versus Hg/HgO for 50 cycles at a scan rate of 20 mV s⁻¹. For OER, the electrolyte was saturated with oxygen prior to and during the measurement. CV was also performed in potential window of 0–0.8 V versus Hg/HgO for 20 cycles at the scan rate of 20 mV s⁻¹. Linear scan voltammograms (LSVs) were then collected at 0.1 mV s⁻¹. Electrochemical impedance spectroscopy (EIS) was performed at –1.08 V versus Hg/HgO for HER and 0.7 V versus Hg/HgO for OER, with frequency ranging from 100 kHz to 1 Hz and an amplitude of 5 mV. All LSV data were iR corrected based on EIS data (Figure 2.12). Finally, the stability test was performed at room temperature and 80 °C in a two-electrode configuration using C–Ni_{1-x}O/3DPNi as both OER and HER electrodes at the voltage of 2.56 and 2.2 V, respectively.

2.3 Results and Discussion

We use the DIW technique to prepare the Ni lattice structure. First, we prepared a paste-like ink (Figure 2.1a) composed of Ni particles, a lactide–glycolide copolymer (polylactic-co-glycolic acid (PLGA)), and a graded volatility solvent including dichloromethane (DCM) and ethylene glycol butyl ether (EGBE). The solid component of the ink is comprised of Ni powder and PLGA in a 3:2 volume ratio. PLGA was first dissolved in DCM to form a homogeneous, and low viscosity solvent-binder system. Next, Ni powder was added and, following DCM evaporation, a concentrated paste was obtained. Finally, small additions of EGBE and DCM were added, followed by mixing, to lower the ink viscosity to an appropriate level for printing. The high solid loading of the inks creates a viscoelastic response that enables shape retention and patterning of porous structures that possess features that span gaps in underlying layers. The graded volatility solvent system enables uniform printing at moderate pressures. The viscoelastic properties of the inks are represented by the shear elastic moduli of the Ni inks with varying solid loadings (40 and 50 vol%) and are measured by an oscillation technique (Figure 2.1b). We find that the Ni ink with 40 vol% solid loading exhibits an elastic modulus (G') plateau value of ≈ 4000 Pa and a yield stress (τ_y) of ≈ 30 Pa. By increasing the solid loading to 50 vol%, the G' plateau value increases to over 10000 Pa, while τ_y increased to ≈ 200 Pa. The ink flow behavior was quantified by measuring the apparent viscosities. As the shear rates increase, the apparent viscosity of the ink sharply decreases, which means that the ink exhibits a shear-thinning, non-Newtonian flow behavior. The 50 vol% ink shows more than one order of magnitude

higher apparent viscosity than the 40 vol% ink, showing that viscosity is highly dependent upon solid loading.

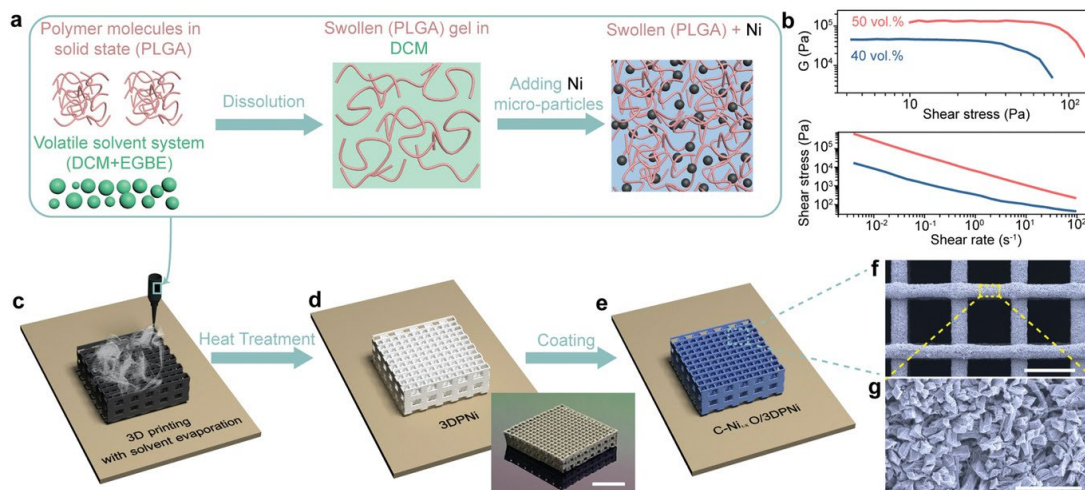


Figure 2.1 3D printing of 3DPNi and the deposition of C–Ni_{1-x}O. a) Schematic illustration of the ink formulation. b) G (elastic modulus) versus shear stress (top) and shear stress versus shear rate (bottom) for Ni-based inks with solid loadings of 40 vol% (blue) and 50 vol% (red). c–e) Schematic diagrams showing the preparation of 3DPNi and the surface functionalization of 3DPNi with C–Ni_{1-x}O catalyst. Inset in (d) is a digital photographic image of a 3DPNi lattice structure. Scale bar is 0.5 mm. SEM images collected from f) a C–Ni_{1-x}O/3DPNi lattice structure and g) high magnification view of the surface of an individual filament of the lattice structure. Scale bars are 500 and 4 μm , respectively.

3DPNi samples were prepared by a series of steps including printing (Figure 2.1c), heat treatment (Figure 2.1d), and catalyst coating (Figure 2.1e). To create 3D architectures, we loaded the ink into a syringe barrel, removed any trapped gas from

the ink mixture, affixed a micronozzle, and pressurized the printhead to deposit ink onto a planar substrate under computer numerical control with an xyz-coordinate and gantry-based motion system. The as-printed lattice structures consist of a linear array of rods (or filaments) within each layer with a center-to-center spacing (L) of $800\ \mu\text{m}$ (pore size is $450\ \mu\text{m}$). The overall structure is composed of five stacked layers with each layer aligned with the x- or y-axis such that an individual layer's orientation is orthogonal to its underlying layer. The as-printed structure exhibits minimal shape deformation and displays well-defined and interconnected vertical and horizontal pores. The printed green body consists of discrete Ni particles bound by polymer. Each green body structure was first thermally treated at 300 and $600\ ^\circ\text{C}$ (1 h) in hydrogen atmosphere to remove the polymer and partially sinter the Ni particles. Next, the structure underwent high temperature heat treatment at $900\ ^\circ\text{C}$ in argon atmosphere for 3 h to achieve even greater densification of the Ni material within each filament (Figure 2.1d inset). As shown in the X-ray energy dispersive spectra (Figure 2.2), 3DPNi and NF have similar elemental compositions (Ni, O, and C). We believe that it is unlikely to have carbon residuals derived from the organic binders after the high temperature treatment process.²² The C signal for the two samples is likely due to physically adsorbed carbon that stems from carbon-based contamination from sample processing.

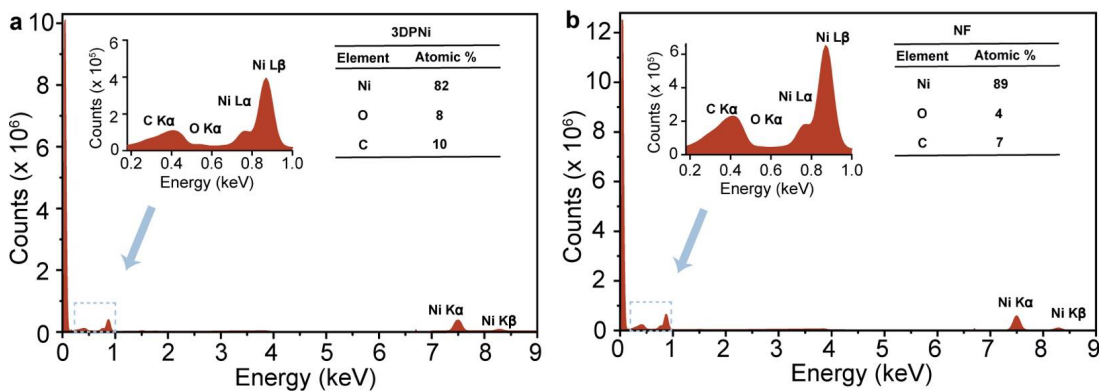


Figure 2.2 EDS spectra of a) 3DPNi and b) NF.

Nickel oxalate dihydrate bulk crystals were then grown uniformly on 3DPNi (Figure 2.3) using a previously reported anodization method.²³ Subsequent thermal treatment in argon atmosphere converted nickel oxalate dihydrate crystals into C–Ni_{1-x}O nanorods (Figure 2.1f,g and Figure 2.4) based on our method reported previously,⁷ while retaining the lattice structure of 3DPNi with interconnected bubble flow channels. The addition of C–Ni_{1-x}O nanorods roughened the electrode surface (Figure 2.1g) and decreases the contact area between gas bubbles and the catalyst and, therefore facilitates the rapid detachment of gas bubbles.²⁴ For comparison, C–Ni_{1-x}O nanorods were also synthesized on NF (Figure 2.5) using the same method.

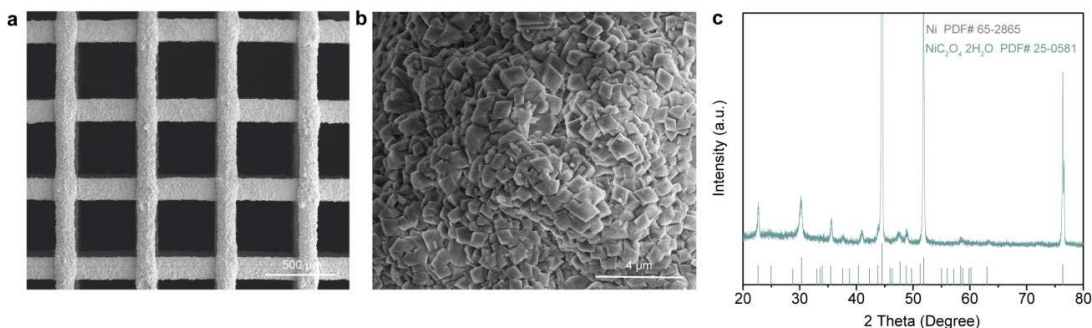


Figure 2.3 a, b) SEM images of $\text{NiC}_2\text{O}_4 \cdot 2\text{H}_2\text{O}/3\text{DPNi}$ collected at low and high magnifications, respectively. c) XRD pattern of the $\text{NiC}_2\text{O}_4 \cdot 2\text{H}_2\text{O}/3\text{DPNi}$.

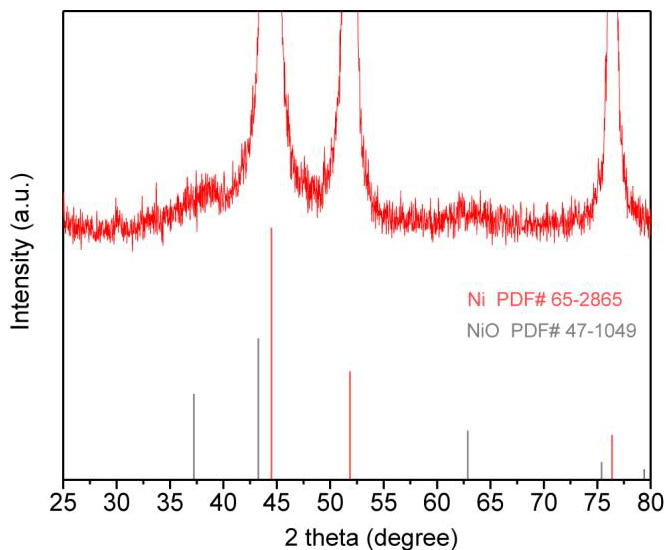


Figure 2.4 XRD pattern of $\text{NiC}_2\text{O}_4 \cdot 2\text{H}_2\text{O}$ powders collected after annealing in Argon.

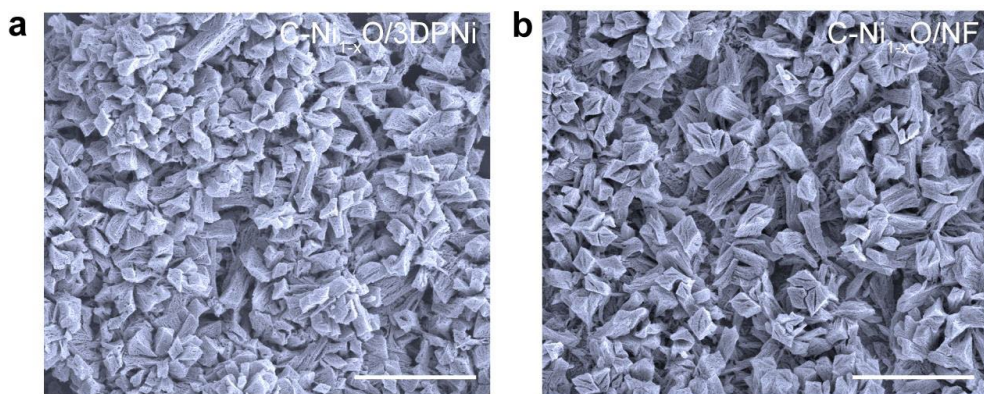


Figure 2.5 SEM images of the $\text{C-Ni}_{1-x}\text{O}$ grown on a) 3DPNi and b) NF, respectively. Scale bars are 4 μm .

To elucidate how the ordering of pores in 3D printed structures affects the bubble traffic, we examined gas bubble release behavior from the disordered C-

$\text{Ni}_{1-x}\text{O}/\text{NF}$ and the ordered $\text{C}-\text{Ni}_{1-x}\text{O}/3\text{DPNi}$ with gas injection experiments (Figure 2.6). In this setup, air was continuously injected at a rate of 1 mL s^{-1} through a syringe needle into two porous electrodes, each with a thickness of $\approx 2 \text{ mm}$. We used a high-speed camera to monitor the bubbles exiting the porous structure after passing through $\text{C}-\text{Ni}_{1-x}\text{O}/\text{NF}$ (Figure 2.6a) and $\text{C}-\text{Ni}_{1-x}\text{O}/3\text{DPNi}$ (Figure 2.6b) structures. Although the initial injection is a single large bubble, the $\text{C}-\text{Ni}_{1-x}\text{O}/\text{NF}$ structure splits the larger bubble into numerous smaller gas bubbles which exit the structure in what we characterize as a burst release with >10 bubbles exiting in a short period of time. In addition, the $\text{C}-\text{Ni}_{1-x}\text{O}/\text{NF}$ sample exhibits an interrupted period of 3131 ms ($t_2 = t_3 - t_1$, Figure 2.6a) during which no gas bubbles release from the structure, which is significantly longer than the interrupted period of 124 ms ($t_3 - t_0$, Figure 2.6b) observed for $\text{C}-\text{Ni}_{1-x}\text{O}/3\text{DPNi}$.

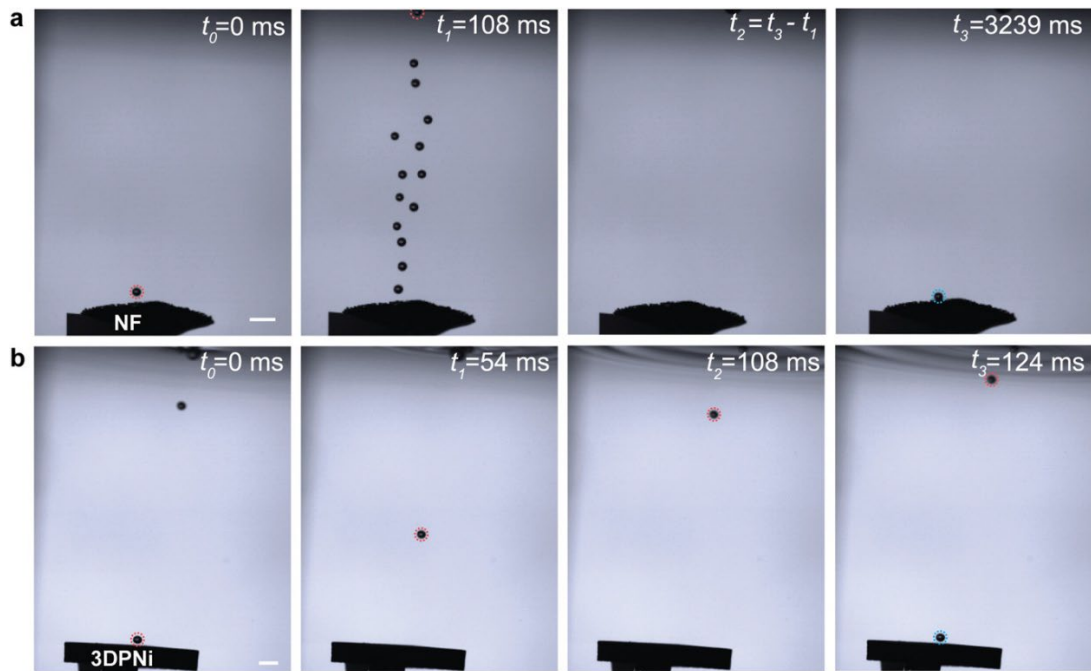


Figure 2.6 High-speed camera images of bubble release from C–Ni_{1-x}O/NF and C–Ni_{1-x}O/3DPNi. Side view high-speed camera images showing bubble release from a) C–Ni_{1-x}O/NF and b) C–Ni_{1-x}O/3DPNi structures at different periods of time. Scale bars are 2 mm. Red and blue dashed circles highlight the initial bubble in the first and second batch of bubble release, respectively.

To gain understanding of the different interruption periods for bubble release observed in Figure 2.6 for C–Ni_{1-x}O/NF versus C–Ni_{1-x}O/3DPNi, the gas bubble transport in the two samples was recorded from a top view using a high-speed camera. Figure 2.7a–c, g–i shows snapshot images extracted from the movies of C–Ni_{1-x}O/NF and C–Ni_{1-x}O/3DPNi, while Figure 2.7d–f, j–l shows the corresponding images with dashed lines highlighting the shapes of bubbles when transporting in the two structures. When a single gas bubble was initially injected into the C–Ni_{1-x}O/NF structure, the gas bubble movement is significantly influenced by the disordered pore structure of the NF skeleton, and typically experiences an in-plane movement first rather than through-plane movement to release. The bubble transport behaviors observed for the C–Ni_{1-x}O/NF electrode (Figure 2.7) can be rationalized by the stochastic structure of NF substrate. The gas bubble invades a pore when the pressure difference in the bubble and liquid is larger than the threshold entry pressure of the pore²⁵

$$P_{\text{bubble}} - P_{\text{liquid}} > 2\gamma \cos\theta / r_{\text{pore}} \quad (2.2)$$

where γ is the surface tension, θ is the contact angle taken in the liquid phase, and r_{pore} is the effective radius of pore, P_{bubble} and P_{liquid} are the pressure in bubble and liquid, respectively. The gas bubble prefers to occupy a larger pore because of its lower

threshold entry pressure. Owing to the random size and spatial distribution of the pores in NF, some pores in the through-plane direction may be smaller than those in the in-plane direction. As a result, the gas bubble initially invades in-plane rather than a through-plane, which is similar to a drainage process in which nonwetting phase replaces wetting phase in porous media (Figure 2.7e). If the in-plane pores adjacent to the bubble are smaller than those in the through-plane direction, then, as the gas pressure increased due to the continuous gas injection, the gas bubble invades the pores in the through-plane direction, and moves upward with the assistance of buoyancy (Figure 2.7f). When the gas bubble finally breaks through the surface of the porous NF, the large volume and the high pressure of the gas bubble resulted in the release of numerous small bubbles, as observed for C–Ni_{1-x}O /NF (t1, Figure 2.6a). It takes a long period for all of the gas bubbles to release from the NF since the gas bubble experiences in-plane invasion and suffers a pressure increase before breaking through the surface. By contrast, the periodically aligned pore structure of the 3DPNi lattice offers bubble flow channels that are parallel to the buoyance of the gas bubbles, which effectively suppresses the in-plane invasion or drainage process and minimized the pressure increase inside the 3D printed architecture, thereby reducing the gas breakthrough time (Figure 2.7j–l).

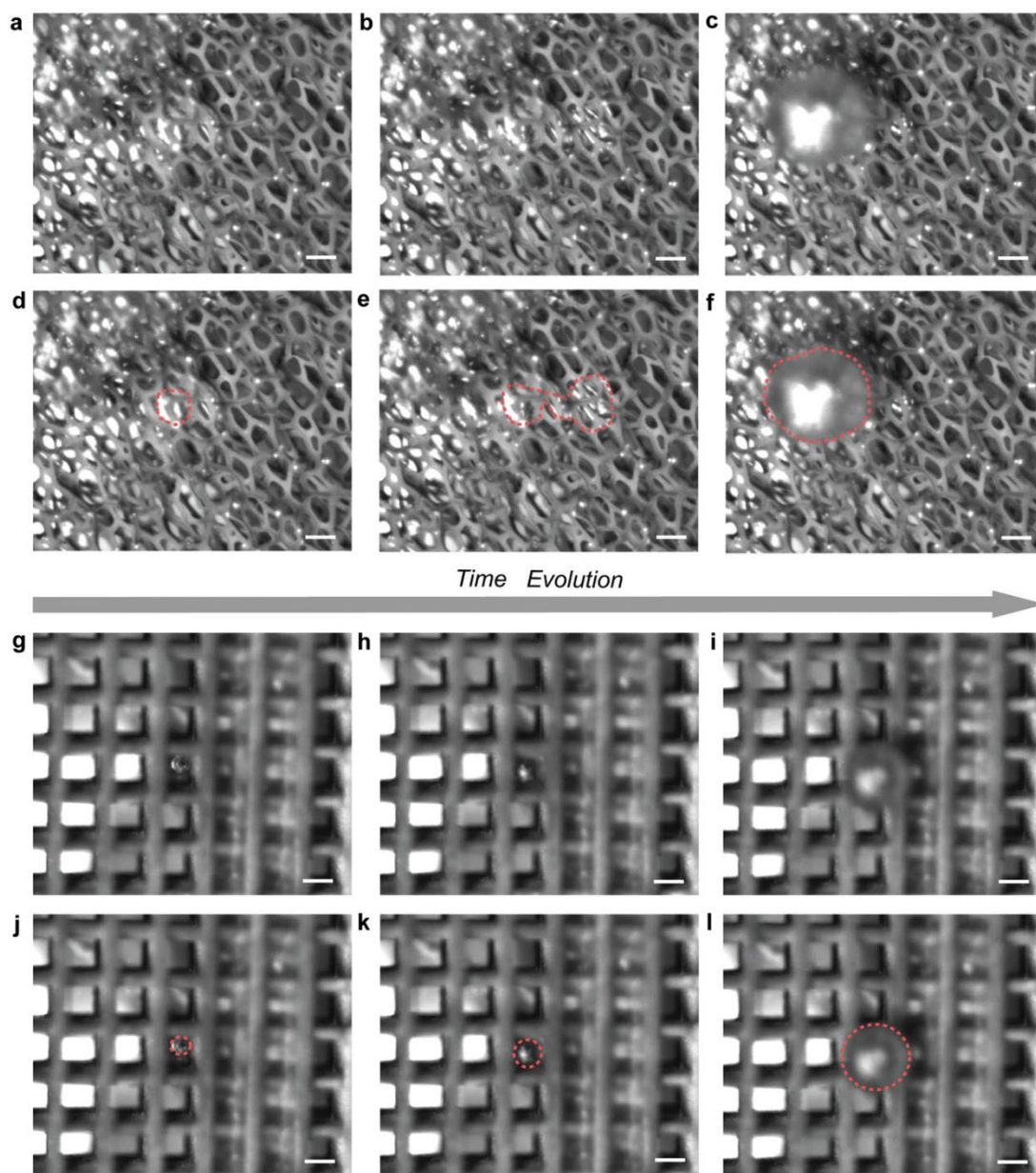


Figure 2.7 High-speed camera images of bubble transport through C-Ni_{1-x}O/NF and C-Ni_{1-x}O/3DPNi. Top view high-speed camera images of a–c) C-Ni_{1-x}O/NF and g–i) C-Ni_{1-x}O/3DPNi collected at different periods of time. d,e,j,k) The corresponding images with dashed lines highlighting the shape of bubbles during transport in the two

structures. f,) The images with dashed lines highlighting the bubble shape exiting the two structures. Scale bars are 500 μm .

To better understand how the pore arrangement affects the bubble diffusion through the 3D electrode, we constructed a computational model based on the Shan-and-Chen-type multicomponent, multiphase lattice Boltzmann method (see the Experimental Section for details). The model was used to investigate the migration of a single bubble through a porous medium as a function of bubble size and porous structure (periodic pores in 3DPNi and random pores in NF, Figure 2.8a,b). A buoyancy force was incorporated to drive the bubble transport (toward the +x-direction). We used the model to compute the time required for a bubble with different diameters to cross the yz-plane at the center of the porous structure, as summarized in Figure 2.8c.

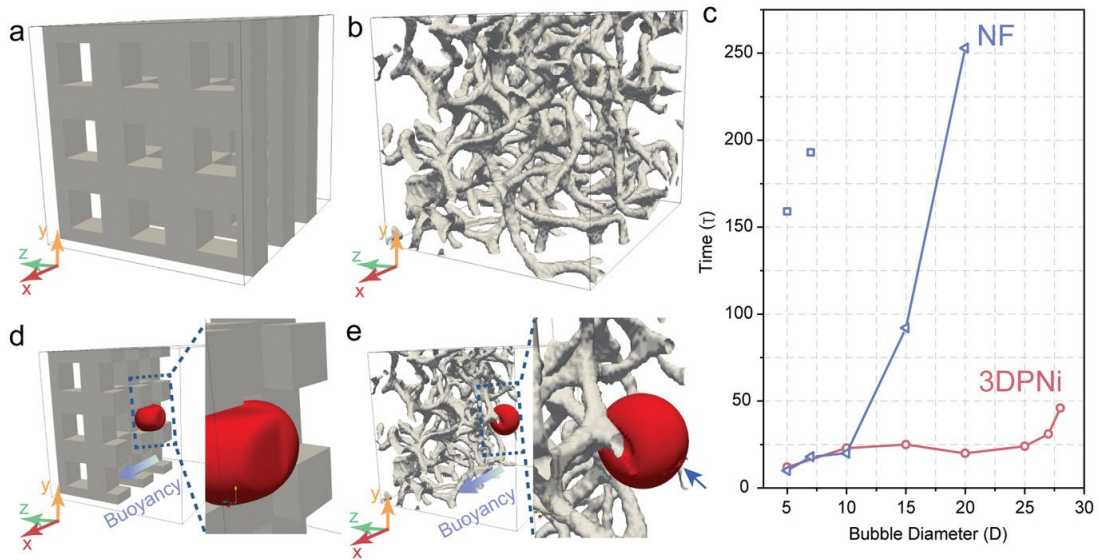


Figure 2.8 Structure model of a) 3DPNi and b) NF. c) Relative bubble migration time through 3DPNi and NF as a function of bubble diameter, determined by time to cross the central plane of the structure (units are dimensionless). The two square data points

represent the bubbles (diameter $d = 5$ and 7) entering the NF at different locations. d,e) Simulation frames showing bubble shape ($d = 20$) during transport in (d) 3DPNi and (e) NF. Arrow in the inset of (e) highlights an interaction with the NF surface, which is manifested through bubble deformation.

For a given porous structure, we find that there exists a critical bubble size, d_c , above which the bubble is incapable of passing through but is instead trapped in the porous medium. It is clear that d_c in the periodic 3DPNi structure ($d_c = 29$) is larger than the random NF structure ($d_c = 20$). As seen from Figure 2.8d, when the diameter of the bubble ($d = 20$) exceeds the size of the cuboidal pore of 3DPNi, the gas bubble can be deformed and squeezes to pass through the pore channel in the periodic structure. The portion of the bubble in contact with the solid beams takes the shape of the channel, while the remaining portion in the liquid electrolyte appears as a spherical cap to minimize the surface energy. Increasing the bubble size increases the traveling velocity (as expected from the Stokes equation, according to which velocity is proportional to square of the bubble diameter), while also requiring a larger deformation to pass through the channel, which offsets the contribution of size to increased traveling speed. Note that the leading portion of the spherical cap (along $+x$) will not encounter or collide with any solid beams when traveling through the channel. Once the bubble size exceeds d_c , only a small portion of the bubble can be deformed and squeezed into the channel. The remaining portion is blocked by the solid elements since the gravitational force cannot induce the bubble deformation necessary to escape the confined pore.

In random porous media such as NF, a gas bubble of the same size ($d = 20$) can also deform upon contact with solid elements within the porous structure (Figure 2.8e). However, due to the random distribution of the pore structure, the bubble experiences frequent collisions and deformations (highlighted by the arrow in Figure 2.8e), which increases the bubble travel distance. Moreover, unlike the relatively large through-hole vias found in the periodic structure that facilitate rapid bubble transport, the varying pore sizes and tortuous paths of the nonperiodic structure cause the leading portion of the bubble to regularly encounter the solid network ahead of it. The resulting forces exerted on the bubble by the solid beams counteract the effect of the buoyancy, slowing the migration. The importance of this interaction is highlighted by the fact that the traveling path—and thus transport time of the bubble—is sensitive to the specific entry point of the bubble into the solid network structure (as an illustration, the square data points in Figure 2.8c show examples of much longer migration time and smaller d_c that can result if the entrance location is changed). We point out that although our simulations consider transport of only a single gas bubble, the physical mechanisms governing the relationship between bubble size and transport kinetics should be qualitatively unchanged at higher current densities, for which bubble interactions may introduce additional complexity.

We hypothesized that a rapid escape of gas bubbles out of the ordered 3D electrodes would decrease the concentration of bubbles per unit of volume for a given period of time and, thus, suppress bubble coalescence. To confirm this hypothesis, we performed water splitting experiments using C–Ni_{1-x}O /NF (Figure 2.9a) and C–

$\text{Ni}_{1-x}\text{O}/3\text{DPNi}$ (Figure 2.9b) as bifunctional electrodes. The gas evolution reactions on both electrodes were recorded by a high-speed camera. Significantly, more gas bubbles were generated on HER electrodes (Figure 2.9a,b) compared to OER electrodes, because water electrolysis generates oxygen gas and hydrogen gas in a 1:2 ratio. Notably, more and considerably larger size gas bubbles were found dwelling on the C- $\text{Ni}_{1-x}\text{O}/\text{NF}$ electrodes (Figure 2.9a) compared to the C- $\text{Ni}_{1-x}\text{O}/3\text{DPNi}$ electrodes (Figure 2.9b). The in-plane gas invasion in NF also increases the number of gas bubbles per unit volume. Bubble coalescence tends to occur when a high number of gas bubbles are confined in a small volume, which increases the probability of bubble collisions²⁶ and merging of adjacent bubbles is thermodynamically favorable as it reduces the overall surface energy. However, an increase of bubble volume would cover more catalytic sites, further reducing the overall reaction rate of water electrolysis. As illustrated in Figure 2.10a, the disordered porous structure of NF causes serious bubble coalescence (highlighted in dashed box), which consequently blocks the pores of NF and further interrupting the inward flow of the electrolyte into NF. By contrast, periodic channels in 3DPNi facilitate bubble flow and greatly suppress bubble coalescence (Figure 2.10b), which enhances the diffusion of surrounding electrolyte into electrode.

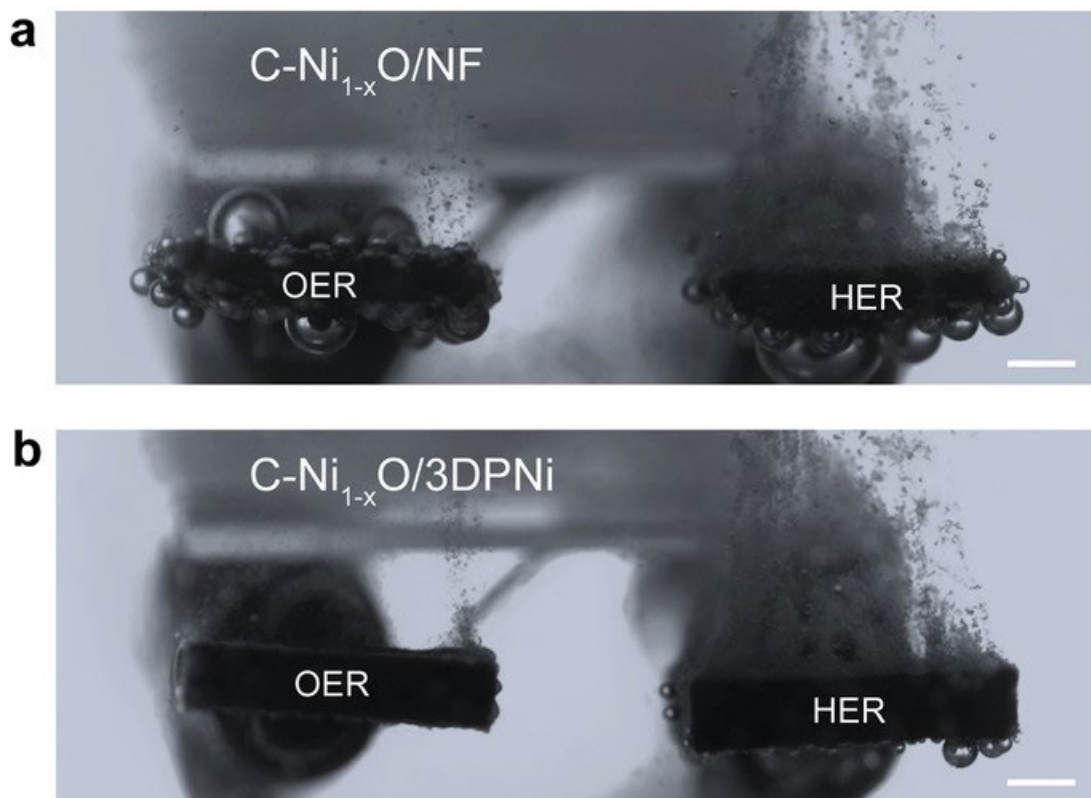


Figure 2.9 Gas bubble coalescence and release for C-Ni_{1-x}O/NF and C-Ni_{1-x}O/3DPNi electrodes during water electrolysis. High-speed camera images collected from the a) C-Ni_{1-x}O/NF and b) C-Ni_{1-x}O/3DPNi electrodes during water electrolysis. Scale bars are 2 mm.

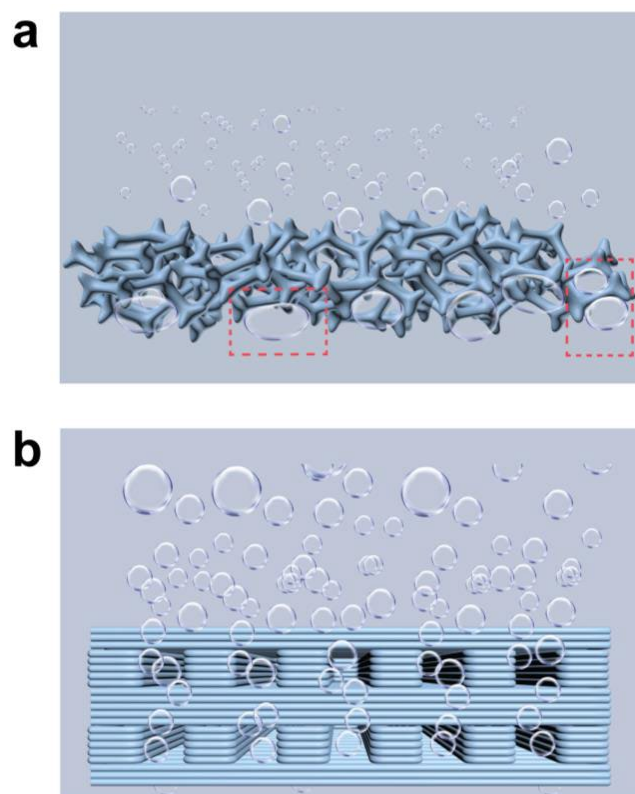


Figure 2.10 Schematic illustrations of bubble coalescence and migration. a) C-Ni_{1-x}O/NF and b) C-Ni_{1-x}O/3DPNi, respectively. Dashed box highlighting the coalescence of adjacent gas bubbles.

High-speed imaging experiments prove that the 3D printed ordered porous structure better suppresses bubble coalescence and enhances bubble release compared to its stochastic foam counterpart, so C-Ni_{1-x}O/3DPNi was proposed to have better catalytic performance for water splitting, especially at high current densities. We measured the performance of C-Ni_{1-x}O/NF and C-Ni_{1-x}O/3DPNi as electrodes for water electrolysis in alkaline medium (Figure 2.11). We believe that any discrepancy in performance should be attributed to the structural differences between the two

porous electrodes since C–Ni_{1-x}O nanorods decorating the surface were used as bifunctional HER/OER catalysts for both NF and 3DPNi electrodes. HER polarization curves of C–Ni_{1-x}O/3DPNi and C–Ni_{1-x}O/NF were collected in nitrogen-gas-saturated 1.00 M KOH at a low scan rate of 0.1 mV s⁻¹ (Figure 2.11a). C–Ni_{1-x}O/NF and C–Ni_{1-x}O/3DPNi used for the measurements have the same geometric dimensions (10 mm × 2 mm × 3 mm) for fair comparison. Significantly, C–Ni_{1-x}O/3DPNi delivers much larger current density than that of C–Ni_{1-x}O/NF at the same overpotentials (iR corrected, Figure 2.12). C–Ni_{1-x}O/3DPNi achieves an ultrahigh geometric current density (j_{geo}) of 1000 mA cm⁻² at an overpotential of 245 mV, while at the same overpotential, C–Ni_{1-x}O/NF merely delivers a j_{geo} of 79.5 mA cm⁻². The performance of C–Ni_{1-x}O/3DPNi at large current densities is also substantially better than the values previously reported for Ni- or Fe-based HER catalysts at the same current density (Figure 2.11b).

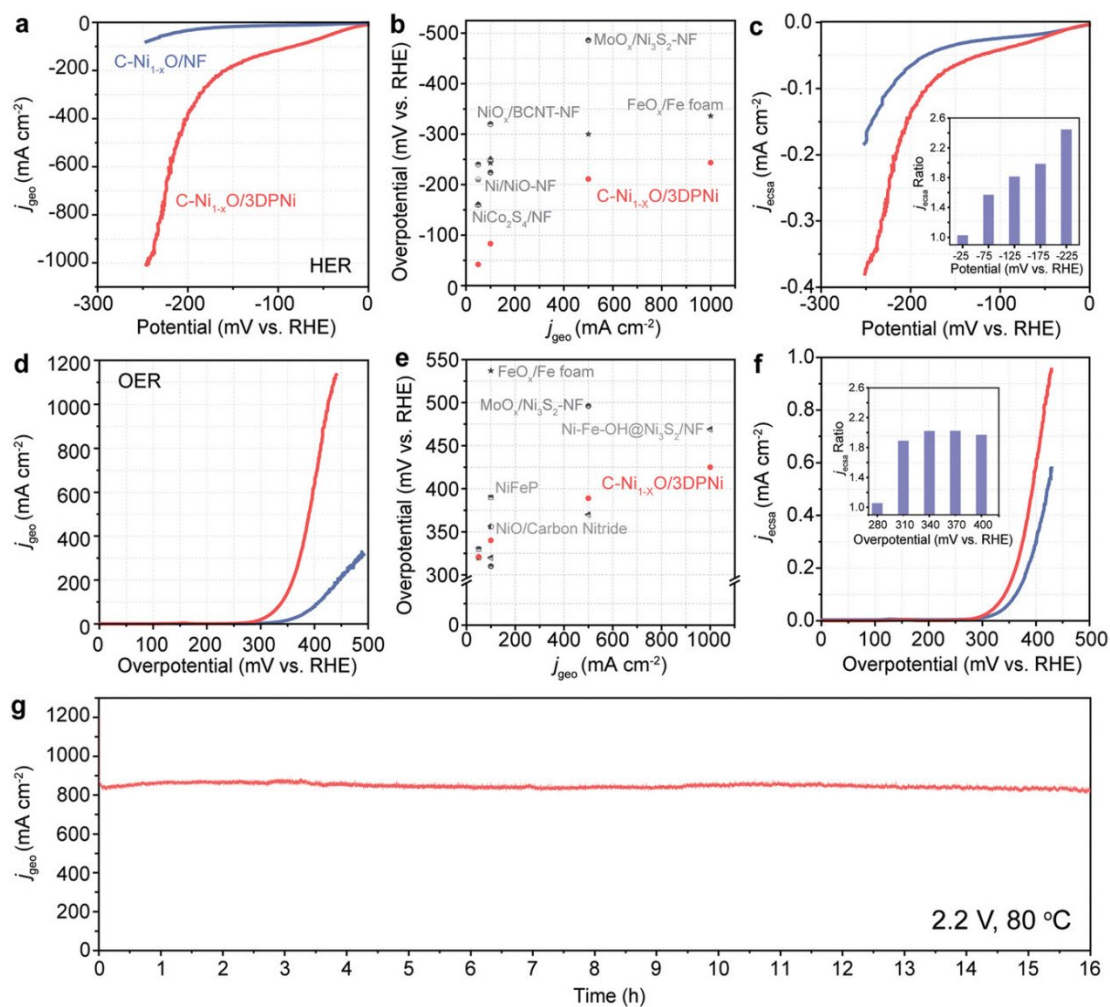


Figure 2.11 Electrochemical performance of C–Ni_{1-x}O/NF and C–Ni_{1-x}O/3DPNi during water electrolysis. Polarization curves of C–Ni_{1-x}O/NF and C–Ni_{1-x}O/3DPNi collected in 1.00 M KOH at a scan rate of 0.1 mV s⁻¹ for a) HER and d) OER. b,e) Plots to compare HER and OER overpotentials (η) of C–Ni_{1-x}O/3DPNi (0.1 mV s⁻¹) obtained at $j_{\text{geo}} = 50, 100, 500,$ and 1000 mA cm^{-2} , with (b) HER catalysts, including Ni/NiO–NF (2 mV s⁻¹),²⁷ NiOx@bamboo-like carbon nanotubes–NF (5 mV s⁻¹),²⁸ NiCo₂S₄/NF (2 mV s⁻¹),²⁹ MoO_x/Ni₃S₂–NF (0.1 mV s⁻¹),⁶ FeO_x/Fe foam (0.1 mV s⁻¹);³⁰ and (e) OER catalysts, including NiO/carbon nitride (10 mV s⁻¹),³¹ FeO_x/Fe

foam (0.1 mV s^{-1}),³⁰ NiFeP (20 mV s^{-1}),³² $\text{MoO}_x/\text{Ni}_3\text{S}_2\text{-NF}$ (0.1 mV s^{-1}),⁶ and $\text{Ni-Fe-OH@Ni}_3\text{S}_2/\text{NF}$ (0.5 mV s^{-1})³³ in 1.00 M KOH electrolyte. c,f) Polarization curves shown in (a) and (d) with current normalized to the electrode's ECSA. The j_{ECSA} ratios (refers to the ratio of j_{ECSA} of $\text{C-Ni}_{1-x}\text{O}/3\text{DPNi}$ to j_{ECSA} of $\text{C-Ni}_{1-x}\text{O}/\text{NF}$) are plotted as a function of overpotential for HER (inset of (c)) and OER (inset of (f)). g) Chronoamperometry curve collected from a water electrolysis device, using $\text{C-Ni}_{1-x}\text{O}/3\text{DPNi}$ as OER and HER electrodes, at 2.2 V in 1.00 M KOH electrolyte at 80°C .

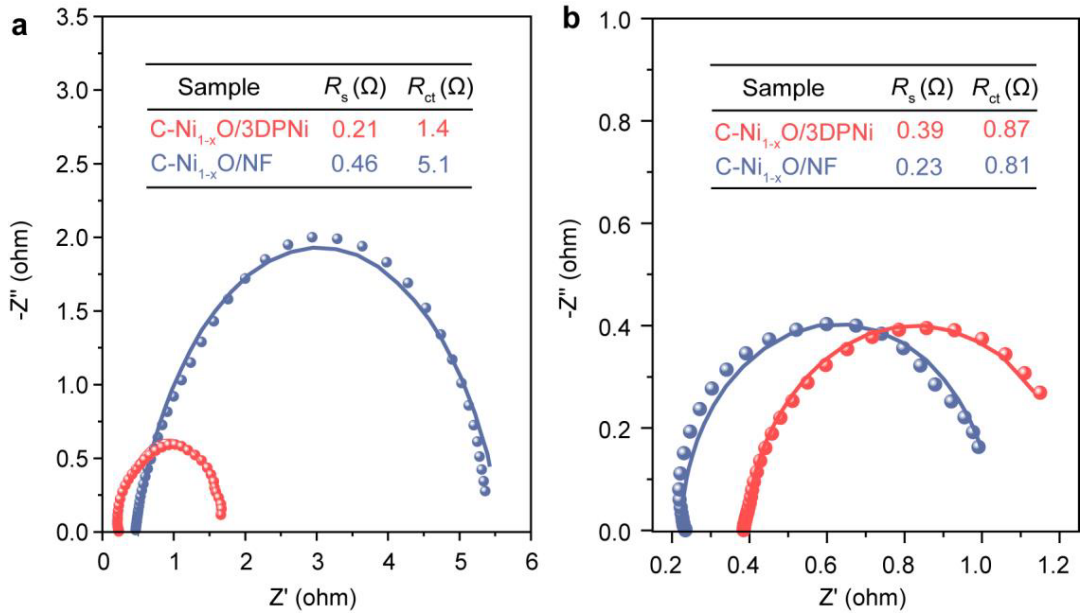


Figure 2.12 EIS spectra of the $\text{C-Ni}_{1-x}\text{O}/3\text{DPNi}$ and $\text{C-Ni}_{1-x}\text{O}/\text{NF}$. a) HER and b) OER, with dot representing experimental data and curve representing simulated results, insets are the tables showing the solution resistance (R_s) and charge transfer resistance (R_{ct}).

The total electrode activity is determined by its intrinsic activity and extrinsic activity and, since we used the same catalyst $\text{C-Ni}_{1-x}\text{O}$ for both 3DPNi and NF

electrodes, both electrodes are expected to possess the same intrinsic activity. Therefore, the increased total electrode activity observed for C–Ni_{1-x}O/3DPNi should be attributed to a larger number of available catalytically active sites. The ECSA of C–Ni_{1-x}O/3DPNi is typically 4–5 times higher than C–Ni_{1-x}O/NF, however, enhanced ECSA alone cannot explain the order of magnitude difference in electrode activity between the two electrodes. It is noteworthy that the availability of catalytically active sites varies with the measurement conditions. For instance, bubble trapping and coalescence can block a significant portion of active sites and severely limit the electrode's extrinsic activity at high current densities. Normalizing the HER current to ECSA (denoted as j_{ECSA}) allows direct comparison of the specific reaction rate of C–Ni_{1-x}O/3DPNi and C–Ni_{1-x}O/NF and, thus, unveils the effectiveness for each electrode to release gas bubbles. As expected, C–Ni_{1-x}O/3DPNi shows a considerably larger j_{ECSA} than that of C–Ni_{1-x}O/NF (Figure 2.11c), especially at higher applied potentials. The inset of Figure 2.11c shows that the j_{ECSA} ratio of C–Ni_{1-x}O/3DPNi to C–Ni_{1-x}O/NF increases from 1 to about 2.5 with the applied HER potential.

Similarly, the total electrode activities of C–Ni_{1-x}O/NF and C–Ni_{1-x}O/3DPNi for OER were also investigated by linear sweep voltammetry at a scan rate of 0.1 mV s⁻¹ in oxygen-saturated 1.00 M KOH. C–Ni_{1-x}O/3DPNi again shows higher geometric current densities than that of C–Ni_{1-x}O/NF (Figure 2.11d) at all potentials (iR corrected, Figure 2.12). At 425 mV, C–Ni_{1-x}O/3DPNi achieves a large current density of 1000 mA cm⁻², which is much higher than the value of 143.5 mA cm⁻² for C–Ni_{1-x}O/NF obtained at the same overpotential. The demonstrated ability to achieve

large geometric current densities makes C-Ni_{1-x}O/3DPNi a promising electrode for OER (Figure 2.11e). The rod-like structure of C-Ni_{1-x}O was mostly retained after OER measurement. C-Ni_{1-x}O/3DPNi also shows consistently larger j_{ECSA} than that of C-Ni_{1-x}O/NF (Figure 2.11f), although the j_{ECSA} ratio of C-Ni_{1-x}O/3DPNi to C-Ni_{1-x}O/NF did not change significantly as a function of overpotentials (inset of Figure 2.11f) because less bubbles are formed during OER at the same current density. Importantly, both HER and OER results support our hypothesis that the ordered porous structure enhances bubble transport and release compared to its disordered porous counterpart.

To further understand how the pore size affects the catalytic performance of 3DPNi, we prepared two additional 3DPNi samples with pore sizes of 150 and 750 μm by adjusting the filament center-to-center distance (Figure 2.13). As shown in Figure 2.14a,b, all three 3D printed electrodes have higher HER/OER total electrode activity (current density) than that of C-Ni_{1-x}O/NF at the same potential, which demonstrates that 3D printed electrodes deliver large current for water splitting and superior performance over their stochastic foam counterparts. The absolute value of current density is related to the electrode ECSA. To investigate the interplay between the electrode structure and its catalytic performance (related to bubble releasing capability), we must remove the effect of the ECSA. Therefore, we normalized the current to the ECSA of each sample (Figure 2.14c,d). For HER, C-Ni_{1-x}O/3DPNi electrodes with pore sizes of 150 and 450 μm exhibit comparable j_{ECSA} (Figure 2.14c). The j_{ECSA} values of these two electrodes are higher than that of the C-Ni_{1-x}O/NF, but considerably lower than the 3D printed electrode with larger pore size (750 μm). The

results suggest that the performances of the 150 and 450 μm pore size samples are limited by the inefficiency of the bubble release process due to the relatively small pore sizes and bubble traffic that occurs when a large volume and number of hydrogen gas bubbles are generated at high current/potential (although performance is still better than the control sample NF). Bubble release efficiency is improved by increasing the pore size to 750 μm . For OER, since fewer gas bubbles are generated compared to HER at the same current, the performance of electrodes with larger pore sizes (NF, 450 and 750 μm samples) is less dependent on the bubbles. However, when the pore size is decreased to 150 μm , the performance becomes more dependent on the bubble transport behavior (Figure 2.14d). The results confirm that gas bubble release is more favorable in an electrode structure with larger pore size with the trade-off being larger pores leading to less ECSA per unit volume, which points to some optimal 3D electrode structure for overall reactivity. For example, whether the performance of a 3D electrode will be limited by the bubble effect depends on the size of pores and their spatial distribution (e.g., ordered vs random structure) as well as the amount and size of gas bubbles that are generated. To explore the stability of our 3D printed electrodes over time, we assembled and tested a water electrolysis device in a two-electrode configuration using bifunctional C–Ni_{1-x}O/3DPNi (450 μm sample) for both HER and OER electrodes. Figure 2.15 shows the chronoamperometry curve of the device collected in 1.00 M KOH electrolyte at room temperature, a large current density of 600 mA cm⁻² can be stably delivered at the voltage of 2.56 V for about 50 h. In addition, we also tested the device's stability at 80 °C, which is a common temperature for

industrial water electrolysis. The device exhibits a stable large current density of 850 mA cm⁻² at 2.2 V for at least 16 h (Figure 2.11). The current density achieved by this device is better than many industrial AWS results under similar conditions.¹ Therefore, we believe that C-Ni_{1-x}O/3DPNi is a promising catalyst and electrode structure for industrial scale alkaline water electrolysis.

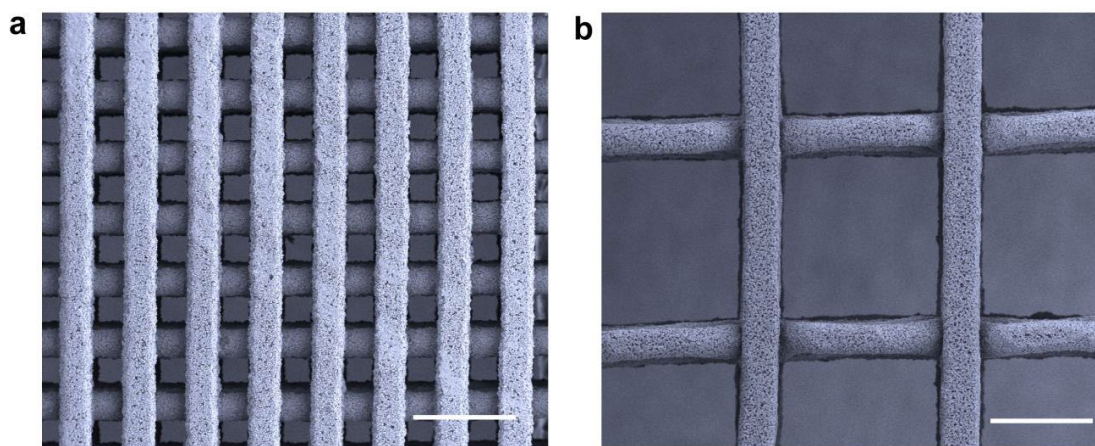


Figure 2.13 SEM images of the C-Ni_{1-x}O/3DPNi samples with printed pore sizes of a) 150 μm, and b) 750 μm. Scale bars are 500 μm.

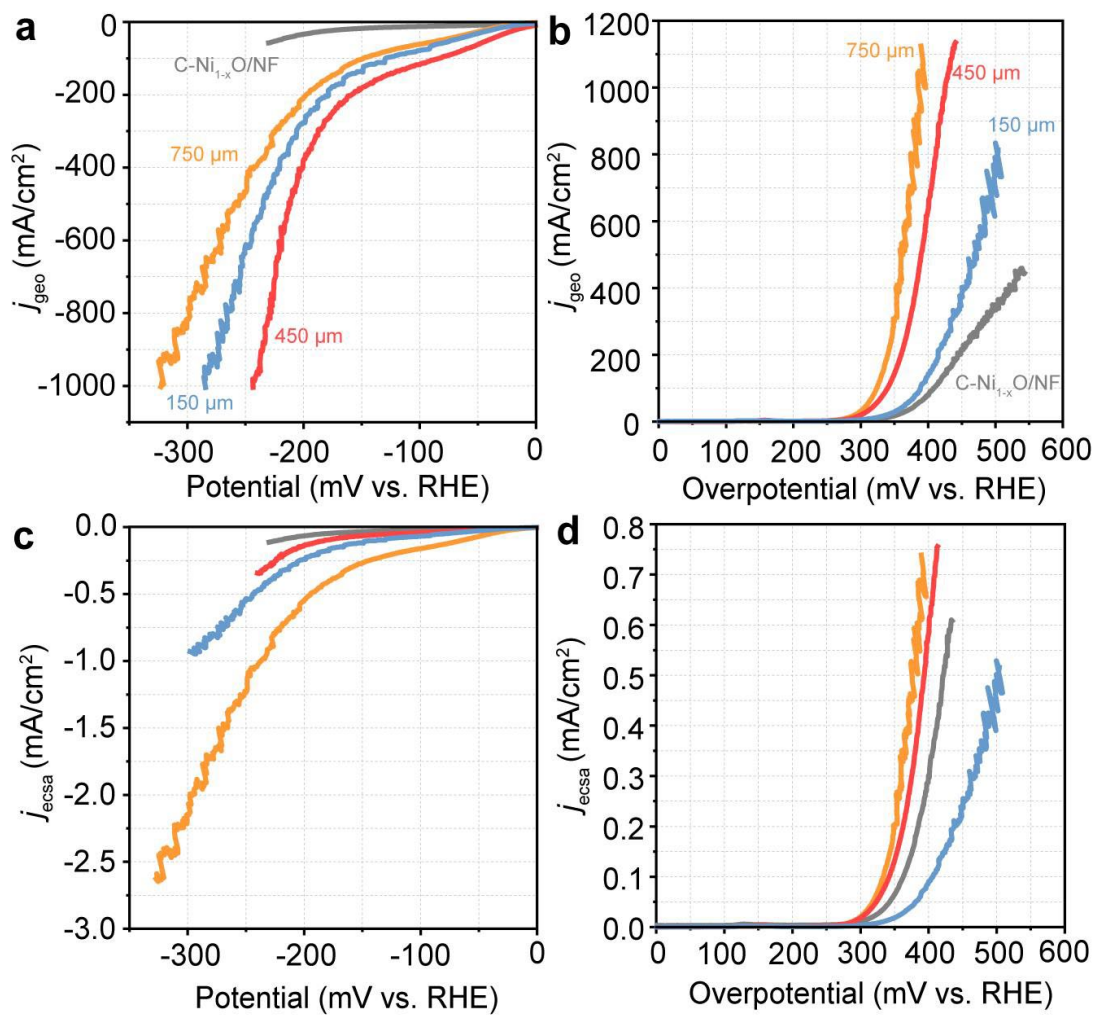


Figure 2.14 Polarization curves of the C-Ni_{1-x}O/NF and C-Ni_{1-x}O/3DPNi with different pore size (150, 450 and 750 μm) collected in 1.00 M KOH for a) HER and b) OER at the scan rate of 0.1 mV s⁻¹. c) and d) are the polarization curves in a) and b) with current normalized to electrochemical surface area.

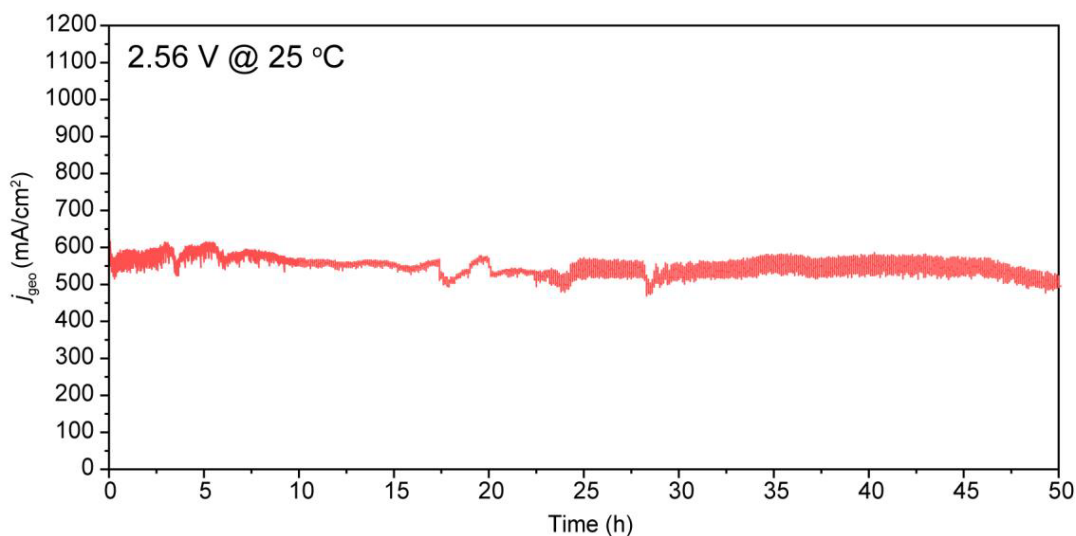


Figure 2.15 Chronoamperometry curve of the full water splitting with C-Ni_{1-x}O/3DPNi as HER and OER electrodes at the voltage of 2.56 V and room temperature.

2.4 Conclusion

In summary, we have demonstrated that the 3D printed electrodes with periodic pore structures facilitate gas bubble transport and release, which maintains accessibility of a large portion of catalytic active sites to electrolyte and grants high specific reaction rates even at high current densities. As a result, C-Ni_{1-x}O/3DPNi achieved significantly lower HER and OER overpotentials than C-Ni_{1-x}O/NF at the same current densities. These findings provide important insights for designing high-performance catalyst/electrode structures for high current (high rate) water electrolysis. We note that our 3DPNi electrode structure has not undergone rigorous optimization for gas bubble transport and release, so there remains room for further performance improvements. For example, computational simulations of gas bubble generation and transport

behavior could serve as the basis for design optimization of 3D electrodes via inverse methods and, when combined with the design space achievable with 3D printing techniques, we envision the construction of complex structures with even greater performance characteristics. Finally, we posit that this new ordered 3D electrode paradigm will deliver performance improvement not only for water electrolysis, but for any electrochemical reactions involving gas consumption or generation.

References

1. A. Buttler, H. Spliethoff, *Renewable Sustainable Energy Rev.* **2018**, *82*, 2440-2454.
2. J. Wang, F. Xu, H. Jin, Y. Chen, Y. Wang, *Adv. Mater.* **2017**, *29*, 1605838.
3. N. Mahmood, Y. Yao, J.-W. Zhang, L. Pan, X. Zhang, J.-J. Zou, *Adv. Sci.* **2018**, *5*, 1700464.
4. W. Ju, M. V. F. Heinz, L. Pusterla, M. Hofer, B. Fumey, R. Castiglioni, M. Pagani, C. Battaglia, U. F. Vogt, *ACS Sustainable Chem. Eng.* **2018**, *6*, 4829-4837.
5. P. Chakthranont, J. Kibsgaard, A. Gallo, J. Park, M. Mitani, D. Sokaras, T. Kroll, R. Sinclair, M. B. Mogensen, T. F. Jaramillo, *ACS Catal.* **2017**, *7*, 5399-5409.
6. a) Y. Wu, G.-D. Li, Y. Liu, L. Yang, X. Lian, T. Asefa, X. Zou, *Adv. Funct. Mater.* **2016**, *26*, 4839-4847; b) X. Zou, Y. Zhang, *Chem. Soc. Rev.* **2015**, *44*, 5148-5180.

7. T. Kou, M. Chen, F. Wu, T. J. Smart, S. Wang, Y. Wu, Y. Zhang, S. Li, S. Lall, Z. Zhang, Y.-S. Liu, J. Guo, G. Wang, Y. Ping, Y. Li, *Nat. Commun.* **2020**, *11*, 590.
8. J. W. D. Ng, M. García-Melchor, M. Bajdich, P. Chakthranont, C. Kirk, A. Vojvodic, T. F. Jaramillo, *Nat. Energy* **2016**, *1*, 16053.
9. K. Zeng, D. Zhang, *Prog. Energy Combust. Sci.* **2010**, *36*, 307-326.
10. J. Luo, J.-H. Im, M. T. Mayer, M. Schreier, M. K. Nazeeruddin, N.-G. Park, S. D. Tilley, H. J. Fan, M. Grätzel, *Science* **2014**, *345*, 1593-1596.
11. L. Wang, X. Huang, S. Jiang, M. Li, K. Zhang, Y. Yan, H. Zhang, J. M. Xue, *ACS Appl. Mater. Interfaces* **2017**, *9*, 40281-40289.
12. a) C. Zhu, T. Y.-J. Han, E. B. Duoss, A. M. Golobic, J. D. Kuntz, C. M. Spadaccini, M. A. Worsley, *Nat. Commun.* **2015**, *6*, 6962; b) C. Zhu, Z. Qi, V. A. Beck, M. Luneau, J. Lattimer, W. Chen, M. A. Worsley, J. Ye, E. B. Duoss, C. M. Spadaccini, C. M. Friend, J. Biener, *Sci. Adv.* **2018**, *4*, eaas9459.
13. L. F. Arenas, C. Ponce de León, F. C. Walsh, *Electrochem. Commun.* **2017**, *77*, 133-137.
14. a) A. Ambrosi, M. Pumera, *ACS Sustainable Chem. Eng.* **2018**, *6*, 16968-16975; b) A. Ambrosi, M. Pumera, *Adv. Funct. Mater.* **2018**, *28*, 1700655; c) X. Su, X. Li, C. Y. A. Ong, T. S. Heng, Y. Wang, E. Peng, J. Ding, *Adv. Sci.* **2019**, *6*, 1801670; d) J. T. Davis, J. Qi, X. Fan, J. C. Bui, D. V. Esposito, *Int. J. Hydrogen Energy* **2018**, *43*, 1224-1238; e) J. C. Bui, J. T. Davis, D. V. Esposito, *Sustainable Energy Fuels* **2020**, *4*, 213-225.

15. a) D. T. Nguyen, C. Meyers, T. D. Yee, N. A. Dudukovic, J. F. Destino, C. Zhu, E. B. Duoss, T. F. Baumann, T. Suratwala, J. E. Smay, R. Dylla-Spears, *Adv. Mater.* **2017**, *29*, 1701181; b) K. T. Sullivan, C. Zhu, E. B. Duoss, A. E. Gash, D. B. Kolesky, J. D. Kuntz, J. A. Lewis, C. M. Spadaccini, *Adv. Mater.* **2016**, *28*, 1934-1939.
16. E. B. Duoss, T. H. Weisgraber, K. Hearon, C. Zhu, W. Small IV, T. R. Metz, J. J. Vericella, H. D. Barth, J. D. Kuntz, R. S. Maxwell, C. M. Spadaccini, T. S. Wilson, *Adv. Funct. Mater.* **2014**, *24*, 4905-4913.
17. S. Mooraj, S. S. Welborn, S. Jiang, S. Peng, J. Fu, S. Baker, E. B. Duoss, C. Zhu, E. Detsi, W. Chen, *Scr. Mater.* **2020**, *177*, 146-150.
18. S. Chandrasekaran, B. Yao, T. Liu, W. Xiao, Y. Song, F. Qian, C. Zhu, E. B. Duoss, C. M. Spadaccini, Y. Li, M. A. Worsley, *Mater. Horiz.* **2018**, *5*, 1166-1175.
19. N. P. Brandon, G. H. Kelsall, *J. Appl. Electrochem.* **1985**, *15*, 475-484.
20. C. Yu, X. Zhu, K. Li, M. Cao, L. Jiang, *Adv. Funct. Mater.* **2017**, *27*, 1701605.
21. H. Vogt, *Electrochim. Acta* **1993**, *38*, 1421-1426.
22. a) G. J. H. Lim, Z. Lyu, X. Zhang, J. J. Koh, Y. Zhang, C. He, S. Adams, J. Wang, J. Ding, *J. Mater. Chem. A* **2020**, *8*, 9058-9067; b) D. Zhang, W. Jonhson, T. S. Heng, Y. Q. Ang, L. Yang, S. C. Tan, E. Peng, H. He, J. Ding, *Mater. Horiz.* **2020**, *7*, 1083-1090.
23. W. Yang, G. Cheng, C. Dong, Q. Bai, X. Chen, Z. Peng, Z. Zhang, *J. Mater. Chem. A* **2014**, *2*, 20022-20029.

24. Z. Lu, W. Zhu, X. Yu, H. Zhang, Y. Li, X. Sun, X. Wang, H. Wang, J. Wang, J. Luo, X. Lei, L. Jiang, *Adv. Mater.* **2014**, *26*, 2683-2687.
25. a) D. F. do Nascimento, J. R. Vimieiro Junior, S. Paciornik, M. S. Carvalho, *Sci. Rep.* **2019**, *9*, 12333; b) P. C. Reeves, M. A. Celia, *Water Resour. Res.* **1996**, *32*, 2345-2358.
26. G. A. Bokkers, J. A. Laverman, M. van Sint Annaland, J. A. M. Kuipers, *Chem. Eng. Sci.* **2006**, *61*, 5590-5602.
27. X. Yan, L. Tian, X. Chen, *J. Power Sources* **2015**, *300*, 336-343.
28. J. Wang, S. Mao, Z. Liu, Z. Wei, H. Wang, Y. Chen, Y. Wang, *ACS Appl. Mater. Interfaces* **2017**, *9*, 7139-7147.
29. L. Ma, Y. Hu, R. Chen, G. Zhu, T. Chen, H. Lv, Y. Wang, J. Liang, H. Liu, C. Yan, H. Zhu, Z. Tie, Z. Jin, J. Liu, *Nano Energy* **2016**, *24*, 139-147.
30. X. Zou, Y. Wu, Y. Liu, D. Liu, W. Li, L. Gu, H. Liu, P. Wang, L. Sun, Y. Zhang, *Chem* **2018**, *4*, 1139-1152.
31. C. Liao, B. Yang, N. Zhang, M. Liu, G. Chen, X. Jiang, G. Chen, J. Yang, X. Liu, T.-S. Chan, Y.-J. Lu, R. Ma, W. Zhou, *Adv. Funct. Mater.* **2019**, *29*, 1904020.
32. Z. Liu, G. Zhang, K. Zhang, H. Liu, J. Qu, *ACS Sustainable Chem. Eng.* **2018**, *6*, 7206-7211.
33. X. Zou, Y. Liu, G.-D. Li, Y. Wu, D.-P. Liu, W. Li, H.-W. Li, D. Wang, Y. Zhang, X. Zou, *Adv. Mater.* **2017**, *29*, 1700404.

34. P. Ganesh, R. Giri, R. Kaul, P. Ram Sankar, P. Tiwari, A. Atulkar, R. K. Porwal, R. K. Dayal, L. M. Kukreja, *Mater. Des.* **2012**, *39*, 509-521.
35. a) J. Latt, O. Malaspinas, D. Kontaxakis, A. Parmigiani, D. Lagrava, F. Brogi, M. B. Belgacem, Y. Thorimbert, S. Leclaire, S. Li, F. Marson, J. Lemus, C. Kotsalos, R. Conradin, C. Coreixas, R. Petkantchin, F. Raynaud, J. Beny, B. Chopard, *Comput. Math. with Appl.* **2020**, <https://doi.org/10.1016/j.camwa.2020.03.022>; b) J. E. Santos, A. Bihani, C. J. Landry, Git code **2019**, <https://doi.org/10.5281/zenodo.3842279>.
36. a) H. Huang, D. T. Thorne, M. G. Schaap, M. C. Sukop, *Phys. Rev. E* **2007**, *76*, 066701; b) J. E. Santos, M. Prodanović, C. J. Landry, H. Jo, in *Proceeding of the 6th Unconventional Resources Technology Conference*, (Eds: J. Stratton, D. Valleau, S. Maxwell), Unconventional Resources Technology Conference, **2018**, 2542.
37. J. E. Santos, *Master Thesis*, The University of Texas at Austin, **2018**.
38. R. Silva, D. Voiry, M. Chhowalla, T. Asefa, *J. Am. Chem. Soc.* **2013**, *135*, 7823-7826.

Chapter 3

Introduction of Electrochemical CO₂ Reduction

Abstract

In comparison with conventional methods, electrochemical CO₂ reduction (CO₂RR) represents a promising and environmentally friendly method to generate value-added products and mitigate anthropogenic climate change. Importantly, with the increasing prevalence of wind and solar power, the cost of electricity continues to decrease. Abundant and low-cost renewable electrical energy sources make electrochemical reduction of CO₂ an attractive and promising solution for CO₂ mitigation.

3.1 Background

In 2013, carbon dioxide (CO₂) concentration in the atmosphere reached 400 parts per million for the first time in human history. The rise of CO₂ levels is believed to be one of the major reasons for the anthropogenic climate change. We can achieve a dual benefit by converting atmospheric CO₂ to value-added chemicals. Recently, enormous effort has recently been devoted to exploring novel catalysts for electrochemical CO₂ reduction reactions (CO₂RR), with a goal of achieving improved selectivity, activity, and stability.

3.2 Basic Mechanisms

Significant progress has been accomplished in the theoretical understanding of electrochemical CO₂RR, especially with respect to the reaction mechanisms for formation of C₁ products (e.g., carbon monoxide [CO], formate [HCOO⁻]). Tin (Sn)-

based,^{1, 2} indium (In)-based,³ and lead (Pb)-based⁴ catalysts have shown excellent activity for CO₂ reduction to formate. For example, Sn dendritic structures achieved faradaic efficiency (FE) greater than 70% for formate generation at -1.4 V vs. reversible hydrogen electrode (RHE).² In addition, oxide-derived Pb and dendritic In foam have reached FEs of 95% (-0.8 V vs. RHE) and 86% (-0.86 V vs. RHE), respectively. As shown in Figure 3.1, there are coordinating and non-coordinating models for CO₂ adsorption on the catalyst surface. In either case, the CO₂ adsorption process is generally regarded as the rate determining step because the bending of the linear CO₂ molecule on a catalyst surface consumes a significant amount of energy.⁵ For Sn-, In-, mercury (Hg)- and Pb-based catalysts, CO₂ usually first adsorbs to their surfaces in the form of a negatively charged molecule (CO₂⁻), which is followed by a protonation step. The weak adsorption strength between and these catalysts is favorable for the formation of HCOO⁻.^{6, 7} On the other hand, CO₂ adsorbs on silver (Ag)-based,⁸ gold (Au)-based,⁹ and zinc (Zn)-based¹⁰ catalysts through a coordinating path in which adsorbed formate (*COOH) is formed on the surface. These catalysts bind with *COOH strongly but weakly bind with adsorbed carbon monoxide (*CO)⁷ (Figure 3.1) and, therefore, are more prone to CO desorption. As a result, these catalysts show high selectivity towards CO. The FE of CO over nanoporous Ag,⁸ monodisperse Au,⁹ and Zn dendrites¹⁰ have reached 90% (-0.5 V vs. RHE), 90% (-0.67 V vs. RHE) and 79% (-1.1 V vs. RHE), respectively.

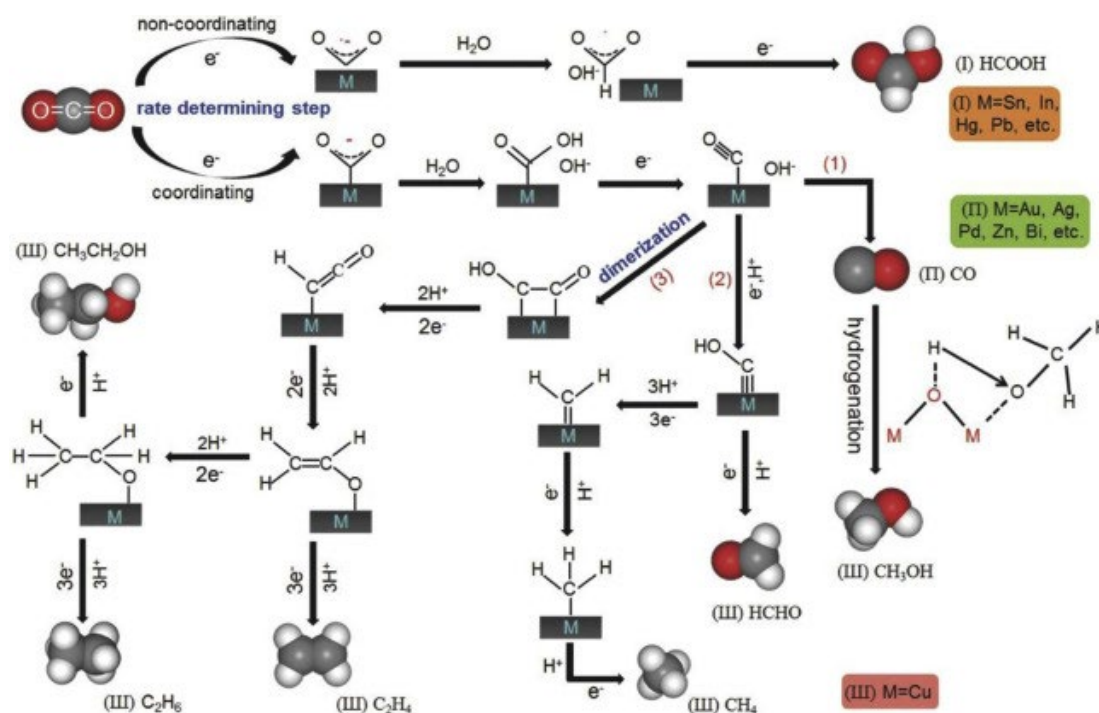


Figure 3.1 proposed reaction mechanism on different metal catalysts. Reproduced with permission from the study by *Zhang et al.*¹¹

C₂₊ products (e.g., ethylene [C₂H₄], ethanol [C₂H₅OH]) are of interest because they are more economically valuable owing to their high energy densities. Yet, the formation of C₂₊ products also involve more complicated reaction pathways and sluggish reaction kinetics (Table 3.1). Although many reaction mechanisms of C₂₊ generation are still under investigation, copper (Cu) is the catalyst that produces the widest range of C_n products.¹² Figure 3.1 also illustrates the proposed CO₂ electrochemical reduction mechanisms on Cu electrodes. It has been reported that *CO is the key intermediate in generating C₂₊ products through a CO–CO dimerization step. Unlike other catalysts, Cu is unique because it binds appropriately with *CO, which allows *CO to further react to generate C₂₊ products.

Table 3.1 Major products of CO₂ reduction with different reaction pathways and standard reaction potentials.¹³

Product	Reactions	Potential (V vs. RHE)
HCOOH	$\text{CO}_2 (\text{g}) + 2\text{H}^+ + 2\text{e}^- \rightarrow \text{HCOOH} (\text{l})$	-0.250
CO	$\text{CO}_2 (\text{g}) + 2\text{H}^+ + 2\text{e}^- \rightarrow \text{CO} (\text{g}) + \text{H}_2\text{O} (\text{l})$	-0.106
HCHO	$\text{CO}_2 (\text{g}) + 4\text{H}^+ + 4\text{e}^- \rightarrow \text{HCHO} (\text{l}) + \text{H}_2\text{O} (\text{l})$	-0.070
CH ₃ OH	$\text{CO}_2 (\text{g}) + 6\text{H}^+ + 6\text{e}^- \rightarrow \text{CH}_3\text{OH} (\text{l}) + \text{H}_2\text{O} (\text{l})$	0.016
CH ₄	$\text{CO}_2 (\text{g}) + 8\text{H}^+ + 8\text{e}^- \rightarrow \text{CH}_4 (\text{l}) + 2\text{H}_2\text{O} (\text{l})$	0.169
C ₂ H ₄	$\text{CO}_2 (\text{g}) + 12\text{H}^+ + 12\text{e}^- \rightarrow \text{C}_2\text{H}_4 (\text{l}) + 4\text{H}_2\text{O} (\text{l})$	0.064
C ₂ H ₅ OH	$\text{CO}_2 (\text{g}) + 12\text{H}^+ + 12\text{e}^- \rightarrow \text{C}_2\text{H}_5\text{OH} (\text{l}) + 3\text{H}_2\text{O} (\text{l})$	0.084
CH ₃ CH ₂ CH ₂ OH	$\text{CO}_2 (\text{g}) + 18\text{H}^+ + 18\text{e}^- \rightarrow \text{CH}_3\text{CH}_2\text{CH}_2\text{OH} (\text{l}) + 5\text{H}_2\text{O} (\text{l})$	0.210

RHE, reversible hydrogen electrode.

References

1. a) Y. Hori, H. Wakebe, T. Tsukamoto, O. Koga, *Electrochim. Acta* **1994**, *39*, 1833-1839; b) Y. Zhang, W. Zhang, Y. Feng, J. Ma, *J. Energy Chem.* **2020**, *48*, 1-6.
2. D. H. Won, C. H. Choi, J. Chung, M. W. Chung, E.-H. Kim, S. I. Woo, *ChemSusChem* **2015**, *8*, 3092-3098.
3. Z. Xia, M. Freeman, D. Zhang, B. Yang, L. Lei, Z. Li, Y. Hou, *ChemElectroChem* **2018**, *5*, 253-259.
4. C. H. Lee, M. W. Kanan, *ACS Catal.* **2015**, *5*, 465-469.
5. L. Sun, V. Reddu, A. C. Fisher, X. Wang, *Energy & Environmental Science* **2020**, *13*, 374; A. Álvarez, M. Borges, J. J. Corral-Pérez, J. G. Olcina, L. Hu,

- D. Cornu, R. Huang, D. Stoian, A. Urakawa, *ChemPhysChem* **2017**, *18*, 3135-3141.
6. B. Khezri, A. C. Fisher, M. Pumera, *J. Mater. Chem. A* **2017**, *5*, 8230-8246.
7. Y. Wang, J. Liu, Y. Wang, A. M. Al-Enizi, G. Zheng, *Small* **2017**, *13*, 1701809.
8. J. Rosen, G. S. Hutchings, Q. Lu, S. Rivera, Y. Zhou, D. G. Vlachos, F. Jiao, *ACS Catal.* **2015**, *5*, 4293-4299.
9. W. Zhu, R. Michalsky, Ö. Metin, H. Lv, S. Guo, C. J. Wright, X. Sun, A. A. Peterson, S. Sun, *J. Am. Chem. Soc.* **2013**, *135*, 16833-16836.
10. J. Rosen, G. S. Hutchings, Q. Lu, R. V. Forest, A. Moore, F. Jiao, *ACS Catal.* **2015**, *5*, 4586-4591.
11. W. Zhang, Y. Hu, L. Ma, G. Zhu, Y. Wang, X. Xue, R. Chen, S. Yang, Z. Jin, *Adv. Sci.* **2018**, *5*, 1700275.
12. a) A. Vasileff, X. Zhi, C. Xu, L. Ge, Y. Jiao, Y. Zheng, S.-Z. Qiao, *ACS Catal.* **2019**, *9*, 9411-9417; b) B. Zijlstra, X. Zhang, J.-X. Liu, I. A. W. Filot, Z. Zhou, S. Sun, E. J. M. Hensen, *Electrochim. Acta* **2020**, *335*, 135665; c) A. H. Shah, Y. Wang, S. Hussain, M. B. Akbar, A. R. Woldu, X. Zhang, T. He, *Phys. Chem. Chem. Phys.* **2020**, *22*, 2046-2053.
13. Z. Gu, H. Shen, L. Shang, X. Lv, L. Qian, G. Zheng, *Small Methods* **2018**, *2*, 1800121; K. P. Kuhl, E. R. Cave, D. N. Abram, T. F. Jaramillo, *Energy Environ. Sci.* **2012**, *5*, 7050-7059; Y. Zhang, Y. Zhao, C. Wang, Z. Wei, J. Yang, J. Ma, *Phys. Chem. Chem. Phys.* **2019**, *21*, 21341-21348.

Chapter 4

Cu₂O/CuS Nanocomposites Show Excellent Selectivity and Stability for Formate Generation via Electrochemical Reduction of Carbon Dioxide

Abstract

Formate is an important value-added chemical that can be produced via electrochemical CO₂ reduction reactions (CO₂RR). Cu₂O-based catalysts have previously demonstrated decent activity for formate generation; however, they often suffer from poor electrochemical stability under reductive conditions. Here, we report a new Cu₂O/CuS composite catalyst that simultaneously achieves an excellent faradaic efficiency of 67.6% and a large partial current density of 15.3 mA/cm² at -0.9 V vs RHE for formate. Importantly, it maintains an average faradaic efficiency of 62.9% for at least 30 h at the same potential. The catalytic selectivity and stability for formate production outperform other Cu, CuS, and Cu₂O catalysts.

4.1 Introduction

Electrochemical CO₂ reduction reactions (CO₂RR) represent a promising route to help alleviate global warming through reducing the footprint of the carbon cycle. Value-added chemicals, such as formate,¹ can be generated as products of CO₂RR, which has recently attracted growing attention.^{2,3} Sn-based catalysts have been shown to be selective towards formate in CO₂RR since the 1980s.⁴ A recent report showed that Sn dendrites can achieve a faradic efficiency (FE) of formate higher than 70 % and a partial current density (j_{HCOO^-}) of 17 mA/cm².⁵ However, the relatively low global reserve of Sn and its uneven distribution on the earth result in high price of Sn

(~\$20/kg).⁶ In contrast, Cu is an earth abundant element that has a considerably lower price (~\$6/kg)⁷ than Sn. Recent studies revealed that metallic Cu catalysts also have decent catalytic activities for formate generation via CO₂RR. For instance, Loiudice *et al.* reported Cu nanocubes exhibit a FE of 15 % (at -1.1 V vs. RHE) and j_{HCOO^-} around 1 mA/cm² for formate.⁸ Nonetheless, for metallic Cu, both the FE and partial current density of formate are not comparable with Sn-based catalysts. An alternative approach was to use Cu-based heterostructures for formate production. For example, Wang *et al.* reported a Cu-Au bimetallic catalyst that achieved an outstanding FE of 81 % and j_{HCOO^-} of 10.4 mA/cm² for formate at -0.6 V vs. RHE. Its performance is much better than the Cu metal catalyst alone.⁹ Yet, increasing the material cost is a downside for adding Au as catalyst.

Theoretical studies have shown that formate can be preferably generated over copper (I) oxide Cu₂O (111) due to the low energy barrier of forming the critical bidentate *OCHO intermediate.^{10, 11} Therefore, using Cu₂O as a catalyst for CO₂RR to produce formate has been of interest.^{11-13, 14} For example, Zhu *et al.* reported a FE of formate of 66 % (-0.8 V vs. RHE) over Cu₂O nanoparticles, which is significantly higher than its Cu counterparts.¹² Yet, the FE of formate over Cu₂O tends to decay quickly.¹¹ Li *et al.* showed that Cu₂O can be rapidly reduced to form metallic Cu under CO₂RR conditions (-0.5 V vs. RHE in 0.100 M KHCO₃).¹⁵ Retaining the catalytic properties of Cu₂O in CO₂RR is critical yet challenging.

Recently, Chen *et al.* reported a cubic nanosized copper (II) sulfide/copper (I) oxide/copper (CuS/Cu₂O/Cu) photocathode for the oxygen reduction reaction.¹⁶ They

found that the conduction band alignment of CuS and Cu₂O facilitates the photo-excited electron transfer from Cu₂O to CuS and, thus, reduces the electron/hole pair recombination loss and enhances the stability of Cu₂O. Inspired by this work, we hypothesized that the aligned band structure at the CuS/Cu₂O heterojunction (Figure 4.1) would suppress the reduction of Cu₂O during CO₂RR. Here, we report the synthesis of a nanocomposite of copper (I) oxide (Cu₂O) and copper (II) sulfide (CuS) through a multistep conversion of copper (I) sulfide (Cu₂S). Structural characterization identified clear domains of CuS and Cu₂O heterointerfaces. The nanocomposite (denoted as Cu₂O/CuS) shows a low onset potential of -0.5 V vs. RHE and exhibits excellent FE of formate of 67.6 % and j_{HCOO^-} of 15.3 mA/cm² at -0.9 V vs. RHE. More importantly, it retained an average FE of 62.9 % for at least 30 hours at the same applied potential. We believe that the presence of CuS stabilizes Cu₂O for CO₂RR due to the favorable band alignment. Density Functional Theory (DFT) calculations also suggest that the CuS (110) surface has preferential selectivity toward formate over CO formation.

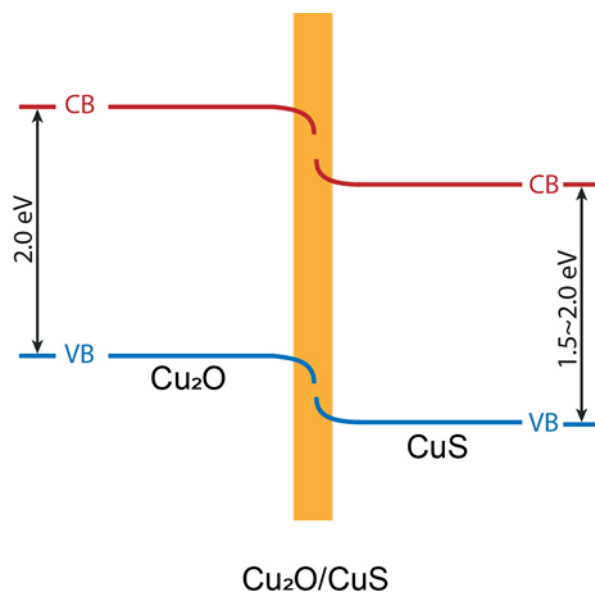


Figure 4.1 A schematic of the band alignment of Cu₂O /CuS heterojunctions based on previous reports,¹⁶⁻¹⁸ assuming a band gap within the reported range of 1.5-2.0 eV.^{16, 19}

The synthesis of our Cu₂O/CuS nanocomposite is illustrated in Figure 4.2a. Metallic Cu gauze was used as a growth substrate and we note that this porous current collector can facilitate the diffusion and mass transport of both reactants and products during CO₂RR. Cu₂S was hydrothermally grown on the Cu gauze using a previously reported method²⁰, followed by a two-step electrochemical and thermal treatment (Experimental section). XRD analysis showed that the product is mainly Cu₂O (JCPDS 05-0667). According to the Pourbaix diagram, Cu₂S would be converted to metallic Cu at the potential we used in the electrochemical treatment. Meanwhile, oxygen gas was generated on the anode. We believe that the reaction between Cu, oxygen, and water leads to the generation of Cu(OH)₂²¹, which consequently been reduced to Cu₂O during the thermal reduction process.²² Figure 4.2 shows the structural characterization data

collected from the Cu₂O/CuS samples tested for CO₂RR at -0.9 V vs. RHE for 6 hours. As shown in Figure 4.2b and c, the surface of Cu gauze is uniformly covered with nanoparticles. The XRD pattern reveals the particles on the Cu gauze are still Cu₂O after CO₂RR. High-resolution transmission electron microscopy (HR-TEM) analysis performed on several randomly selected particles further showed that the nanoparticles are actually a mixture of Cu₂O and CuS. The HR-TEM image (Figure 4.2d) shows three different lattice spacings that are consistent with the d-spacings reported for the (111) and (200) planes of Cu₂O and (110) planes of CuS. The fast Fourier transform (FFT) pattern collected from the high-resolution image also suggested that Cu₂O/CuS is a polycrystalline mixture of Cu₂O and CuS (Figure 4.2e). The high-angle annular dark field-TEM (HAADF-TEM, Figure 4.2f-i) image and corresponding elemental mapping images reveal a uniform spatial distribution of Cu, S and O over the Cu gauze, as expected for a composite of Cu₂O and CuS nanoparticles.

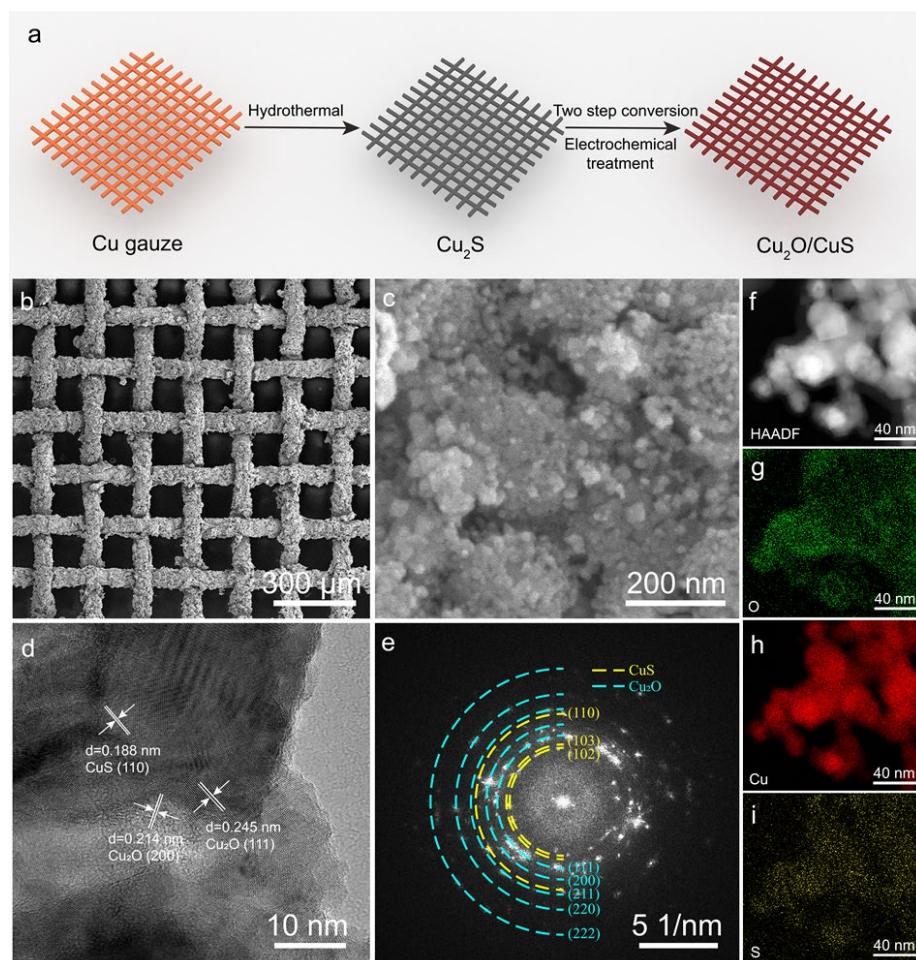


Figure 4.2 (a) A schematic illustration of the synthesis of $\text{Cu}_2\text{O}/\text{CuS}$ nanocomposites. (b) and (c) SEM images of $\text{Cu}_2\text{O}/\text{CuS}$ nanocomposites grown on a copper gauze collected at different magnifications. (d) HR-TEM image collected from a representative $\text{Cu}_2\text{O}/\text{CuS}$ particle. (e) Corresponding FFT image of (d). Blue and yellow dashed lines highlight the diffraction rings of polycrystalline Cu_2O and CuS particles, respectively. (f-i) HAADF-TEM image of $\text{Cu}_2\text{O}/\text{CuS}$ nanocomposites and the corresponding mapping images of element O, Cu, and S.

4.2 Experimental section

Synthesis: Synthesis of Cu_2S : 0.032 g sulfur powder (sublimed sulfur) and 0.364 g cetyltrimethylammonium bromide (CTAB) were dissolved in 25 ml deionized water under vigorous stirring. Then 1 ml hydrazine monohydrate was added into the solution. Cu gauze (2 cm \times 2 cm, 140 mesh with 0.056 mm diameter wire) was cleaned in 85 % H_3PO_4 for 1 min, followed by successive sonication steps in deionized water, acetone and ethanol. Cu gauze and the S containing solution were transferred to a Teflon-lined stainless autoclave and heated at 180 °C for 12 hours. The autoclave was then cooled to room temperature. The Cu gauze was uniformly coated with Cu_2S and became grey in color. The prepared Cu_2S catalyst was rinsed with deionized water and dried in vacuum overnight.

Post-growth treatment: The Cu_2S was electrochemically treated in a 1.00 M KNO_3 solution for 6 hours at a constant potential (-1.5 V vs. Ag/AgCl reference electrode). The sample was then air dried and further annealed in a tube furnace at 500 °C for 4 hours in hydrogen atmosphere at a flow rate of 120 sccm.

Characterization: The crystal phase and morphologies of the spent catalysts ($\text{Cu}_2\text{O}/\text{CuS}$ nanocomposites on Cu gauze) were characterized by X-ray powder diffraction (XRD, Rigaku Smartlab Powder & Thin Film Diffractometer) and scanning electron microscopy (SEM, Hitachi S-4800 II), respectively. After testing for CO_2RR for 6 hours, $\text{Cu}_2\text{O}/\text{CuS}$ particles were collected by sonicating the $\text{Cu}_2\text{O}/\text{CuS}$ coated Cu gauze in ethanol. These particles were used for high-resolution transmission electron microscopy (HR-TEM, Talos-F200X), and X-ray photoelectron spectroscopy (XPS,

Thermo Scientific ESCALAB 250Xi). The contact angle was measured with a Ossila Contact Angle Goniometer. Gas chromatography (SRI Model 8610C) was used to identify and quantify the yield of gas products. 600 MHz nuclear magnetic resonance spectroscopy (NMR, 600 MHz, Varian INOVA) was used to identify and quantify the yield of products in liquid electrolyte.

Electrochemical test and product analysis: The electrochemical measurements were conducted in a three-electrode configuration in a H-cell²³ connected to an electrochemical workstation (CHI 660D). We used the copper gauze decorated with Cu₂O/CuS nanocomposites as the working electrode (1 cm²), a carbon rod as the counter electrode, and Ag/AgCl (saturated KCl) as the reference electrode. The cathode and anode chambers were separated by a proton exchange membrane (Nafion 117). Each chamber was filled with 30 ml of 0.100 M KHCO₃ solution. CO₂ (99.995%) was purged at a flow rate of 40 sccm into the cathode chamber for 30 min before each CO₂RR measurement with continued purging throughout the measurement. The solution pH after purging with CO₂ was 6.7. The catalytic activity of Cu₂O/CuS catalysts was measured in a range of potentials from -0.4 V to -1.3 V vs. RHE. At each potential, the catalyst was tested for 9 hours in total. After the first 6 hours of measurement, the electrochemical cell, Nafion membrane, and electrodes were cleaned. Then the subsequent 3 hours of measurement was performed in a fresh electrolyte for gas and liquid product analysis. The gas products from CO₂ reduction were analyzed by gas chromatography. Argon (Praxair, 5.0 ultra-high purity) was used

as the carrier gas. All Faradaic efficiencies reported were averaged from three different runs. The FEs for gas products were calculated using the following equation:

$$FE = \frac{ne^- \times 40 \left(\frac{\text{ml}}{\text{min}}\right) \times 10^{-6} \left(\frac{\text{m}^3}{\text{ml}}\right) \times v(\text{vol}\%) \times 1.01 \times 10^5 \left(\frac{\text{N}}{\text{m}^2}\right) \times 9.65 \times 10^4 \left(\frac{\text{C}}{\text{mol}}\right)}{8.314 \left(\frac{\text{N}\cdot\text{m}}{\text{mol}\cdot\text{K}}\right) \times 298.15 \text{ (K)} \times I \text{ (A)} \times 60 \left(\frac{\text{s}}{\text{min}}\right)}$$

Where n is the number of electrons involved in the CO_2 reduction process, $40 \left(\frac{\text{ml}}{\text{min}}\right)$ is the flow rate of the CO_2 gas, $1.01 \times 10^5 \left(\frac{\text{N}}{\text{m}^2}\right)$ is the atmospheric pressure, $9.65 \times 10^4 \left(\frac{\text{C}}{\text{mol}}\right)$ is the Faraday constant, $v(\text{vol}\%)$ is percent of gas products (derived from GC), $8.314 \left(\frac{\text{N}\cdot\text{m}}{\text{mol}\cdot\text{K}}\right)$ is the gas constant, 298.15 (K) is room temperature, I is the current.

Both anolyte and catholyte were collected for proton NMR analysis to identify and quantify the yield of the liquid product. For NMR measurements, 0.5 ml of electrolyte solution was mixed with 0.1 ml deuterium oxide (D_2O , 99.9%) and dimethyl sulfoxide (DMSO, 56.3 mM) was added as an internal standard. The FE for forming formate was calculated using the following equation:

$$FE = \frac{2e^- \times 56.3 \text{ (mM)} \times \left(\frac{S_{\text{formate}}}{S_{\text{DMSO}}}\right) \times 6 \times 30 \text{ ml} \times 9.65 \times 10^4 \left(\frac{\text{C}}{\text{mol}}\right)}{\text{Total charge}}$$

where $2e^-$ is used because the formation of formate from CO_2 reduction is a two-electron reaction, 56.3 mM is the concentration of DMSO internal standard, S_{formate} and S_{DMSO} are the respective peak areas of formate and DMSO in the NMR spectrum, a constant of 6 is added because DMSO has 6 protons while formate has 1 proton, 30 ml is the total volume of electrolyte solution in each chamber, and $9.65 \times 10^4 \text{ C per mole}$ is the Faraday constant. The total charge was obtained from chronoamperometry data.

Computational Methods: All calculations were performed using the Vienna Ab initio Simulation Package (VASP) code with the projector-augmented wave (PAW) approach and the Revised Perdew-Burke-Ernzerhof (RPBE) exchange-correlation functional.²⁴ For the slab models we used the optimized bulk lattice constants 5.02 Å for covellite as calculated with the RPBE functional. Solvation corrections were treated using an implicit solvation model within a linearized Poisson-Boltzmann approach as implemented in VASPsol,²⁵ using a Debye length of 3 Å.

Model surfaces for CuS (110) were constructed using the Python Materials Genomics (pymatgen) package.²⁶ For the covellite CuS (110) surfaces, we adopted a 48-atom clean slab model that was sampled with a $2 \times 4 \times 1$ Monkhorst-Pack k -point grid. All slab calculations were performed with 15 Å of vacuum region and a 500-eV plane-wave energy cutoff. Free energies were evaluated with the calculated electronic energies assuming adsorbate and gas phase entropic corrections for all species.^{27, 28} We also adopt electronic energy contributions as detailed in the same references and elsewhere,²⁹ which equates to a systematic correction of 0.46 eV to CO₂, 0.07 eV for CO, and 0.27 eV for HCOOH gas-phase molecules. Electrochemical reaction energies and limiting overpotentials were evaluated with the computational hydrogen electrode (CHE) model of Nørskov and coworkers, where we consider electrochemical reaction steps as coupled proton-electron transfer events.³⁰

4.3 Results and Discussion

We performed XPS analysis to probe the chemical environment of the Cu₂O/CuS surface (Figure 4.3). In the Cu 2p XPS spectrum, the peaks centered at 934.3

and 954.3 eV as well as the shake-up peaks between 940 to 950 eV indicate the presence of Cu^{2+} .^{31, 32} We also collected the Cu LMM Auger spectrum (Figure 4.3b) to probe the Cu valence states since both Cu^+ and Cu^0 have signals located at binding energies of 932.4 eV and 952.2 eV. The characteristic peaks observed at 570.2, 569.0, and 568.3 eV in the Cu LMM Auger spectrum confirmed the presence of Cu^0 , Cu^{2+} and Cu^+ , respectively.³²⁻³⁴ The existence of Cu^0 could be due to the partial reduction of Cu_2O during CO_2RR . The presence of Cu_2O was also confirmed by O 1s XPS spectrum (Figure 4.3c) in which the peak located at 530.6 eV is consistent with the value reported for O-Cu in Cu_2O .^{35, 36} Furthermore, the nanocomposite exhibits a broad signal in the S 2p XPS spectrum between the binding energy of 163.7 to 161.1 eV, as shown in Figure 4.3d. By deconvoluting the broad peak, the characteristic peaks for CuS including the S vacancy (V_{S} , 161.1 eV), S^{2-} (161.7, 162.9 eV), and S_2^{2-} (162.4, 163.7 eV) were identified.^{33, 35, 37, 38} The S-O bond signals observed at 164.3 and 165.5 eV also indicate the formation of the $\text{Cu}_2\text{O}/\text{CuS}$ heterojunction.³⁸

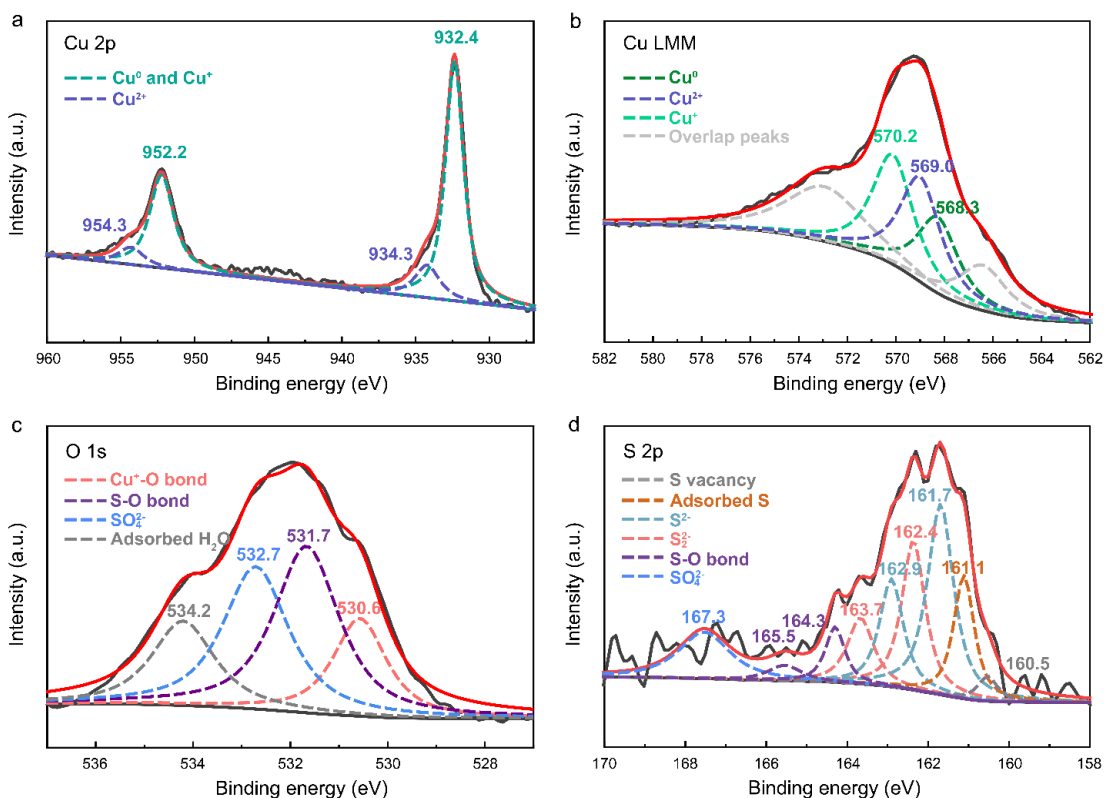


Figure 4.3 (a) Cu 2p XPS spectrum. (b) Cu Auger LMM spectrum. (c) O 1s and (d) S 2p XPS spectra. All spectra were collected from Cu₂O/CuS particles without Cu gauze substrate. The black curves represent experimental data and red curves represent the fitting curve. The dashed lines represent deconvoluted peaks.

The catalytic performance of Cu₂O/CuS was characterized in a H-cell in Ar and CO₂ saturated 0.100 M KHCO₃ electrolyte solutions using the linear scan voltammetry (LSV) technique. The cathodic current in CO₂ saturated electrolyte is smaller than that in Ar saturated electrolyte. The smaller current is possibly due to the suppression of HER in CO₂ saturated electrolyte.³⁹ We also performed chronoamperometry measurements to evaluate the catalyst performance. Proton NMR was used for analyzing the yield of formate. As shown in Figure 4.4a, Cu₂O/CuS exhibits decent FE

for formate (~20 %) at a low potential -0.5 V vs. RHE. In contrast, the activity of Cu gauze is low (~2 %) at the same potential. The optimized potential for formate generation over the Cu₂O/CuS nanocomposite is -0.9 V vs. RHE (Figure 4.4). At this potential, the FE for formate reaches 67.6% at a current density of 15.3 mA/cm², with only a small amount of ethanol (1.4%) and propanol (0.9%) (Figure 4.5a and b). The yield and the current density for formate generation are considerably higher than that of the Cu gauze control sample (39.2 %) as well as previously reported Cu, CuS and Cu₂O catalysts (Figure 4.5a and Table 4.1). We also investigated the composition of gaseous products at this optimized potential of -0.9 V vs. RHE and found that only hydrogen gas (FE of 18.9%) is present (Figure 4.5b). In comparison, a higher FE of 38.9% for hydrogen gas was obtained over Cu gauze, indicating that the Cu₂O/CuS composite largely suppressed hydrogen production. The insets in Figure 4.5b show the contact angles of the electrolyte (0.100 M KHCO₃) droplet on the Cu gauze and Cu₂O/CuS catalyst surface, respectively. The comparison indicates that the Cu₂O/CuS catalyst is more hydrophilic than the Cu gauze. The improved hydrophilicity of Cu₂O/CuS enhances the accessibility of the catalyst's active sites in CO₂ saturated electrolyte and therefore increases the CO₂ reduction efficiency. The boosted CO₂ reduction rate creates a higher local pH and consequently suppresses HER, which ensures better accessibility of electrolyte to the active sites. Furthermore, it is noteworthy that the Cu₂O/CuS catalyst was able to retain its catalytic performance for at least 30 hours at -0.9 V vs. RHE with an average of FE of 62.9 % and j_{HCOO^-} of 12.3

mA/cm² for formate (Figure 4.5c). This performance is much better than the electrochemical stability reported for other Cu₂O catalysts (Table 4.1).

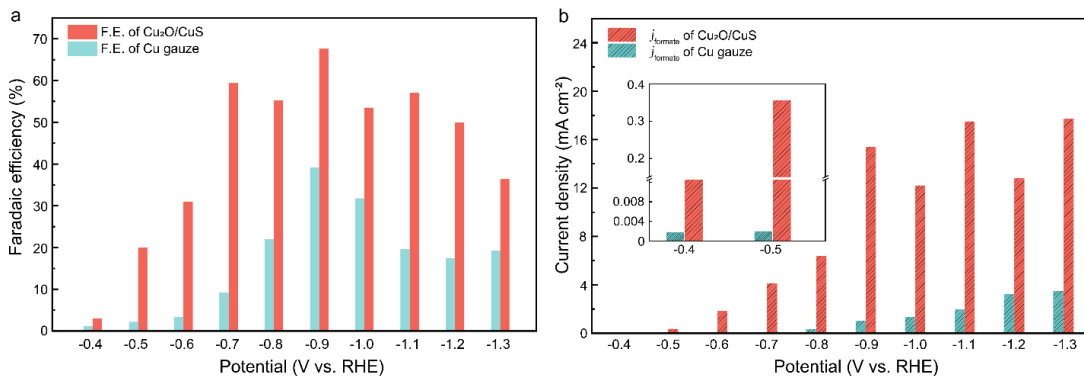


Figure 4.4 (a) Faradaic efficiency and (b) partial current for formate generation obtained from Cu₂O/CuS and Cu gauze at different applied potentials. The inset figure in (b) shows a magnified view of partial currents obtained at -0.4 V and -0.5 V vs. RHE.

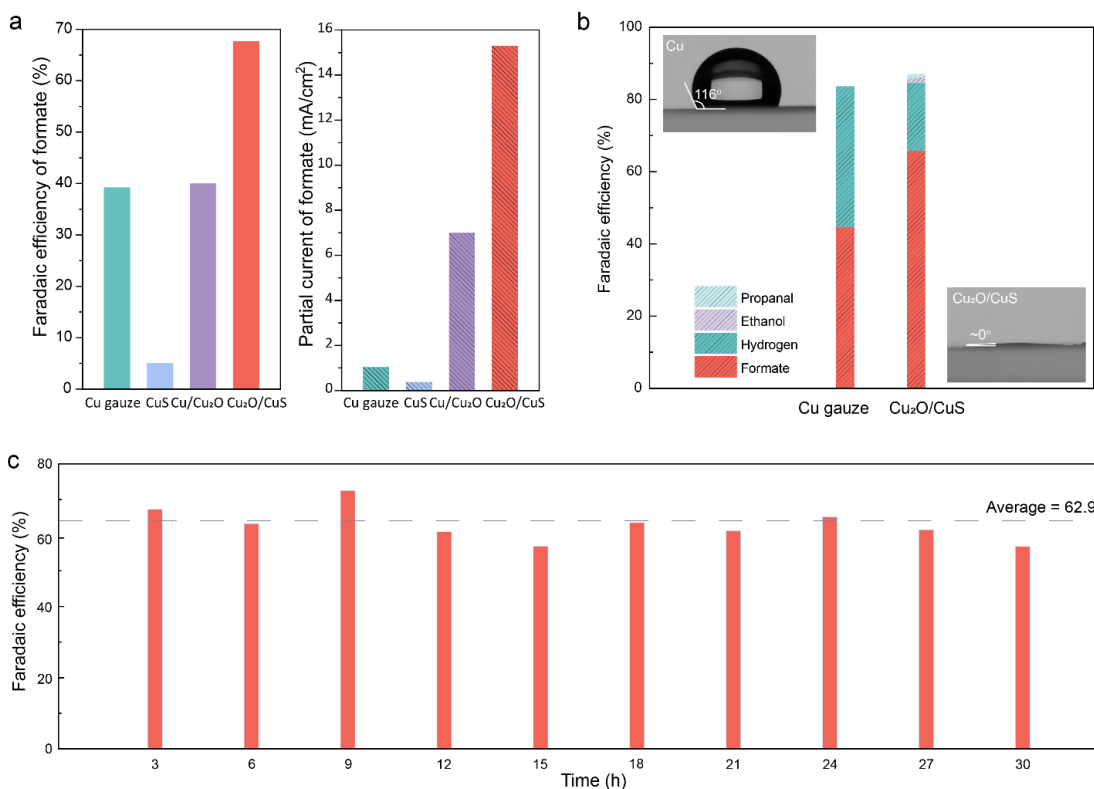


Figure 4.5 (a) Faradaic efficiency and partial current density (towards formate) comparison of the Cu gauze, CuS, Cu₂O and Cu₂O/CuS (CuS and Cu₂O data was extracted from previous reports^{14, 40}). (b) Faradic efficiency obtained from Cu₂O/CuS and Cu gauze at -0.9 V vs. RHE. The inset figures in (b) shows the contact angle of the 0.100 M KHCO₃ droplet on the Cu gauze (top left) and Cu₂O/CuS catalyst (bottom right). (c) A plot of FE for formate collected from the Cu₂O/CuS catalyst at -0.9 V vs. RHE for 30 hours.

Table 4.1 Comparison of the catalytic performance of CuS/Cu₂O for formate formation with other state-of-the-art Cu-based catalysts.

Catalysts	Potential (vs. RHE)	FE of formate	j_{HCOO^-} (mA/cm ²)	Test time	Ref.
Cu ₂ O/CuS	-0.9 V	67.6 %	15.3	30 h	this work
Metallic Cu	-0.88 V	22 %	0.2	1.5 h	41
Oxide derived Cu	-0.8 V	25 %	1.0	40 mins	41
Amorphous Cu	-0.8 V	36 %	4.3	12 h	42
Copper nanofoam	-0.9 V	37 %	1.5	1 h	43
CuS nanosheet arrays	-1.1 V	5 %	0.37	60 h	40
Plasma-activated Cu (Cu/Cu ₂ O)	-0.55 V	25 %	0.25	1 h	44
ERD-Cu (Cu/Cu ₂ O)	-1.0 V	28 %	*5.6	1 h	45

Cu and Cu ₂ O					
nanocubes (10 cycles)	-0.845 V	40 %	7	-	14
Cu ₂ O nanoparticles	-0.8 V	66 %	-	-	12
*Estimated from original paper.					

Although CuS alone is not very active for formate generation (highest FE < 10 %, $j_{\text{HCOO}^-} < 1 \text{ mA/cm}^2$),⁴⁰ we believe CuS can work synergistically with Cu₂O to improve activity and stability for producing formate during CO₂RR. The conventional mechanism for formate selectivity is dictated by the relative energetics of the two-electron reduction CO₂RR pathways to forming CO+H₂O or formic acid (HCOOH).^{2, 28} The CO production pathway is believed to proceed via carboxyl (COOH*) intermediates, while the formate/HCOOH pathway is believed to proceed via formyl (OCHO*) intermediates or carboxyl (COOH*) intermediates (especially for catalysts that have low binding affinity with *OCHO), with their relative binding energies correlated to experimentally observed selectivity trends in a number of electrochemical systems.^{2, 28, 46} In Figure 4.6, we show the relative CO₂RR energetics calculated for OCHO* vs COOH* intermediates on CuS (110) surfaces. The DFT results demonstrated that OCHO* preferentially binds bidentate with O bound to surface Cu sites, while COOH* preferentially binds through C to surface anion species.⁴⁷ Despite also binding through C like COOH*, CO* is found to preferentially bind to Cu sites rather than anion sites. However, we find the binding free energies of

CO* as calculated with the RPBE functional are unfavorable relative to CO(g), suggesting that CO* should dissociate from CuS (110) surfaces upon formation (Figure 4.7). HCOOH* was also found to be unstable relative to the gas phase and spontaneously dissociated in the calculations. Hydrogen, as described more below, is found to strongly favor anion sites and may inhibit the COOH*-mediated pathway due to competitive adsorption.

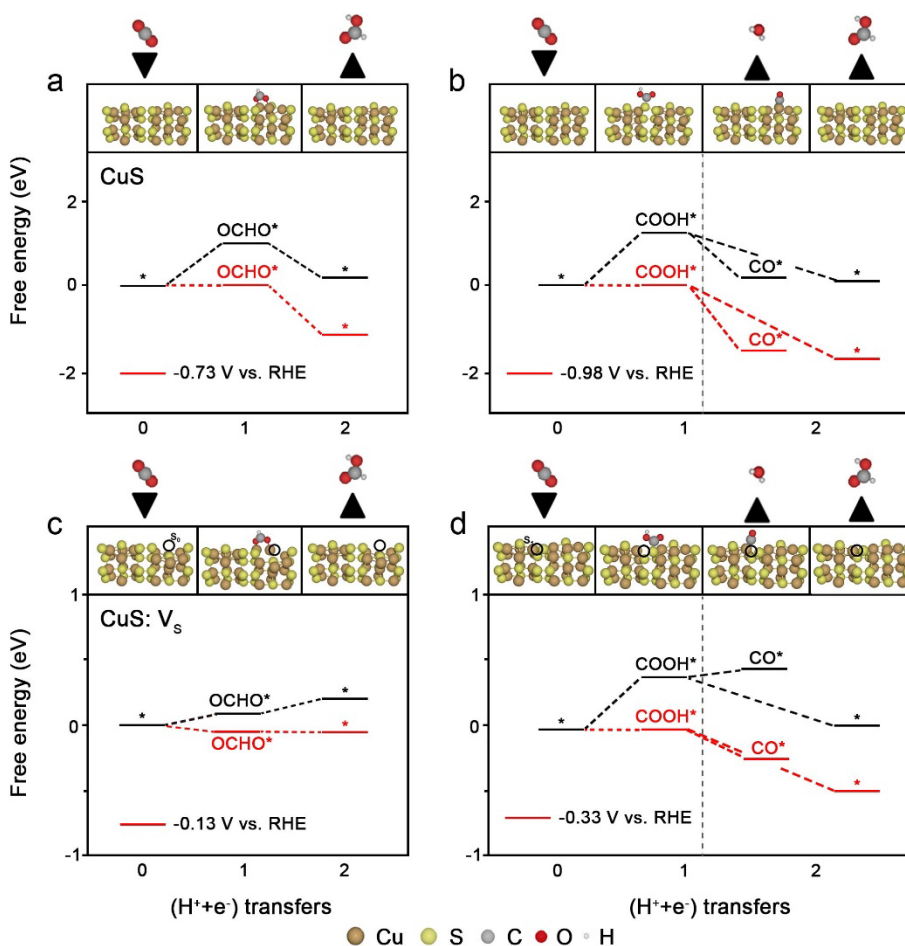


Figure 4.6 Comparison of calculated CO₂RR pathways to produce formic acid from (a) OCHO* and (b) COOH* intermediates on CuS (110) without surface O_S or vacancy species. Analogous pathways with surface sulfur vacancies V_S species are shown in (c)

and (d). Vacancies at S0 sites (V_{S0}) leave undercoordinated Cu that strengthen OCHO binding (c), while vacancies at S dimers (V_{S1}) leave undercoordinated S that more strongly bind COOH* (d). The black curves are pathways at 0 V vs. RHE and the red curves are at the predicted limiting potential (the applied overpotential) that makes the entire pathway downhill in free energy, as computed within the CHE model.

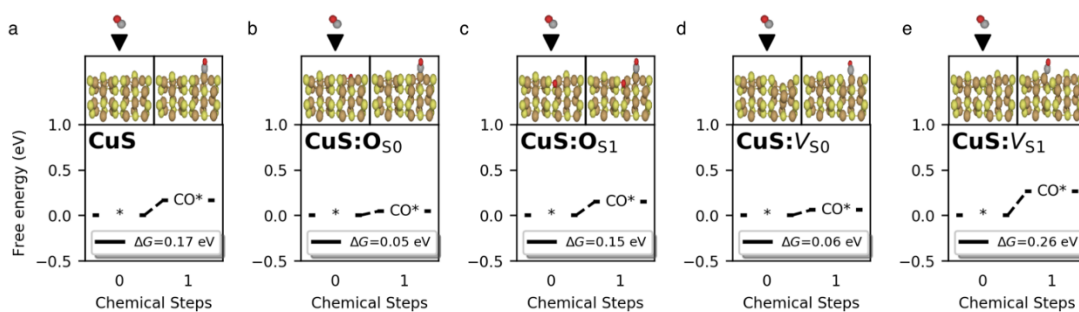


Figure 4.7 Calculated binding free energies of CO* relative to gas-phase CO(g). The CO molecular reference adopts an electronic energy correction of +0.07 eV and a chemical potential contribution at 298 K and 5562 Pa. The plots show binding on (a) pure CuS (110), (b) surfaces with substitutional O_S on the non-S dimer sites (O_{S0}), (c) surfaces with O_S on S dimer sites (O_{S1}), (d) surfaces with vacancies at the S0 site, and (e) surfaces with vacancies at the S1 site. CO* adsorbs to Cu sites and exhibits weak and unfavorable binding free energies, where it is expected to dissociate.

The calculations suggest that on the pure sulfide surface (Figure 4.6a, b), the potential-limiting step for CO₂RR is the initial binding and coupled-proton-electron transfer step, where OCHO* is slightly thermodynamically preferred to COOH*. Within the computational hydrogen electrode (CHE) model, the predicted theoretical onset potential to produce formate on CuS (110) is -0.73 V vs RHE, with a larger

potential of -0.98 V vs RHE predicted to activate the COOH^* pathway with both predictions being higher than what is observed experimentally. However, we note that the Faradaic efficiency towards formate, summarized in Figure 4.4, increases substantially in the vicinity of -0.7 vs RHE, which may coincide with the activation of the OCHO^* -mediated CO_2RR pathway to formic acid on CuS (110).

The incorporation of surface O_S species, as expected for the $\text{Cu}_2\text{O}/\text{CuS}$ nanocomposites, can preferentially stabilize both OCHO^* and COOH^* intermediates, with COOH^* binding enhanced more due to a stronger interaction with O surface sites relative to S sites (Figure 4.8-4.9). We considered O_S occupying both unique S sites in CuS, substituting on both the non-dimer and dimer S surface sites, which we denote as S_0 and S_1 , respectively. With O_S present, the COOH^* -mediated pathway can become more favorable than the OCHO^* -mediated pathway, with the most favorable case arising from COOH^* adsorbing to an $\text{O}_{\text{S}0}$ site. The calculated theoretical overpotential associated with this COOH^* adsorption step is only -0.11 V vs RHE, indicating that CO produced via a COOH^* -mediated pathway on surface O_S sites may be dominant at lower overpotentials. This may be consistent with the low FE for formate at the lowest overpotentials in Figure 4.4, but requires additional study of the gas-phase products to identify whether CO is being produced.

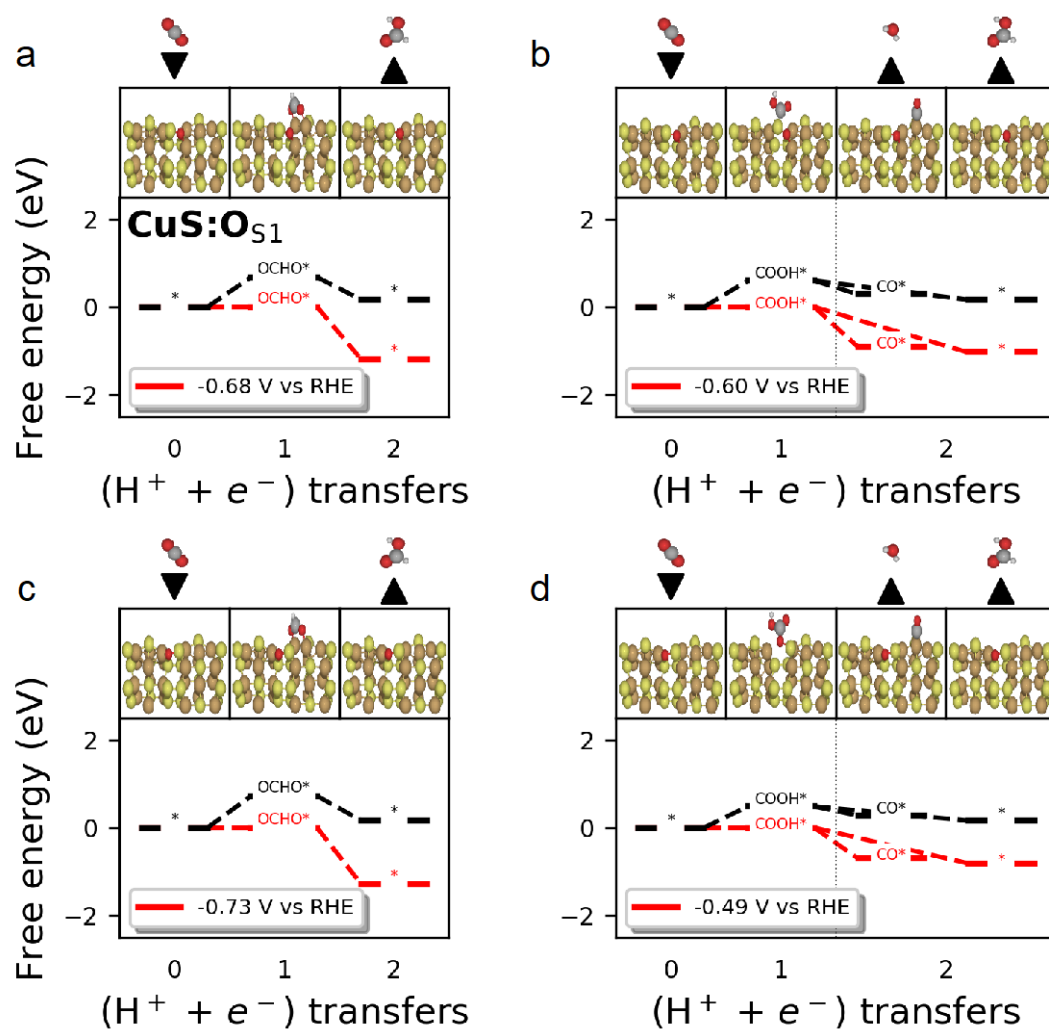


Figure 4.8 Comparison of calculated CO₂RR pathways to produce formic acid from (a,c) OCHO* and (b,d) COOH* intermediates on CuS (110) with substitutional O at a surface dimer site (O_{S1}). The top and bottom panels differ in the proximity of the O_{S1} to the bound intermediate, e.g. acting as a participant in the binding or as a neighboring atom. The black curves are pathways calculated at 0 V vs RHE and the red curves are at the potential that makes the entire included pathway downhill in free energy, as computed within the CHE model. O_{S1} are found to slightly stabilize the OCHO*-

mediated formic acid pathway (a,c), but make it much easier to bind COOH* intermediates at both the S1 (b) and OS₁ sites (d) relative to pure CuS(110).

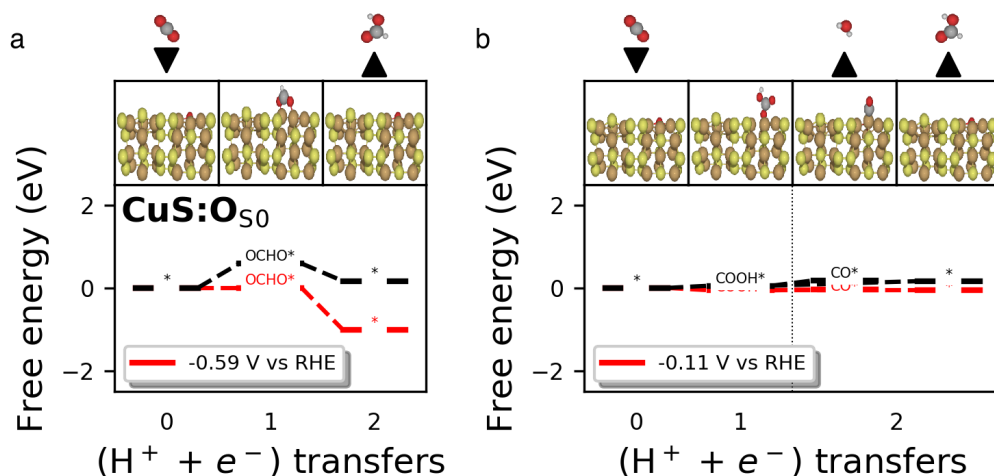


Figure 4.9 Comparison of calculated CO₂RR pathways to produce formic acid from (a) OCHO* and (b) COOH* intermediates on CuS (110) with substitutional O at a the S0 non-dimer surface S site (O_{S0}). The black curves are pathways calculated at 0 V vs RHE and the red curves are at the potential that makes the entire included pathway downhill in free energy, as computed within the CHE model. O_{S0} are found to stabilize the OCHO*-mediated formic acid pathway (a), but make it much easier to bind COOH* intermediates at the S0 site.

The hydrogen evolution is also a competitive reduction process that also preferentially involves anion sites rather than at Cu sites (Figure 4.10). We find that the interaction of H* with O_S to be problematically favorable, as the reduction of the surface O_{S0} and O_{S1} sites and the formation of H₂O and surface vacancies is predicted to occur already at 0 V vs RHE (Figure 4.11). Thus, surface O_S species are expected to

be short-lived under CO₂RR conditions, with the formation of surface sulfur vacancies (V_S) likely and consistent with the XPS spectra in Figure 4.3.

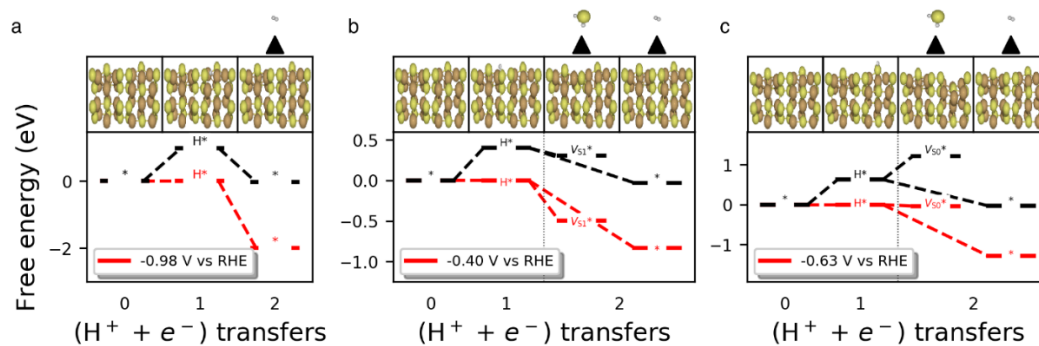


Figure 4.10 Comparison of calculated hydrogen evolution reaction (HER) pathways to adsorb H and produce H₂ on (a) a Cu site, (b) a non-dimer S site (S₀), and (c) a S dimer site (S₁) on CuS (110) surfaces. The black curves are pathways calculated at 0 V vs RHE and the red curves are at the potential that makes the entire included pathway downhill in free energy, as computed within the CHE model. In (b) and (c) we also show competitive hydrogen sulfide evolution from surface S sites, showing that HER is preferred over surface degradation on CuS(110). H* preferentially binds to anion sites, which may compete with COOH* intermediates but not OCHO*, which most favorably binds through metal sites.

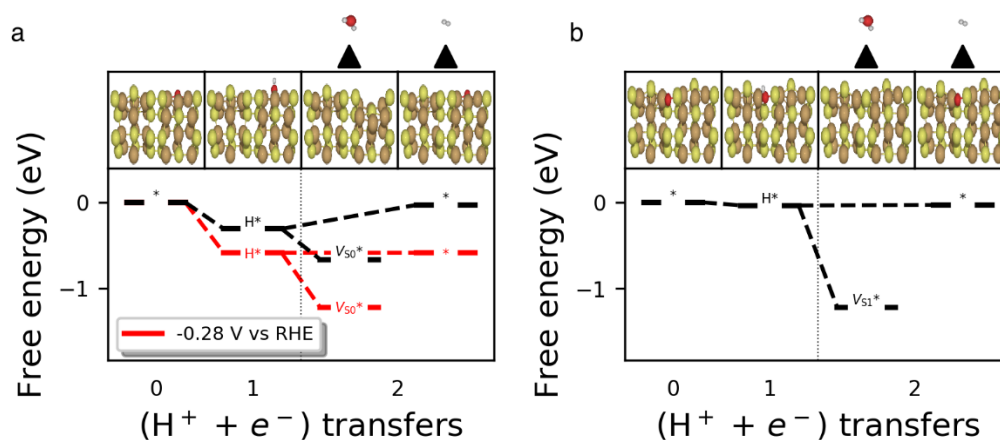


Figure 4.11 Comparison of calculated hydrogen evolution reaction (HER) pathways to adsorb H and produce H₂ on substitutional O_S occupying (a) a non-dimer S0 site and (b) a S1 dimer site on CuS (110) surfaces. We also show the competitive process for dissociation of the surface O_S as H₂O rather than facilitating HER, which we find is favorable for both the S0 and S1 sites at 0 V vs RHE. Thus, surface O_S sites are not expected to be long-lived under reducing conditions.

The influence of V_S on the OCHO*- and COOH*-mediated pathways is also considered in Figure 4.6c-d and Figures 4.12-4.13, where we find they have a significant effect. We find that the formation of undercoordinated Cu from V_{S0} lead to a much stronger binding of OCHO* intermediates, lowering the predicted onset potential to -0.13 V vs RHE for formate production. For surface vacancies at the dimer sites, we found V_{S1} lead to a stabilization of COOH* at the undercoordinated S site and lowers the predicted overpotential to adsorb CO₂ on the surface via a COOH*-mediated pathway to -0.33 V vs RHE. We note that these COOH* intermediates tethered to undercoordinated surface S species exhibit exposed C atoms that may also participate

in coupled-proton electron transfers in competition with the O and OH, providing another possible route to HCOOH formation instead of CO+H₂O.

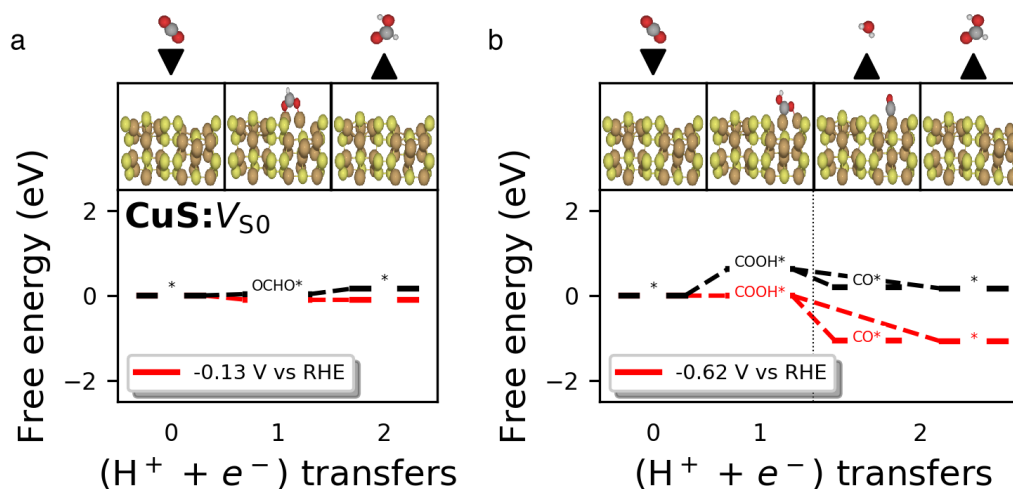


Figure 4.12 Comparison of calculated CO₂RR pathways to produce formic acid from (a) OCHO* and (b) COOH* intermediates on CuS (110) with a surface S vacancy (V_{S0}) at a the S0 S site. The black curves are pathways calculated at 0 V vs RHE and the red curves are at the potential that makes the entire included pathway downhill in free energy, as computed within the computational hydrogen electrode (CHE) model. V_{S0} are found to significantly enhance the OCHO*-mediated formic acid pathway, as the undercoordinated Cu can more strongly bind OCHO* relative to pure CuS(110).

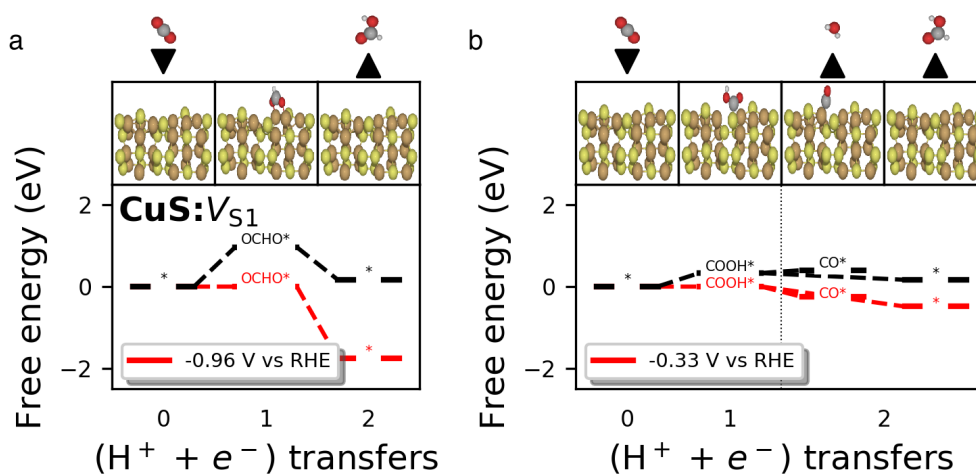


Figure 4.13 Comparison of calculated CO₂RR pathways to produce formic acid from (a) OCHO* and (b) COOH* intermediates on CuS (110) with a surface S vacancy (V_{S1}) at the S1 dimer S site. The black curves are pathways calculated at 0 V vs RHE and the red curves are at the potential that makes the entire included pathway downhill in free energy, as computed within the CHE model. V_{S1} are found to slightly destabilize the OCHO*-mediated formic acid pathway (a), but make it much easier to bind COOH* intermediates at the undercoordinated surface S1 sites relative to pure CuS(110).

We also note that these potentials predicted to initiate CO₂RR to formate are also slightly below that computed for competitive hydrogen adsorption and hydrogen evolution to H₂, which we predict occurs at a potential of -0.4 V (-0.9) vs RHE on S (Cu) sites on CuS(110) (Figure 4.11). These results support the idea that formic acid production may proceed via OCHO* and possibly COOH* intermediates on CuS(110) and that surface O_S and V_S species should enhance the activity of CO₂RR and selectivity

toward HCOOH, consistent with the XPS surface characterization and electrochemical measurements on Cu₂O/CuS.

Furthermore, we believe the presence of CuS is responsible for the improved electrochemical stability of Cu₂O in the Cu₂O/CuS nanocomposites under CO₂RR conditions. According to previous studies,^{17, 48} a gradient band structure is expected to form at the heterojunction of CuS and Cu₂O, promoting the photo-excited electron transfer from Cu₂O to CuS and, thus, protecting Cu₂O from reduction. Our characterization results, calculations, and long-term stability data provide indirect evidence to support this mechanism. TEM results confirm the presence of Cu₂O in the CuS/Cu₂O composite catalyst after CO₂RR. In addition, the stable formate generation over 30 hours suggests the CuS/Cu₂O catalyst is long-lived, in contrast to other previously reported Cu₂O catalysts. Taken together, these results reveal the essential role of CuS in stabilizing Cu₂O during CO₂RR. This is also supported by computed results that S removal from the CuS (110) surface under reduction conditions is not favorable (Figure 4.12); thus it is expected that charge transfer to sulfide should enhance the stability of the surface under CO₂RR.

4.4 Conclusion

In summary, we have prepared a new Cu₂O/CuS nanocomposite catalyst via multistep conversion from Cu₂S. The Cu₂O/CuS shows outstanding catalytic performance for formate generation via CO₂RR, achieving a FE of 67.6 % and j_{HCOO} of 15.3 mA/cm² for formate at -0.9 V vs. RHE, which outperforms most other Cu, CuS or Cu₂O catalysts. DFT simulations indicate that CuS (110) surfaces exhibit a

preferential selectivity toward HCOOH over CO, with substitutional surface O_s or vacancy V_s species expected to lead to reduced onset potentials and enhanced catalytic activities, with both COOH*- and OCHO*-mediated CO₂RR pathways expected to contribute. Cu₂O/CuS maintained an excellent FE=62.9 %, j_{HCOO^-} =12.3 mA/cm² towards formate at -0.9 V vs. RHE during the 30-hour stability test, suggesting that the incorporation of CuS could stabilize Cu₂O during the CO₂RR. These findings open new opportunities in the design of low-cost Cu₂O-based catalysts for CO₂RR and provide additional insight into the influence of sulfide phases in the selective production of formate.

References

1. C. F. Hansen, A. L. Riis, S. Bresson, O. Højbjerg, B. B. Jensen, *Livest. Sci.* **2007**, *108*, 206-209.
2. J. T. Feaster, C. Shi, E. R. Cave, T. Hatsukade, D. N. Abram, K. P. Kuhl, C. Hahn, J. K. Nørskov, T. F. Jaramillo, *ACS Catal.* **2017**, *7*, 4822-4827.
3. X. Lu, D. Y. C. Leung, H. Wang, M. K. H. Leung, J. Xuan, *ChemElectroChem* **2014**, *1*, 836-849.
4. S. Kapusta, N. Hackerman, *J. Electrochem. Soc.* **1983**, *130*, 607-613.
5. D. H. Won, C. H. Choi, J. Chung, M. W. Chung, E.-H. Kim, S. I. Woo, *ChemSusChem* **2015**, *8*, 3092-3098.

6. C. F. Izard, D. B. Müller, *Resources, Conservation and Recycling* **2010**, *54*, 1436; Y. Jian-guang, L. Jie, P. Si-yao, L. Yuan-lu, S. Wei-qiang, *J. Hazard. Mater.* **2016**, *304*, 409-416.
7. H. Dehghani, D. Bogdanovic, *Resources Policy* **2018**, *55*, 55-59.
8. A. Loiudice, P. Lobaccaro, E. A. Kamali, T. Thao, B. H. Huang, J. W. Ager, R. Buonsanti, *Angew. Chem. Int. Ed.* **2016**, *55*, 5789-5792.
9. Z. Tao, Z. Wu, X. Yuan, Y. Wu, H. Wang, *ACS Catal.* **2019**, *9*, 10894-10898.
10. A. K. Mishra, N. H. de Leeuw, *J. CO2 Util.* **2016**, *15*, 96-106.
11. J. Li, Y. Kuang, Y. Meng, X. Tian, W.-H. Hung, X. Zhang, A. Li, M. Xu, W. Zhou, C.-S. Ku, C.-Y. Chiang, G. Zhu, J. Guo, X. Sun, H. Dai, *J. Am. Chem. Soc.* **2020**, *142*, 7276-7282.
12. X. Zhu, K. Gupta, M. Bersani, J. A. Darr, P. R. Shearing, D. J. L. Brett, *Electrochim. Acta* **2018**, *283*, 1037-1044.
13. J. Qiao, M. Fan, Y. Fu, Z. Bai, C. Ma, Y. Liu, X.-D. Zhou, *Electrochimica Acta* **2015**, *153*, 559; M. Fan, Z. Bai, Q. Zhang, C. Ma, X.-D. Zhou, J. Qiao, *RSC Adv.* **2014**, *4*, 44583-44591.
14. K. Jiang, R. B. Sandberg, A. J. Akey, X. Liu, D. C. Bell, J. K. Nørskov, K. Chan, H. Wang, *Nat. Catal.* **2018**, *1*, 111-119.
15. C. W. Li, M. W. Kanan, *J. Am. Chem. Soc.* **2012**, *134*, 7231-7234.
16. X. Chen, R. Chen, X. Zhu, Q. Liao, Y. Zhang, D. Ye, B. Zhang, Y. Yu, J. Li, *J. Catal.* **2019**, *372*, 182-192.

17. H.-N. Wang, X. Chen, R. Chen, X. Zhu, Q. Liao, D.-D. Ye, B. Zhang, Y.-X. Yu, W. Zhang, J.-W. Li, *J. Power Sources* **2019**, *435*, 226766.
18. A. A. Dubale, A. G. Tamirat, H.-M. Chen, T. A. Berhe, C.-J. Pan, W.-N. Su, B.-J. Hwang, *J. Mater. Chem. A* **2016**, *4*, 2205-2216.
19. S. V. Bagul, S. D. Chavhan, R. Sharma, *Journal of Physics and Chemistry of Solids* **2007**, *68*, 1623; L. Isac, I. Popovici, A. Enesca, A. Duta, *Energy Procedia* **2010**, *2*, 71-78.
20. X. Yu, X. An, *Mater. Lett.* **2010**, *64*, 252-254.
21. S. Gong, X. Wu, J. Zhang, N. Han, Y. Chen, *CrystEngComm* **2018**, *20*, 3096-3104.
22. A. Santos, *Nanomaterials (Basel)* **2018**, *8*, 691.
23. a) Y. Wang, Z. Chen, P. Han, Y. Du, Z. Gu, X. Xu, G. Zheng, *ACS Catal.* **2018**, *8*, 7113-7119; b) P. Han, Z. Wang, M. Kuang, Y. Wang, J. Liu, L. Hu, L. Qian, G. Zheng, *Adv. Energy Mater.* **2018**, *8*, 1801230.
24. a) G. Kresse, J. Furthmüller, *Comput. Mater. Sci.* **1996**, *6*, 15-50; b) G. Kresse, J. Furthmüller, *Phys. Rev. B* **1996**, *54*, 11169; c) P. E. Blöchl, *Phys. Rev. B* **1994**, *50*, 17953; d) B. Hammer, L. B. Hansen, J. K. Nørskov, *Phys. Rev. B* **1999**, *59*, 7413.
25. K. Mathew, V. S. C. Kolluru, S. Mula, S. N. Steinmann, R. G. Hennig, *J. Chem. Phys.* **2019**, *151*, 234101.

26. S. P. Ong, W. D. Richards, A. Jain, G. Hautier, M. Kocher, S. Cholia, D. Gunter, V. L. Chevrier, K. A. Persson, G. Ceder, *Comput. Mater. Sci.* **2013**, *68*, 314-319.
27. A. A. Peterson, F. Abild-Pedersen, F. Studt, J. Rossmeisl, J. K. Nørskov, *Energy Environ. Sci.* **2010**, *3*, 1311-1315.
28. J. B. Varley, H. A. Hansen, N. L. Ammitzbøll, L. C. Grabow, A. A. Peterson, J. Rossmeisl, J. K. Nørskov, *ACS Catal.* **2013**, *3*, 2640-2643.
29. a) L. P. Granda-Marulanda, A. Rendón-Calle, S. Builes, F. Illas, M. T. M. Koper, F. Calle-Vallejo, *ACS Catal.* **2020**, *10*, 6900-6907; b) F. Studt, F. Abild-Pedersen, J. B. Varley, J. K. Nørskov, *Catal. Lett.* **2013**, *143*, 71-73.
30. J. K. Nørskov, J. Rossmeisl, A. Logadottir, L. Lindqvist, J. R. Kitchin, T. Bligaard, H. Jónsson, *J. Phys. Chem. B* **2004**, *108*, 17886-17892.
31. T. Kou, C. Si, J. Pinto, C. Ma, Z. Zhang, *Nanoscale* **2017**, *9*, 8007-8014.
32. C.-K. Wu, M. Yin, S. O'Brien, J. T. Koberstein, *Chem. Mater.* **2006**, *18*, 6054-6058.
33. N. Karikalan, R. Karthik, S.-M. Chen, C. Karuppiah, A. Elangovan, *Sci. Rep.* **2017**, *7*, 2494.
34. a) C. Xiang, G. M. Kimball, R. L. Grimm, B. S. Brunshwig, H. A. Atwater, N. S. Lewis, *Energy Environ. Sci.* **2011**, *4*, 1311-1318; b) P. Dubot, D. Jousset, V. Pinet, F. Pellerin, J. P. Langeron, *Surf. Interface Anal.* **1988**, *12*, 99-104.
35. K. L. Chavez, D. W. Hess, *J. Electrochem. Soc.* **2001**, *148*, G640-G643.

36. L. Trotochaud, A. R. Head, S. Pletincx, O. Karshioğlu, Y. Yu, A. Waldner, L. Kyhl, T. Hauffman, H. Terryn, B. Eichhorn, H. Bluhm, *J. Phys. Chem. B* **2018**, *122*, 1000-1008.
37. a) Y. Xie, A. Riedinger, M. Prato, A. Casu, A. Genovese, P. Guardia, S. Sottini, C. Sangregorio, K. Miszta, S. Ghosh, T. Pellegrino, L. Manna, *J. Am. Chem. Soc.* **2013**, *135*, 17630-17637; b) C.-H. Kuo, Y.-T. Chu, Y.-F. Song, M. H. Huang, *Adv. Funct. Mater.* **2011**, *21*, 792-797; c) Y. W. Yang, L. J. Fan, *Langmuir* **2002**, *18*, 1157-1164; d) C. M. Whelan, M. R. Smyth, C. J. Barnes, N. M. D. Brown, C. A. Anderson, *Appl. Surf. Sci.* **1998**, *134*, 144-158; e) F. W. Herbert, A. Krishnamoorthy, W. Ma, K. J. Van Vliet, B. Yildiz, *Electrochim. Acta* **2014**, *127*, 416-426; f) W. Liu, H. Niu, J. Yang, K. Cheng, K. Ye, K. Zhu, G. Wang, D. Cao, J. Yan, *Chem. Mater.* **2018**, *30*, 1055-1068.
38. F. Wu, J. Li, Y. Tian, Y. Su, J. Wang, W. Yang, N. Li, S. Chen, L. Bao, *Scientific Reports* 2015, *5*, 13340; L. Zhang, L. Ji, P.-A. Glans, Y. Zhang, J. Zhu, J. Guo, *Phys. Chem. Chem. Phys.* **2012**, *14*, 13670-13675.
39. a) D. Kim, S. Lee, J. D. Ocon, B. Jeong, J. K. Lee, J. Lee, *Phys. Chem. Chem. Phys.* **2015**, *17*, 824-830; b) F. Li, S.-F. Zhao, L. Chen, A. Khan, D. R. MacFarlane, J. Zhang, *Energy Environ. Sci.* **2016**, *9*, 216-223; c) S. Lee, G. Park, J. Lee, *ACS Catal.* 2017, *7*, 8594-8604.
40. Z. Zhao, X. Peng, X. Liu, X. Sun, J. Shi, L. Han, G. Li, J. Luo, *J. Mater. Chem. A* **2017**, *5*, 20239-20243.

41. Y. Huang, A. D. Handoko, P. Hirunsit, B. S. Yeo, *ACS Catal.* **2017**, *7*, 1749-1756.
42. Y.-X. Duan, F.-L. Meng, K.-H. Liu, S.-S. Yi, S.-J. Li, J.-M. Yan, Q. Jiang, *Adv. Mater.* **2018**, *30*, 1706194.
43. S. Sen, D. Liu, G. T. R. Palmore, *ACS Catal.* **2014**, *4*, 3091-3095.
44. H. Mistry, A. S. Varela, C. S. Bonifacio, I. Zegkinoglou, I. Sinev, Y.-W. Choi, K. Kisslinger, E. A. Stach, J. C. Yang, P. Strasser, B. R. Cuenya, *Nat. Commun.* **2016**, *7*, 12123.
45. P. De Luna, R. Quintero-Bermudez, C.-T. Dinh, M. B. Ross, O. S. Bushuyev, P. Todorović, T. Regier, S. O. Kelley, P. Yang, E. H. Sargent, *Nat. Catal.* **2018**, *1*, 103-110.
46. a) I. V. Chernyshova, P. Somasundaran, S. Ponnurangam, *Proc. Natl. Acad. Sci. U. S. A.* **2018**, *115*, E9261-E9270; b) J. S. Yoo, R. Christensen, T. Vegge, J. K. Nørskov, F. Studt, *ChemSusChem* **2016**, *9*, 358-363.
47. R. García-Muelas, F. Dattila, T. Shinagawa, A. J. Martín, J. Pérez-Ramírez, N. López, *J. Phys. Chem. Lett.* **2018**, *9*, 7153-7159.
48. a) G. Panzeri, M. Cristina, M. S. Jagadeesh, G. Bussetti, L. Magagnin, *Sci. Rep.* **2020**, *10*, 18730; b) T. C. van Thiel, J. Fowlie, C. Autieri, N. Manca, M. Šiškins, D. Afanasiev, S. Gariglio, A. D. Caviglia, *ACS Materials Lett.* **2020**, *2*, 389-394; c) S. A. Lee, S. Choi, C. Kim, J. W. Yang, S. Y. Kim, H. W. Jang, *ACS Materials Lett.* **2020**, *2*, 107-126; d) Z. Zeng, G. Fu, H. B. Yang, Y. Yan, J.

Chen, Z. Yu, J. Gao, L. Y. Gan, B. Liu, P. Chen, *ACS Materials Lett.* **2019**, *1*, 432-439.

Chapter 5

Amorphous CeO₂-Cu Heterojunction for CO₂ Reduction into Multi-carbon Alcohols

Abstract

Coupling with renewable electricity, electrochemically converting CO₂ greenhouse gas into value-added chemicals, such as multi-carbon (C₂₊) alcohols, is believed to be a strategy of two birds with one stone. However, tremendous challenges are still present in restricting the intrinsic activity and selectivity to C₂₊ alcohols. Herein, in this work we adopted a combined metallurgy-dealloying-in situ CO₂ reduction method to synthesize amorphous CeO₂-Cu heterojunction, aiming at enriching the catalysts with intrinsically active and selective sites to produce C₂₊ alcohols. The interfacial sites of amorphous CeO₂-Cu heterojunction have been found to not only improve the adsorption of key intermediates such as *CO, but also stabilize *CH₂CHO at the bifurcation step, steering the reaction toward C₂₊ alcohols over ethylene. A fairly high faradaic efficiency of 34.15% toward C₂₊ alcohols at -0.6 V vs. RHE has thus been achieved over the amorphous CeO₂-Cu heterojunction.

5.1 Introduction

Multi-carbon (C₂₊) alcohols are important chemical feedstocks in different industries and can also be upgraded to hydrocarbon fuels including gasoline and diesel.¹ Owing to the importance of C₂₊ alcohols to the human society, their market size has been continuously increased over the past decades. It has been estimated that the global market size of ethanol itself already hit 75 billion of US dollars (USD).²

Conventionally, the generation of C_{2+} alcohols mainly depend on microbial fermentation or petrochemical process, whereas both are problematic either due to the generation of greenhouse gas by-product (e.g. CO_2) or harsh synthesis conditions (e.g. elevated temperatures and pressures).³ The price of renewable electricity has been decreased significantly in the recent years. For example, the price of wind powered electricity already reached a low level of about 0.02 USD per kWh.² Under this scenario, coupling with renewable electricity and electrochemically converting CO_2 into C_{2+} alcohols (i.e. CO_2 reduction) has been accepted as a promising strategy, which offers two-fold benefit of neutralizing carbon footprint and sustainably producing value added chemical feedstocks at the same time.

Among different catalysts, Cu is the only metal that can convert CO_2 into hydrocarbons, and oxygenates including C_{2+} alcohols due to its capability of adsorbing various key intermediates and C-C coupling.⁴ Nonetheless, the selectivity towards C_{2+} alcohols is inferior limited by multiple reasons such as the competing hydrogen evolution reaction, the relatively weak adsorption strength towards $*CO$, and bifurcating reaction pathways towards ethylene vs. alcohols. Introducing secondary component has been found to be able to alter the electronic structures of Cu and thus the selectivity to C_{2+} alcohols. CeO_2 is commonly used support material in metal-support catalysts and its activity enhancement through interface effect has been proved in thermal catalysis. For example, CeO_2 supported Cu showed improved activity in activating and adsorbing CO_2 and promoting the adsorption of CO in thermal catalysis of hydrogenation of CO_2 and CO oxidation,^{5,6} respectively. Most recently, hybridizing

Cu and CeO₂ has also been demonstrated as electrocatalysts for CO₂ reduction in a couple of reports.⁷⁻¹² Even though the major components only include Cu and CeO₂, the product distribution varies in these studies, and some interesting trends can be generalized based on literature reports.⁷⁻¹² For instance, doping atomic Cu into CeO₂ or interfacing nanocrystalline Cu with CeO₂ leads to similar product distributions, with CH₄ as a major product (Faradaic efficiency, *i.e.*, F.E. ~55%).^{9, 10, 12} Increasing the fraction of crystalline Cu shifts the product to ethylene, with a F.E. close to 50%.^{7, 8, 11, 12} For example, the Cu with a fraction of 0.4 was decorated on top of CeO₂ nanorods by Yin *et al.* and the composite showed a F.E. of 42% towards ethylene in 0.100 M CsHCO₃ (H-Cell).¹² In spite of the F.E. towards C₂₊ alcohols is still around or less than 20%, the trend suggests that the interfacial structure plays a dominant role in tuning the product distribution of Cu and CeO₂ composite.

Owing to the abundant defect sites resulted from the long-range disordering atomic arrangement, amorphous structures have shown appealing properties in boosting the intrinsic activity of electrocatalysts.^{13, 14} For example, the amorphous Cu nanoparticles synthesized by Duan *et al.* exhibited a F.E. of 22% towards ethanol at -1.4 V vs. RHE in 0.100 M KHCO₃, whereas only 6% of the ethanol was generated over the crystalline Cu only at -1.7 V vs. RHE.¹³ By virtue of the interfacial effect between Cu and CeO₂, in this work we introduced nanoporous amorphous heterojunction between Cu and CeO₂ (denoted as np CeO₂-Cu catalyst) through a combined metallurgy-dealloying-*in situ* CO₂ reduction strategy. Theoretical studies suggest that the interfacial sites of the np CeO₂-Cu heterojunction bring the benefits of enhanced adsorption of key

intermediates (*CO, *CH₂CHO). Particularly the synergistic Cu-Ce binary centers stabilize *CH₂CHO intermediate through Ce-O and Cu-C bonding, which steers the reaction toward C₂₊ alcohols that were proved with a F.E. of 34.15% at -0.6 V vs. RHE in 1.00 M KOH (flow cell).

5.2 Experimental Section

Catalyst synthesis: Al₉₀Cu_{7.5}Ce_{2.5} (at%) alloy ingot was prepared using high-frequency induction furnace loaded with pure metals of Al, Cu and Ce. All metals are with 99.9 wt% purity. Then, the ingot was transferred to a quartz tube and heated up to melt through high-frequency induction. Rapid solidification was performed by injecting the melt to a single roller of melt-spinning instrument in argon ambience, and eventually alloy ribbons with thickness of 20 to 50 μm and width of 2 to 5 mm were obtained. To perform dealloying, 200 mg of the alloy ribbon was transferred into a beaker containing 100 ml 5.00 M NaOH (Acris Organics) in a 50 °C oven for dealloying until no gas bubbles (5 hours). The as-dealloyed Cu-Ce-O catalyst was rinsed by deionized water and ethanol consecutively for several times and dried under vacuum overnight. For comparison, Al₉₀Cu₁₀ alloy was also prepared and dealloyed under the same conditions to obtain Cu as control sample.

Preparation of gas diffusion electrodes: 5 mg of catalyst was dispersed in a mixed solution (22 μL 5% Nafion solution, 978 μL isopropanol), and then sonicated for 30 mins in ice-water bath to get the homogeneous catalyst ink. In order to prepare the gas diffusion electrode, the catalyst ink was air-sprayed onto the H14C9 (Fuel Cell Store)

gas diffusion layer with an areal catalyst loading of 0.56 mg/cm² and dried under vacuum.

Catalysts characterizations: The phase compositions of the alloy precursor and as-dealloyed sample were characterized using X-ray diffraction (XRD) (Rigaku Smartlab Powder & Thin Film Diffractometer). The morphological, and chemical information of the spent catalysts were characterized using scanning electron microscopy (SEM, FEI), transmission electron microscopy (TEM, TalosF200C G2), and X-ray photoelectron spectroscopy (XPS, Thermofisher Nexsa G2).

Electrochemical measurements: The electrochemical measurements were conducted in a customized flow cell using a three-electrode fashion. The gas diffusion electrode with exposed area of 1 cm², nickel foam, and Hg/HgO (1.00 M KOH) serve as the working, counter and reference electrodes, respectively. Fumasep FAS-50 (Fuel cell store) anion exchange membrane was used to separate cathode and anode chamber. 1.00 M KOH solution was purified (electrolysis for 24 h (0.1 mA, graphite rods as working and counter electrodes) to remove any trace amount of metal ions.) and used as electrolyte and circulated in cathode and anode chambers separately. CO₂ gas (Praxair, 4.5 Laser) was flowed through the gas chamber in adjacent to the GDE at a flow rate of 40 sccm. The electrochemistry data were collected using a CHI electrochemical workstation (Model 660D). The CO₂ reduction performances were electrochemically evaluated using chronoamperometry at potentials from -0.5 to -0.8 V vs. RHE (*iR* corrected).

Products evaluation: Gas chromatography (SRI, Model 8610C) and 800 MHz nuclear magnetic resonance (NMR, Bruker Ascend 800) spectroscopy were used to quantify the gas and liquid products, respectively. Argon (Praxair, 5.0 ultra-high purity) was used as the carrier gas in GC measurement. The F.E. values for gas products were calculated using the following equation:

$$\text{F.E.} = \frac{n e^- \times 40 \left(\frac{\text{ml}}{\text{min}}\right) \times 10^{-6} \left(\frac{\text{m}^3}{\text{ml}}\right) \times v(\text{vol}\%) \times 1.01 \times 10^5 \left(\frac{\text{N}}{\text{m}^2}\right) \times 9.65 \times 10^4 \left(\frac{\text{C}}{\text{mol}}\right)}{8.314 \left(\frac{\text{N}\cdot\text{m}}{\text{mol}\cdot\text{K}}\right) \times 298.15 \text{ (K)} \times I \text{ (A)} \times 60 \left(\frac{\text{s}}{\text{min}}\right)}$$

where n is the number of electrons involved in the CO_2 reduction process, $40 \left(\frac{\text{ml}}{\text{min}}\right)$ is the flow rate of the CO_2 gas, $1.01 \times 10^5 \left(\frac{\text{N}}{\text{m}^2}\right)$ is the atmospheric pressure, $9.65 \times 10^4 \left(\frac{\text{C}}{\text{mol}}\right)$ is the Faraday constant, $v(\%)$ is percent of gas products (derived from GC), $8.314 \left(\frac{\text{N}\cdot\text{m}}{\text{mol}\cdot\text{K}}\right)$ is the gas constant, 298.15 (K) is room temperature, and I is the current.

Both anolyte and catholyte were collected for ^1H NMR analysis to quantify the liquid product. To prepare samples for NMR testing, 0.5 ml of diluted electrolyte solution was mixed with 0.1 ml deuterium oxide (D_2O , 99.9%) and dimethyl sulfoxide (DMSO, 56.3 mM) was added as an internal standard. The F.E. values were calculated using the following equation:

$$\text{F.E.} = \frac{n e^- \times 56.3 \text{ (mM)} \times \left(\frac{S_{\text{product}}}{S_{\text{DMSO}}}\right) \times \frac{6}{A} \times V_{\text{ml}} \times 9.65 \times 10^4 \left(\frac{\text{C}}{\text{mol}}\right)}{\text{Total charge}}$$

where n is the number of electrons involved in the CO_2 reduction process, 56.3 mM is the concentration of DMSO internal standard, S_{product} and S_{DMSO} are the respective peak areas of product and DMSO in the NMR spectrum, constant 6 is added in the equation because DMSO has 6 protons while A indicates the specific proton numbers in the

product, V in ml is the total volume of electrolyte solution in each chamber, and 9.65×10^4 C per mole is the Faraday constant. The total charge was obtained from chronoamperometry data.

Theoretical simulations: The first-principles calculations based on density functional theory (DFT) in this work are performed using the projected augmented wave (PAW) method included in the commercial Vienna ab-initio simulation package (VASP). Molecular dynamics (MD) was used to assist the building of amorphous structure of CeO_2 . The electron exchange correlation was described by the generalized gradient approximation (GGA) with the function of Perdew-Burke-Ernzerhof. The energy cutoff was set to 500 eV and the Brillouin zone was sampled by a Gamma $1 \times 1 \times 1$ K-point grid for a simple qualitative calculation. The vacuum gap of 15 Å was used to avoid the interaction between the periodic slabs. The bottom atomic position was fixed to facilitate the convergence while the surface atomic position was fully relaxed until the maximum force and energy on each atom were less than -0.04 eV/Å and 10^{-5} eV, respectively. The weak interaction has been considered through the DFT-D3 scheme. In order to obtain the np CeO_2 -Cu heterogeneous model, a supercell containing 64 Ce atoms, 133 O atoms and 24 Cu atoms was constructed as the initial model where Cu atoms are embedded in the lattice of CeO_2 based on CeO_2 (110) and Cu (111). After performing the AIMD simulation on this model at 800 K, a random structure was selected for the subsequent DFT calculation. The adsorption energy of CO and CH_2CHO adsorbed on CeO_2 -Cu can be calculated as $E_b = E(\text{total}) - E(\text{CeO}_2\text{-Cu}) - E(\text{ads})$, where $E(\text{total})$, $E(\text{CeO}_2\text{-Cu})$, and $E(\text{ads})$ represent the total energies of the

adsorbed system, clean CeO₂-Cu slab, and *CO or *CH₂CHO moieties in vacuum, respectively. For the protonation calculation, the computational hydrogen electrode method was used to calculate the adsorption free energies, which assumes the chemical potential of an electron-proton pair is equal to that of ½ H₂ in the gas phase. The free energies of adsorption are then calculated as $\Delta G = \Delta E + \Delta ZPE - \Delta TS$, where ΔE , ΔZPE , T, and S are adsorption energy, zero-point energy, temperature, and entropy, respectively.

5.3 Results and Discussion

The catalyst was synthesized through a combined metallurgy, dealloying and *in situ* CO₂ reduction strategy. Specifically, the Al₉₀Cu_{7.5}Ce_{2.5} (at. %) alloy ingot obtained by high-frequency induction was re-melted and rapidly solidified into alloy ribbons precursors (Figure 5.1). The X-ray diffraction (XRD) pattern (Figure 5.2a) of the alloy ribbons indicates a mixture of three phases including Al, and Al enriched intermetallic compounds (Al₃CuCe, JCPDS#18-0009, and Al₈Cu₄Ce, JCPDS#16-0494). Upon dealloying in 5.00 M NaOH, the Al phase and the Al component in the intermetallic compounds were selectively leached, accompanied by the diffusion of noble atoms (i.e. Cu and Ce) along the interface of alkaline solution/alloy and reconstruction. As a result, the as-dealloyed sample showed a different profile of phase compositions as shown in Figure 5.2b. The Al components were completely disappeared, whereas the cubic and hexagonal CeO₂ (JCPDS#34-0349, 44-1001), Cu₂O (JCPDS# 34-1354) and Cu (JCPDS# 01-1241) phases can be identified in the XRD pattern. The as-dealloyed samples were loaded as cathode in a flow cell circulated with 1.00 M KOH electrolyte,

and electrochemically treated through amperometry technique under CO₂ reduction conditions. The spent catalyst with desired CO₂ reduction performances (denoted as np CeO₂-Cu) were characterized.

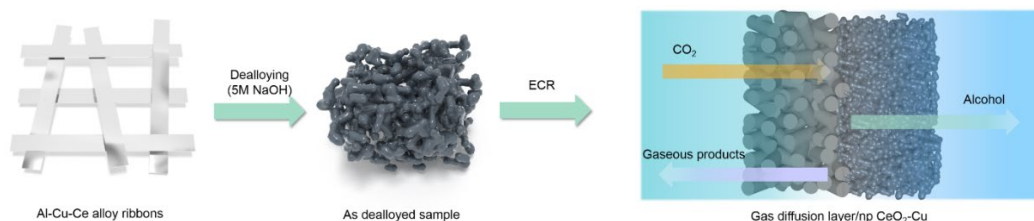


Figure 5.1 Schematic illustration of the synthesis and test of as-dealloyed catalysts.

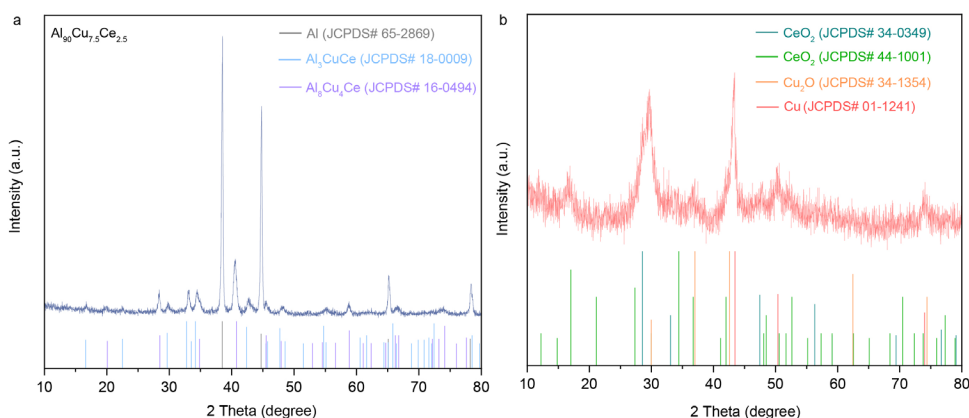


Figure 5.2 X-ray diffraction patterns of a) Al₉₀Cu_{7.5}Ce_{2.5} alloy precursor and b) as-dealloyed sample.

The morphologies of the spent catalysts and Cu control sample (denoted as np Cu) were investigated using transmission scanning electron microscopy with a solid-state detector. Both show nanoporous structures (Figure 5.3a and b, Figure 5.4a and b) which is typically present as a result of dealloying, in which the leaching of the active Al component and the reorganization of noble components synergistically contribute to the formation of pore-islands structures. The diffuse halo rings in the selected area

electron diffraction (SAED) of both samples (Figure 5.3c and Figure 5.4c) suggest the amorphous feature which was also confirmed through high-resolution transmission electron microscopy (HR-TEM, Figure 5.3d). Few lattice fringes (spacing indexed to CuO) adjacent to the amorphous area (highlighted by the enclosed dashed lines) confirm the low crystalline characteristics, suggesting that the amorphization of the catalyst during CO₂ reduction. The transformation to amorphous structures during CO₂ reduction has been lately reported in very few literatures^{15, 16}. Even though the mechanism is still not fully explored, the amorphization of catalysts is expected to bring improved intrinsic activity due to the abundant defect sites.¹⁴ X-ray photoelectron spectroscopy (XPS) was adopted to further study the chemical environment and elemental valance. Core-level Cu 2p spectrum of the spent Cu sample exhibits typical spin-orbit splitting which leads to doublet of Cu 2p_{1/2} and Cu2p_{3/2}. Specifically, the peaks at 934.5 and 953.8 eV suggest the presence of Cu²⁺ in the form of CuO.^{17, 18} The deconvoluted O 1s spectrum indicates different oxygen species on np Cu, with the peaks at 535.8 and 533.9 eV attributed to the oxygen functional groups in residual Nafion binder¹⁹, and 532.2 and 530.8 eV associated to the adsorbed oxygen species and lattice oxygen in CuO^{20, 21}, respectively. The Cu 2p high resolution XPS spectrum of np CeO₂-Cu shows similar doublet of Cu 2p_{1/2} and Cu2p_{3/2} and typical Cu²⁺ satellite peak, except for the slight peaks shifting to higher binding energies (Figure 5.3e). The 1s spectrum of O in the np CeO₂-Cu also reveals similar deconvoluted peaks with that of np Cu, while not much information can be generated in this spectrum as lattice oxygen in CuO and CeO₂ shares overlapped binding energies.^{20, 22} The Ce 3d core-level

spectrum exhibits typical doublet of Ce 3d_{3/2} and Ce 3d_{5/2}, and ten peaks are deconvoluted due to the presence of mixed Ce valance of CeO₂. For example, the peaks of v⁰, v' u₀ and u' labeled in Figure 5.3e correspond to the Ce³⁺, whereas the v, v'', v''', u, u'' and u''' are associated with Ce⁴⁺ in CeO₂.²³ Compared to Ce 3d XPS spectrum of CeO₂ reported in literature, peak shifting to high binding energies also happened. The combined Cu 2p and Ce 3d spectra consistently indicate some electronic interactions. The characterizations consistently suggest that the np CeO₂-Cu catalyst is composed of CuO and amorphous CeO₂. Nonetheless, Cu oxides including CuO can be easily reduced to metallic Cu during CO₂ reduction.²⁴ The presence of CuO is thus believed to be resulted from a series of spontaneous chemical conversion happened after the CO₂ reduction. Specifically, Cu₂O can be easily formed by the oxidation of Cu, and the conversion of Cu₂O to CuO was found to occur in alkaline solution ($Cu_2O + 2OH^- = 2CuO + H_2O + 2e^-$)²⁵.

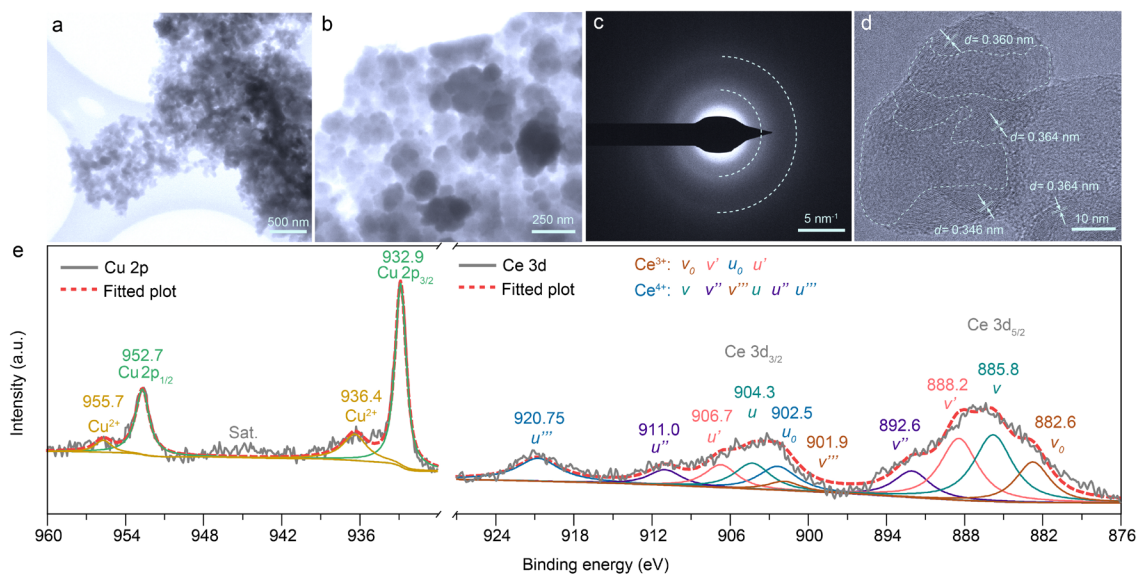


Figure 5.3 a) and b) are the transmission electron images of the spent np CeO₂-Cu catalysts at low and higher magnifications, c) SAED image, d) HR-TEM image of the np CeO₂-Cu particles, e) Cu 2p and Ce 3d core-level XPS spectra of the spent np CeO₂-Cu catalyst.

In the reaction pathway toward C₂₊ alcohols, *CO adsorption has been widely accepted as one of the important decisive steps as enhanced binding strength between *CO and active site can ensure a higher coverage of this early intermediate and increase its residence time, facilitating the transition into late intermediates.²⁶ In order to obtain atomic insights into the *CO binding capability of the catalyst, CeO₂-Cu heterojunction model has been built and the amorphous CeO₂ is simulated through molecular dynamics (MD) and density functional theory (DFT). There are nine *CO adsorption configurations in total being investigated based on the location of the site. The sites in the amorphous CeO₂ far away from heterojunction exhibits a weak adsorption profile toward *CO and the adsorption energies are relatively close to zero (Table 5.1). Differential charge analysis was performed on these configurations and the charge of *CO intermediate in configuration 1-6 is almost the same with that of individual CO molecular (Table 5.1), suggesting that there is bare charge transfer between the CeO₂ sites and *CO intermediate, which also indicates a typical physical adsorption profile. In comparison, the top, bridge and hollow sites of Cu show improved adsorption strength towards *CO (configuration 7-9, Figure 5.4a-c) and charge transfer behaviors (Table 5.1), revealing a characteristic chemical adsorption. Among those sites, the Cu at the CeO₂-Cu interface (i.e. bridge site in configuration 9) achieves a more stable

adsorption configuration and exhibits particularly improved binding strength, with adsorption energy of -1.04 eV. The survey of the *CO adsorption on different locations indicates that interfacing amorphous CeO₂ and Cu contributes to the enhanced adsorption capability of *CO intermediate. In addition to *CO adsorption, the binding strength to the late intermediate *CH₂CHO is also critical, as the reaction pathway bifurcates at *CH₂CHO toward either ethylene or C₂₊ alcohols.²⁶ A relatively stronger binding strength between the site and *CH₂CHO could also suppress the reaction towards ethylene, which improves the selectivity to C₂₊ alcohols at the same time. In order to shed light on the capability of retaining *CH₂CHO over the CeO₂-Cu heterojunction, a detailed site-to-site adsorption study was also carried out (Figure 5.4 d-f). As shown in Table 5.2, Cu or Ce sites away from the heterojunction (configuration 1'-5') show relatively weak adsorption to *CH₂CHO. In contrast, the Cu-Ce sites at the CeO₂-Cu interface (configuration 6'-8') exhibits improved *CH₂CHO adsorption capability as indicated by the increased charge transfer of the oxygen species in *CH₂CHO intermediate and more negative adsorption energies of -2.24 to -2.59 eV, suggesting a promoted binding strength at the interface. This can be rationalized by the synergistic adsorption effect of Cu-Ce site at which the Ce shows higher affinity towards oxygen and Cu binds the carbon of *CH₂CHO intermediate.

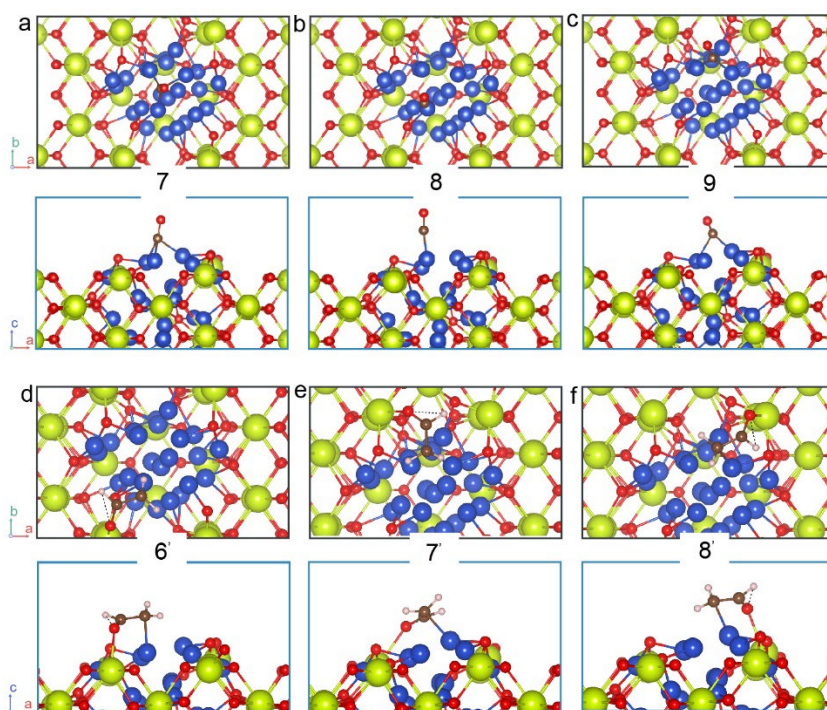


Figure 5.4 a)-c) *CO adsorption configurations on np CeO₂-Cu catalyst. d)-f) *CH₂CHO adsorption configurations 6'-8' on np CeO₂-Cu catalyst. Green, red, blue and brown spheres represent Ce, O, Cu, and C atoms, respectively. The top view and side view are highlighted by black and cyan boxes, respectively. These labeling marks are consistent in the main text and SI.

Table 5.1 *CO adsorption configurations and associated adsorption energy.

*CO adsorption configuration	Adsorption energy (eV)	Charge of O (e)	Charge of C (e)	Charge of CO (e)
1	-0.35	7.11	2.94	10.05
2	-0.36	7.09	2.92	10.02

3	-0.31	7.06	2.93	9.99
4	-0.29	7.08	2.92	10.00
5	-0.29	7.10	2.90	10.01
6	-0.18	7.13	2.86	9.99
7	-0.83	7.01	3.39	10.40
8	-0.90	7.07	3.08	10.15
9	-1.04	7.07	3.20	10.27
CO molecule (gas)	—	7.12	2.88	10

Table 5.2 *CH₂CHO adsorption configurations and associated adsorption energy.

*CH ₂ CHO adsorption configuration	Adsorption energy (eV)	Charge of O (e)
1'	-2.01	7.11
2'	-1.67	7.11
3'	-1.75	7.10
4'	-1.63	7.14
5'	-2.31	7.16
6'	-2.56	7.18
7'	-2.24	7.17
8'	-2.59	7.17

Even though Cu-Ce sites near the interface of CeO₂-Cu heterojunction show enhanced adsorption behavior and are able to stabilize *CH₂CHO intermediate, it remains to be a question if the enhanced adsorption of the binary carbon in *CH₂CHO hinders its subsequent reactive transition. Motivated by this question, the protonation step of *CH₂CHO in configuration 8' which corresponds to the most likely adsorption profile has also been investigated (Figure 5.5). Both the Cu-Cu site and the Cu-Ce interface site were selected for the comparisons of protonation. There are two possible protonation paths for the intermediate: one is the hydrogenation at the CH₂ group, and the other is the hydrogenation at CHO. The stability of protonated intermediates on the catalyst determines the energy barrier during protonation and the Cu-Cu and Cu-Ce sites contribute different protonation paths. For example, the *CH₂CHO tends to be protonated through the hydrogenation of CHO on Cu-Cu site with an uphill free energy of 0.18 eV, whereas the hydrogenation of CH₂ on Cu-Ce is much favored with only a minimum free energy of 0.08 eV.

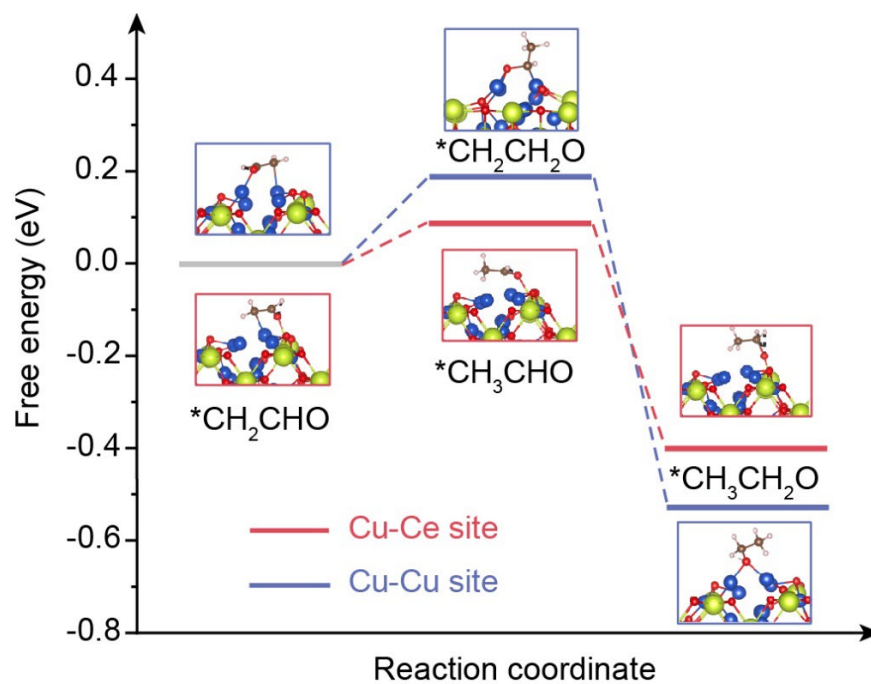


Figure 5.5 The protonation paths of $*CH_2CHO$ and corresponding energy barriers over Cu-Ce and Cu-Ce site of np CeO_2 -Cu.

The theoretical studies suggest that the np CeO_2 -Cu heterojunction benefits the generation of C_{2+} , which is also confirmed by the electrochemical characterizations. The F.E. of different products against potentials are compared over the two catalysts (Figure 5.6). As indicated in the bar chart of Figure 5.6, np CeO_2 -Cu exhibits a low F.E. of 11.2% for hydrogen evolution reaction (HER) at -0.6 V vs. RHE, suggesting most of the charge was contributed to CO_2 reductions. A fairly high F.E. (34.15%, Figure 5.7) toward C_{2+} alcohols over np CeO_2 -Cu catalyst is achieved at a low potential of -0.6 V (vs. RHE) as well, with ethanol and 1-propanol being 28.41% and 5.74%, respectively. In contrast, at the same potential the np Cu control sample shows more than doubled F.E. (28.6%) of HER, suggesting the addition of Ce component largely

suppressed HER during CO₂ reductions. A much lower F.E. of only 19.22% toward C₂₊ alcohols (18.92% and 0.3% for ethanol and 1-propanol, respectively) is obtained in the Cu control sample at the same potential. The measurements over three independent samples were performed and these samples show comparable selectivity for C₂₊ alcohols, with average F.E. of 32.9%±2.62% and 17.91%±3.29% for np CeO₂-Cu catalyst and np Cu control sample, respectively. As aforementioned, ethylene shares the same intermediate (*CH₂CHO) with C₂₊ alcohols and thus the reaction could bifurcate to both products, leading to the difficulties of improving selectivity to C₂₊ alcohols. In order to electrochemically evaluate the selectivity to C₂₊ alcohols vs. ethylene, the ratios of F.E. of ethylene to F.E. of C₂₊ alcohols were plot against potentials. As shown in Figure 5.7b, the ratio is as high as 0.87 for np Cu control sample at -0.6 V vs. RHE, whereas a much lower ratio of only 0.37 is achieved for np CeO₂-Cu, indicating that the reaction toward ethylene is suppressed over np CeO₂-Cu, compared to the np Cu control sample. In addition, np CeO₂-Cu also exhibits much improved partial current densities of C₂₊ alcohols, with a $j_{\text{part.}}$ of 19.35 mA/cm² at -0.6 V vs. RHE, more than twice of that of np Cu control sample (Figure 5.7c). In order to shed light on the improved partial current densities for np CeO₂-Cu vs. np Cu, electrochemical surface area (ECSA) is studied through investigating the difference of anodic and cathodic capacitive current against scan rate. At a given geometric area, np CeO₂-Cu indeed shows slightly improved ECSA compared to that of np Cu sample, as revealed by the capacitance (7.7 mF of np CeO₂-Cu vs. 6.6 mF of np Cu) in Figure 5.7d. The increased ECSA provides the chance of enriching active sites on the catalysts, but

it cannot give insights if the improved partial current density could be attributed to the intrinsic activity of each active site. Further analysis was performed by investigating the ratio of j_{ecsa} of np CeO₂-Cu to the j_{ecsa} of np Cu which is revealed in Figure 5.7e. The ratio is above 1 at potentials of -0.6 V vs. RHE or more negative, which confirms that the np CeO₂-Cu catalyst is enriched with intrinsically active site for C₂₊ alcohols. More impressively, the np CeO₂-Cu catalyst not only exceeds other Cu-Ce based catalysts reported recently in F.E. toward C₂₊ alcohols, but also shows comparable or even better performances than those advanced catalysts reported in literatures (Figure 5.7f), such as Cu nanoparticles²⁷, grain boundary rich Cu²⁸, (nano)porous Cu^{29, 30}, Cu based bimetallic catalysts including CuZn³¹, CuAu³², Cu-Ag^{33, 34}, and Cu based compound such as Cu₂S-Cu-V (V represents Cu vacancy)³⁵.

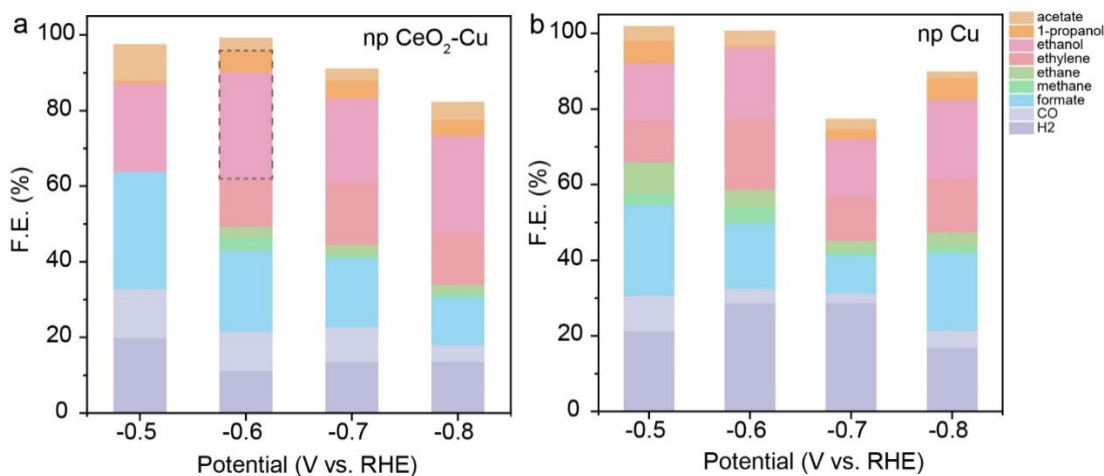


Figure 5.6 F.E. comparisons of all products of a) np CeO₂-Cu and b) np Cu at different potentials. The dashed box highlights the F.E. of C₂₊ alcohols.

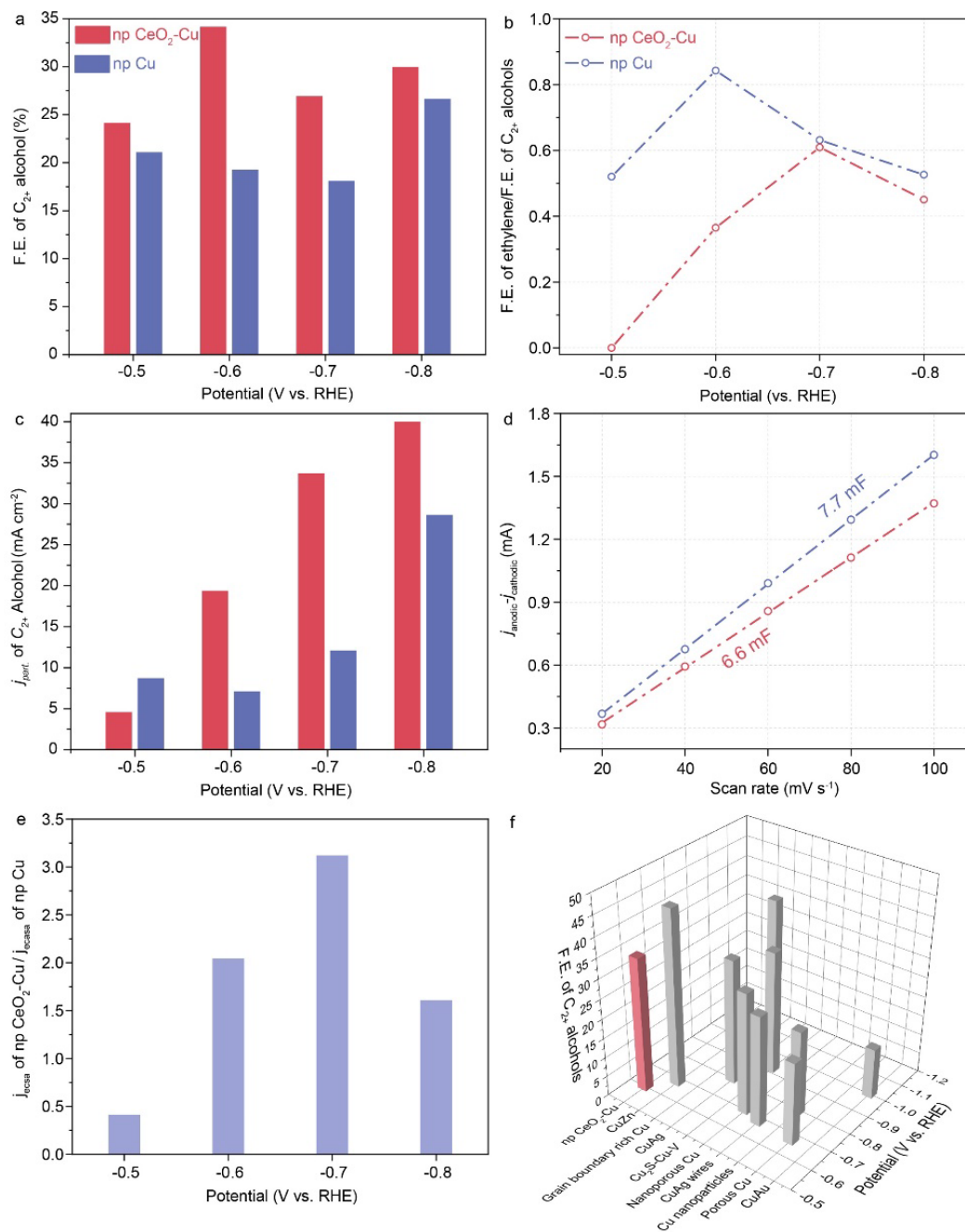


Figure 5.7 The comparisons of a) F.E. of alcohols, b) the ratio of F.E. of ethylene/alcohol, c) partial current density of alcohol, d) C_{dl} of np CeO₂-Cu and np Cu, e) the ratio of j_{ccsa} of np CeO₂-Cu to np Cu at different potentials, f) literature data tested under similar conditions.

5.4 Conclusion

In summary, we realized a heterojunction between Cu and amorphous CeO₂ through a combined metallurgy-dealloying-*in situ* CO₂ reduction strategy. The interfacial sites of np CeO₂-Cu were found to be able to improve the adsorption strength of *CO and *CH₂CHO, which enhances the coverage of the key intermediates, contribute to the subsequent reactive transition into late intermediates and steer the reaction pathway toward C₂₊ alcohols. The np CeO₂-Cu catalyst thus exhibited a fairly high F.E. of C₂₊ alcohols of 34.15% at a low potential of -0.6 V vs. RHE in flow cell circulated with alkaline electrolyte and confirms a high intrinsic activity and selectivity. This work exemplifies an efficient strategy in designing amorphous heterojunction in improving the selectivity of C₂₊ alcohols.

References

1. R. McGinnis, *Joule* **2020**, *4*, 509-511.
2. H. Shin, K. U. Hansen, F. Jiao, *Nat. Sustain.* **2021**, *4*, 911-919.
3. S. Gehrman, N. Tenhumberg, *Chem. Ing. Tech.* **2020**, *92*, 1444-1458.
4. Y. Hori, I. Takahashi, O. Koga, N. Hoshi, *J. Mol. Catal. A: Chem.* **2003**, *199*, 39-47.
5. J. Graciani, K. Mudiyanse, F. Xu, E. Baber Ashleigh, J. Evans, D. Senanayake Sanjaya, J. Stacchiola Darío, P. Liu, J. Hrbek, F. Sanz Javier, A. Rodriguez José, *Science* **2014**, *345*, 546-550.
6. T. Kou, C. Si, J. Pinto, C. Ma, Z. Zhang, *Nanoscale* **2017**, *9*, 8007-8014.

7. S. Chu, X. Yan, C. Choi, S. Hong, A. W. Robertson, J. Masa, B. Han, Y. Jung, Z. Sun, *Green Chem.* **2020**, *22*, 6540-6546.
8. C. W. Lee, S.-J. Shin, H. Jung, D. L. T. Nguyen, S. Y. Lee, W. H. Lee, D. H. Won, M. G. Kim, H.-S. Oh, T. Jang, H. Kim, B. K. Min, Y. J. Hwang, *ACS Energy Lett.* **2019**, *4*, 2241-2248.
9. S. B. Varandili, J. Huang, E. Oveisi, G. L. De Gregorio, M. Mensi, M. Strach, J. Vavra, C. Gadiyar, A. Bhowmik, R. Buonsanti, *ACS Catal.* **2019**, *9*, 5035-5046.
10. Y. Wang, Z. Chen, P. Han, Y. Du, Z. Gu, X. Xu, G. Zheng, *ACS Catal.* **2018**, *8*, 7113-7119.
11. X. Yan, C. Chen, Y. Wu, S. Liu, Y. Chen, R. Feng, J. Zhang, B. Han, *Chem. Sci.* **2021**, *12*, 6638-6645.
12. J. Yin, Z. Gao, F. Wei, C. Liu, J. Gong, J. Li, W. Li, L. Xiao, G. Wang, J. Lu, L. Zhuang, *ACS Catal.* **2022**, *12*, 1004-1011.
13. Y.-X. Duan, F.-L. Meng, K.-H. Liu, S.-S. Yi, S.-J. Li, J.-M. Yan, Q. Jiang, *Adv. Mater.* **2018**, *30*, 1706194.
14. J. Liu, L. Guo, *Matter* **2021**, *4*, 2850-2873.
15. Y. Zhao, X. Tan, W. Yang, C. Jia, X. Chen, W. Ren, S. C. Smith, C. Zhao, *Angew. Chem. Int. Ed.* **2020**, *59*, 21493-21498.
16. X. Zhou, X. Lu, T. Yu, H. Wang, L. Qian, P. Lei, Y. Yu, L. Liu, S. Xia, J. Fang, *ACS Appl. Mater. Interfaces* **2020**, *12*, 31319-31326.

17. J.-R. Li, S.-Q. Wang, Z.-X. Zhuang, Z.-G. Liu, Z. Guo, X.-J. Huang, *Chinese J. Anal. Chem.* **2022**, *50*, 24-31.
18. X. Lv, G. Liang, Q. Wang, Y. Li, H. Duan, D. Chen, M. Long, Q. Hu, F. Han, L. Li, *JOM* **2020**, *72*, 4458-4465.
19. A. K. Friedman, W. Shi, Y. Losovyj, A. R. Siedle, L. A. Baker, *J. Electrochem. Soc.* **2018**, *165*, H733-H741.
20. H. Wang, J.-Z. Xu, J.-J. Zhu, H.-Y. Chen, *J. Cryst. Growth* **2002**, *244*, 88-94.
21. M. Zhu, P. Tian, M. E. Ford, J. Chen, J. Xu, Y.-F. Han, I. E. Wachs, *ACS Catal.* **2020**, *10*, 7857-7863.
22. P. M. Albrecht, D.-e. Jiang, D. R. Mullins, *J. Phys. Chem. C.* **2014**, *118*, 9042-9050.
23. C. Anandan, P. Bera, *Appl. Surf. Sci.* **2013**, *283*, 297-303.
24. S. Wang, T. Kou, S. E. Baker, E. B. Duoss, Y. Li, *Mater. Today Nano* **2020**, *12*, 100096.
25. W.-Y. Zeng, J.-H. Lai, I. C. Cheng, *J. Electrochem. Soc.* **2021**, *168*, 123501.
26. X. Zhi, A. Vasileff, Y. Zheng, Y. Jiao, S.-Z. Qiao, *Energy Environ. Sci.* **2021**, *14*, 3912-3930.
27. S. Ma, M. Sadakiyo, R. Luo, M. Heima, M. Yamauchi, P. J. A. Kenis, *J. Power Sources* **2016**, *301*, 219-228.
28. Z. Chen, T. Wang, B. Liu, D. Cheng, C. Hu, G. Zhang, W. Zhu, H. Wang, Z.-J. Zhao, J. Gong, *J. Am. Chem. Soc.* **2020**, *142*, 6878-6883.

29. T. T. H. Hoang, S. Ma, J. I. Gold, P. J. A. Kenis, A. A. Gewirth, *ACS Catal.* **2017**, *7*, 3313-3321.
30. J.-J. Lv, M. Jouny, W. Luc, W. Zhu, J.-J. Zhu, F. Jiao, *Adv. Mater.* **2018**, *30*, 1803111.
31. D. Ren, J. Gao, L. Pan, Z. Wang, J. Luo, S. M. Zakeeruddin, A. Hagfeldt, M. Grätzel, *Angew. Chem. Int. Ed.* **2019**, *58*, 15036-15040.
32. C. G. Morales-Guio, E. R. Cave, S. A. Nitopi, J. T. Feaster, L. Wang, K. P. Kuhl, A. Jackson, N. C. Johnson, D. N. Abram, T. Hatsukade, C. Hahn, T. F. Jaramillo, *Nat. Catal.* **2018**, *1*, 764-771.
33. T. T. H. Hoang, S. Verma, S. Ma, T. T. Fister, J. Timoshenko, A. I. Frenkel, P. J. A. Kenis, A. A. Gewirth, *J. Am. Chem. Soc.* **2018**, *140*, 5791-5797.
34. X. She, T. Zhang, Z. Li, H. Li, H. Xu, J. Wu, *Cell Rep. Physic. Sci.* **2020**, *1*, 100051.
35. T.-T. Zhuang, Z.-Q. Liang, A. Seifitokaldani, Y. Li, P. De Luna, T. Burdyny, F. Che, F. Meng, Y. Min, R. Quintero-Bermudez, C. T. Dinh, Y. Pang, M. Zhong, B. Zhang, J. Li, P.-N. Chen, X.-L. Zheng, H. Liang, W.-N. Ge, B.-J. Ye, D. Sinton, S.-H. Yu, E. H. Sargent, *Nat. Catal.* **2018**, *1*, 421-428.

Chapter 6

Outlook

As discussed in the previous chapters, some novel electrocatalysts showed promising results in water splitting and carbon dioxide reduction reaction studies. However, there are still many challenges. Here, a few key challenges are listed, and some potential solutions are discussed.

Electrochemical water splitting: Additional efforts should be devoted on high current densities water splitting.¹ At high current densities, gas bubble removal will be a big challenge. Rapid bubble removal is critical in minimizing the ohmic resistance and retaining the ECSA during high-rate water splitting. In addition, minimizing the bubble size could reduce the electrode damage from the detachment of gas bubbles. In this regard, a superaerophobic electrode/catalyst surface and bubble flow channels are highly desirable for high-rate water splitting.

Structural/compositional stability is important. Strengthening the adhesion between the catalysts layer and substrate would be crucial in prevent the catalysts detachment from the substrate during gas bubble releasing. Compared to catalysts coated on substrate using polymer binders, self-standing catalysts or catalysts directly grow on a substrate with strong chemical bonding are more mechanically stable. For high-rate water splitting, high overpotentials needs to be applied to reach the large current densities. Quite often catalysts are not thermodynamically stable under the large applied potential and extreme local pH, leading to compositional changes over the long-

term operation. Ideally, the catalysts used for high-rate water splitting should be stable in a broad range of applied potentials and pH conditions.

Electrochemical CO₂ reduction: additional efforts should be devoted to understanding the mechanisms of electrochemical reduction of CO₂. Promising results have been obtained by combining experiments with DFT simulations. However, since many electronic and reduction steps are involved in CO₂RR, it is hard to fully identify CO₂ reduction pathways for all products. Reduction conditions, such as local pH and electrolyte concentration, can also influence the performance, which adds complication for mechanistic studies. For example, the CO-CO coupling step is widely considered to be the rate determining step for CO₂ electroreduction to form C₂₊ products on Cu-based catalysts. However, it remains unclear how one would, through careful catalyst design, improve the selectivity for C₂H₅OH while suppressing formation of C₂H₄. Additional electro-kinetic studies are also needed to answer these questions.

The reactor design is also important for CO₂RR. Flow cell test configurations can achieve much higher current densities than H cells. The gas diffusion layer (GDL) enables gaseous CO₂ to pass through and directly interact with the catalyst and, thus, mitigates the CO₂ mass transport issue (due to its low solubility in aqueous electrolyte). In addition, it is widely accepted that high local pH can suppress H₂ formation, and lead to high C₂₊ selectivity by promoting the CO-CO coupling step. The flow cell also enables use of alkaline electrolytes for CO₂RR because the GDL can effectively separate the CO₂ gas and the alkaline electrolyte. As catalysts are immobilized on the GDL, CO₂ gas is expected to be reduced on the catalyst before it reacts with the alkaline

electrolyte. However, as the reaction continues, the high pH electrolyte will inevitably be neutralized by CO₂ gas, which affects the device's performance. Recently, Jiao and coworkers discussed the advantages of using a two-step pathway for CO₂ utilization². Since the conversion from CO₂ to CO has been extensively studied and some catalysts have commercially deployed, it could be beneficial to focus future research efforts on electroreduction of CO. This is because CO will not react with alkaline electrolytes, so device instability due to pH changes can be eliminated.

Separation and extraction of different CO₂RR products remains a major challenge. To date, the most widely used electrolyte for CO₂RR is the aqueous KHCO₃ solution. In this system, the liquid products are inevitably mixed with KHCO₃ salt in the solution. It is difficult and energy intensive to separate these liquid products from the salt solution. Inspired by the idea of solid-state batteries, Wang and coworkers designed a CO₂ electrolyzer with a solid-electrolyte³. In this device, ions move between the cathode and anode through a solid ion conducting polymer without the need of liquid electrolyte. As a result, solid-electrolyte devices could use water and CO₂ as reactants and continuously produce pure liquid products without using salt. This design could lower the operational cost of CO₂ electrolyzers. Yet, the different liquid products are still mixed with each other. To solve this issue, the selectivity needs to be improved to to 90% or above for a specific product, otherwise new reactor technologies need to be developed that can efficiently separate products during the reaction.

References

1. T. Kou, S. Wang, Y. Li, *ACS Materials Lett.* **2021**, *3*, 224-234.
2. M. Jouny, G. S. Hutchings, F. Jiao, *Nat. Catal.* **2019**, *2*, 1062-1070.
3. C. Xia, P. Zhu, Q. Jiang, Y. Pan, W. Liang, E. Stavitski, H. N. Alshareef, H. Wang, *Nat. Energy* **2019**, *4*, 776-785.